A RE-EXAMINATION OF THE AUGUST 22, 1949 QUEEN CHARLOTTE EARTHQUAKE

by

TODD KENDALL BOSTWICK

B.A., The University Of California, 1979

A THESIS SUBMITTED IN PARTIAL FULFILMENT OF

THE REQUIREMENTS FOR THE DEGREE OF

MASTER OF SCIENCE

in

THE FACULTY OF GRADUATE STUDIES

DEPARTMENT OF GEOPHYSICS AND ASTRONOMY

We accept this thesis as conforming

to the required standard

THE UNIVERSITY OF BRITISH COLUMBIA

July 1984

© Todd Kendall Bostwick, 1984

In presenting this thesis in partial fulfilment of the requirements for an advanced degree at the University of British Columbia, I agree that the Library shall make it freely available for reference and study. I further agree that permission for extensive copying of this thesis for scholarly purposes may be granted by the head of my department or by his or her representatives. It is understood that copying or publication of this thesis for financial gain shall not be allowed without my written permission.

Department of Geophysics and Astronomy

The University of British Columbia
1956 Main Mall
Vancouver, Canada
V6T 1Y3

Date July 27, 1984

DE-6 (3/81)

Abstract

Using previously unavailable horizontal seismograms recorded at Sitka, Alaska, thirty-eight new aftershock locations were determined for the August 22, 1949 Queen Charlotte earthquake (Ms=8.1). The aftershock zone was found to extend from 300 km to the north of the epicenter to 190 km south of the epicenter, yielding a total aftershock zone of 490 km. This aftershock zone implies that a previously suggested seismic gap to the north of the Ms=8.1 earthquake (Rogers, 1983) does not exist. The aftershock distribution suggests a time variation of the rupture sequence, with the aftershocks clustering first to the north, and then to the south of the epicenter.

The directivity function and differential phases were analyzed at three stations. The results imply a unilateral rupture propagating to the northwest for 265 km at a rupture velocity between 3.1 km/s and 3.5 km/s. The difference between the radiation length and the aftershock zone implies that the radiation fault length does not represent the full rupture fault length. The non-equivalence of the radiation fault length and the rupture fault length suggests that the displacement offset along the fault was uneven, with the largest displacement occurring in the zone indicated by the radiation fault length.

An attempt was made to derive the mechanism solutions for the two largest aftershocks using their azimuthal surface wave radiation patterns. It was concluded that the use of this technique to obtain focal mechanism solutions is ineffective for

this area and time in history when station coverage was sparse and the quality of instrument calibrations poor.

Table of Contents

Abstract ii
List of Tables vi
List of Figures vii
Acknowledgement x

Chapter I
INTRODUCTION 1
1.1 THE QUEEN CHARLOTTE FAULT 1
1.1.1 Tectonic Setting Of The Queen Charlotte Fault 1
1.1.2 Seismicity Of The Queen Charlotte Fault 6
i. Epicenter Locations 6
ii. Focal Mechanisms 8
1.1.3 Fault Model 9
1.2 THE 1949, M 8.1, QUEEN CHARLOTTE EARTHQUAKE 11
1.2.1 Focal Mechanism 12
1.2.2 Seismic Gap 14
1.3 THESIS OBJECTIVES 16

Chapter II
AFTERSHOCK ZONE OF THE 1949 QUEEN CHARLOTTE EARTHQUAKE ...19
2.1 PROCEDURE 19
2.2 RESULTS 27

Chapter III
SURFACE WAVE ANALYSIS 34
3.1 POINT SOURCE MECHANISM SOLUTION 34
3.1.1 Introduction 34
3.1.2 Theory And Computer Programs 35
3.2 RUPTURE PARAMETERS 41
3.2.1 Introduction 41
3.2.2 Directivity Function Theory 42
3.2.3 Differential Phases Theory 44
3.3 PROCESSING 46
3.3.1 Data Acquisition 46
3.3.2 Data Processing 48
3.3.3 Amplitude Data 49
3.3.4 Phase Data 51

Chapter IV
RESULTS FOR THE M=8.1 EARTHQUAKE OF AUGUST 22 52
4.1 DIRECTIVITY FUNCTION 59
4.2 DIFFERENTIAL PHASES 65
4.3 ERROR ANALYSIS 68
4.4 SEISMIC MOMENT AND STRESS DROP 69

Chapter V
RESULTS FOR THE EARTHQUAKES OF AUGUST 23 AND OCTOBER 31 ..74
MECHANISM SOLUTIONS 87

Chapter VI
SUMMARY AND DISCUSSION 94
6.1 DISCUSSION 94
6.2 CONCLUSION 99

BIBLIOGRAPHY 101

APPENDIX A - LIST OF SEISMOGRAPH STATIONS 106

APPENDIX B - WORLD AVERAGED PHASE VELOCITIES AND Q VALUES
.....108

APPENDIX C - EARTH MODEL USED FOR THE AUGUST 23 AND OCTOBER 31 MECHANISM SOLUTIONS 110

APPENDIX D - INSTRUMENT RESPONSE CURVES 111

List of Tables

I. PUBLISHED FAULT PLANE SOLUTIONS FOR EARTHQUAKES ON THE QUEEN CHARLOTTE FAULT 8

II. AFTERSHOCK DATA 22

III. DIFFERENTIAL PHASE FAULT LENGTHS 66

IV. RUPTURE LENGTH FROM DIRECTIVITY AND DIFFERENTIAL PHASES 95

V. ESTIMATE OF SEISMIC SOURCE PARAMETERS OF THE 1949 QUEEN CHARLOTTE EARTHQUAKE 100

List of Figures

1. TECTONIC SETTING OF THE QUEEN CHARLOTTE FAULT 1

2. RECENT TECTONIC HISTORY OF THE QUEEN CHARLOTTE FAULT ..3

3. DIRECTION OF RELATIVE PLATE MOTION 4

4. MODEL OF THE QUEEN CHARLOTTE FAULT ZONE 5

5. SEISMICITY OF THE QUEEN CHARLOTTE REGION 7

6. STRUCTURAL INTERPRETATION OF A REFRACTION SURVEY ACROSS THE QUEEN CHARLOTTE FAULT ZONE 10

7. P-NODAL MECHANISM SOLUTION FOR THE AUGUST 22, 1949 QUEEN CHARLOTTE EARTHQUAKE 13

8. PROPOSED SEISMIC GAPS ON THE QUEEN CHARLOTTE FAULT ...15

9. AFTERSHOCK LOCATIONS 23

10. RELATIONSHIP OF THE CHATHAM STRAIT AND FAIRWEATHER FAULTS TO THE QUEEN CHARLOTTE FAULT 26

11. TIME DISTRIBUTION OF AFTERSHOCKS 27

12. EMPIRICAL MAGNITUDE RUPTURE-LENGTH RELATIONSHIP FOR 7 REGIONS OF THE WORLD 29

13. MAGNITUDE RUPTURE-AREA RELATIONSHIPS 30

14. TIME PROGRESSION OF AFTERSHOCKS 33

15. DIGITIZED TUO SEISMOGRAMS FOR THE AUGUST 22 EARTHQUAKE (M=8.1) 54

16. DIGITIZED PAS AND HON SEISMOGRAMS FOR THE AUGUST 22 EARTHQUAKE (M=8.1) 55

17. TYPICAL GROUP VELOCITY CURVES FOR LOVE AND RAYLEIGH WAVES 56

18. GROUP VELOCITY CURVES FOR THE AUGUST 22 DATA 57

19. GROUP VELOCITY CURVES FOR THE AUGUST 22 DATA 58

20. DIRECTIVITY FUNCTION CURVES 60

21. DECAYING SOURCE DIRECTIVITY FUNCTION CURVES 62

22. THE EFFECT OF BILATERAL RUPTURE ON THE DIRECTIVITY FUNCTION 63

23. LEAST SQUARES SOLUTION TO THE DATA 64

24. RESPONSE CURVE FOR THE PAS STRAIN METER 70

25. DIGITIZED SEISMOGRAMS FOR THE AUGUST 23 EARTHQUAKE (M=6.4) 75

26. DIGITIZED SEISMOGRAMS FOR THE AUGUST 23 EARTHQUAKE (M=6.4) 76

27. DIGITIZED SEISMOGRAMS FOR THE OCTOBER 31 EARTHQUAKE (M=6.2) 77

28. DIGITIZED SEISMOGRAMS FOR THE OCTOBER 31 EARTHQUAKE (M=6.2) 78

29. DIGITIZED SEISMOGRAMS FOR THE OCTOBER 31 EARTHQUAKE (M=6.2) 79

30. GROUP VELOCITY CURVES FOR THE AUGUST 23 LOVE WAVE DATA 80

31. GROUP VELOCITY CURVES FOR THE AUGUST 23 RAYLEIGH WAVE DATA 81

32. GROUP VELOCITY CURVES FOR THE AUGUST 23 SJP DATA 82

33. GROUP VELOCITY CURVES FOR THE OCTOBER 31 LOVE WAVE DATA 83

34. GROUP VELOCITY CURVES FOR THE OCTOBER 31 LOVE WAVE DATA 84

35. GROUP VELOCITY CURVES FOR THE OCTOBER 31 RAYLEIGH WAVE DATA 85

36. GROUP VELOCITY CURVES FOR THE OCTOBER 31 RAYLEIGH WAVE DATA 86

37. THEORETICAL LOVE WAVE RADIATION PATTERN FOR THE AUGUST 23 EARTHQUAKE 88

38. THEORETICAL RAYLEIGH WAVE RADIATION PATTERN FOR THE AUGUST 23 EARTHQUAKE 89

39. THEORETICAL LOVE WAVE RADIATION PATTERN FOR THE OCTOBER 31 EARTHQUAKE 90

40. THEORETICAL RAYLEIGH WAVE RADIATION PATTERN FOR THE OCTOBER 31 EARTHQUAKE 91

41. FOCAL MECHANISMS OF THE AUGUST 23 AND OCTOBER 31 EARTHQUAKES 92

42. DISPLACEMENT ALONG THE SAN ANDREAS FAULT FOR THE 1906 EARTHQUAKE 96

Acknowledgement

This research owes much to Dr. Garry Rogers. Dr. Rogers provided the original suggestion for the thesis, and then gave encouragement and direction during its development. Dr. Rogers also obtained the SIT seismic records for me. My advisor, Dr. Ellis, provided most of the computer programs used in this thesis. He also provided useful direction in the development of this thesis. Dr. Clowes povided valuable support as my surrogate advisor during Dr. Ellis's sabbatical leave.

A special thanks goes to all who read my thesis and improved it: Dr. Clowes, Dr. Rogers, Dr. Ellis, and Dr. Armstrong. I would also like to thank Don White, Dave Mackie, Ian Jones, and, most importantly, my wife Kimiko, for making my time in Canada so enjoyable.

Financial support for this project was provided by Research Agreement 288/83 from the Department of Energy, Mines and Resources, and by NSERC Operating Grant A2617.

I. INTRODUCTION

1.1 THE QUEEN CHARLOTTE FAULT

1.1.1 Tectonic Setting Of The Queen Charlotte Fault

The Queen Charlotte Fault Zone along the west coast of the Queen Charlotte Islands is a transform fault making up part of the boundary between the Pacific and North American lithospheric plates (see Figure 1).

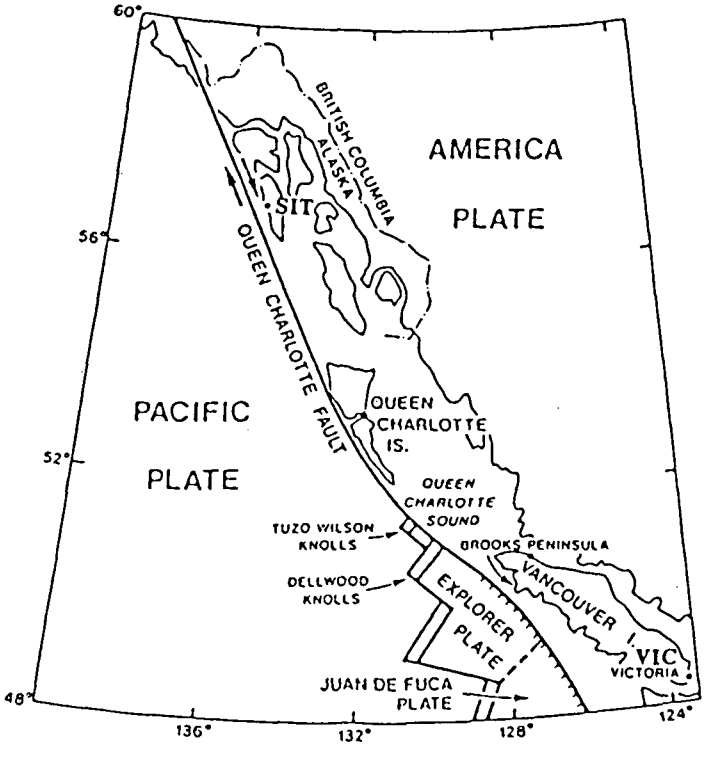

Figure 1 - TECTONIC SETTING OF THE QUEEN CHARLOTTE FAULT

Geographic features, tectonic setting and key seismograph stations (SIT and VIC) in the Queen Charlotte Islands region (adapted from Rogers, 1983).

The fault zone extends northwestward from a ridge-trench-

transform triple junction south of the Queen Charlotte Islands to southern Alaska where it is also known as the Chichagof-Baranof fault (Von Huene et. al., 1979). Current motion along the fault, as determined from global plate motions of Minster and Jordan (1978) and mid-ocean ridge spreading rates, is primarily right-lateral strike-slip at a rate of 5.5 cm/yr (see discussion in Riddihough, 1977).

The fault zone characteristically shows two distinct fault escarpments. Wedged between the two escarpments lies a submarine terrace which is elevated more than 1 km above the basin to the west. Riddihough et al. (1980) have proposed that the present configuration of the fault zone developed about 1 Ma ago, when a triple junction, then located at the end of the Explorer Ridge, jumped northwesterly to the Dellwood Knolls in response to changing spreading conditions of the Explorer Ridge. This led to rifting of older ocean crust (4.5 Ma) and the beginning of spreading at the newly created Dellwood knolls. Hyndman and Ellis (1981) have suggested that this change in position of the triple junction required a landward jump of the Queen Charlotte fault to what is now seen as the inner escarpment, with the outer Queen Charlotte fault scarp accommodating the transcurrent motion between the Pacific and North American plates prior to the jump 1 Ma ago (see Figure 2).

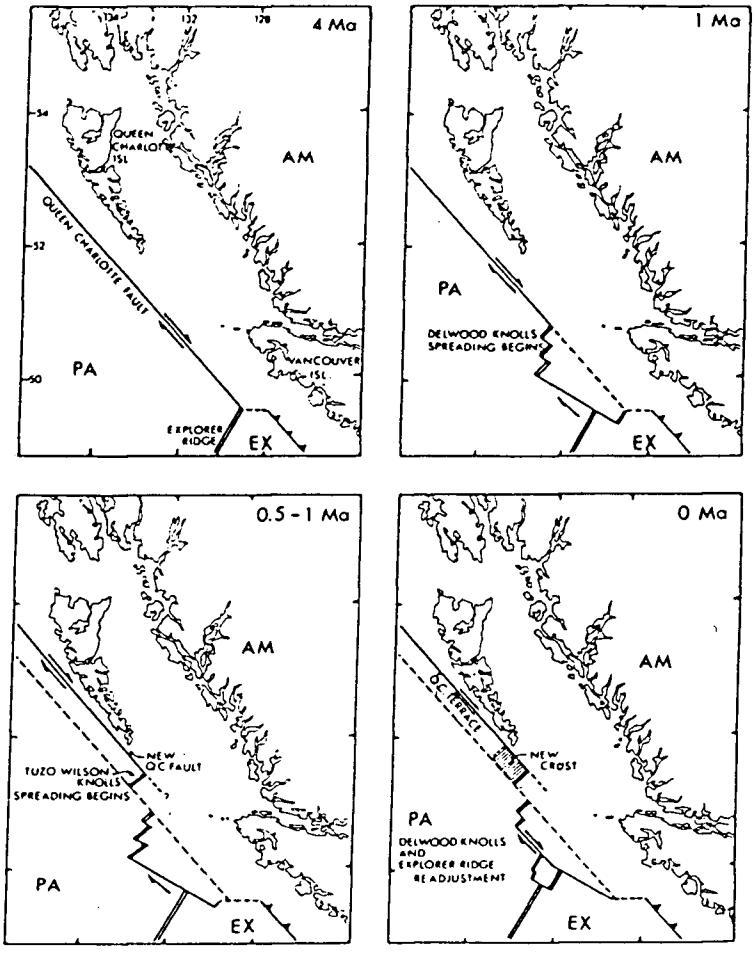

Figure 2 - RECENT TECTONIC HISTORY OF THE QUEEN CHARLOTTE FAULT

Schematic reconstruction of plate tectonic development relevant to the Queen Charlotte Islands region for the past 4 Ma. AM, the North American plate; EX, the Explorer plate; PA, the Pacific plate. Single lines with opposing arrows represent transform margins and the direction of slip; double lines represent spreading margins; and toothed lines represent converging margins with teeth on the overriding plate. At 1 Ma note the difference between the relative motion vector and the trace of the transform fault between Explorer Ridge and Delwood Knolls. This gives rise to instability of the triple junction and the transform fault and leads to asymmetric spreading. At 0.5-1 Ma spreading at Tuzo Wilson Knolls begins. This requires the transform motion between PA and AM to jump landward into older crust, which is then pushed northward with PA. The instability at Delwood Knolls causes readjustment of Explorer Ridge and the transform fault joining the two (after Riddihough et al., 1980; Hyndman and Ellis, 1981).

(From Horn et. al., 1984).

In the present configuration of the fault zone, the bearing of the inner fault trace lies 10° to 20° west of the calculated relative motion vector of Minster and Jordan (1978) between the Pacific and North American plates for the Queen Charlotte region. The angle of this oblique interaction is small at the northern end of the fault but increases towards the southern end along Moresby Island (see figure 3).

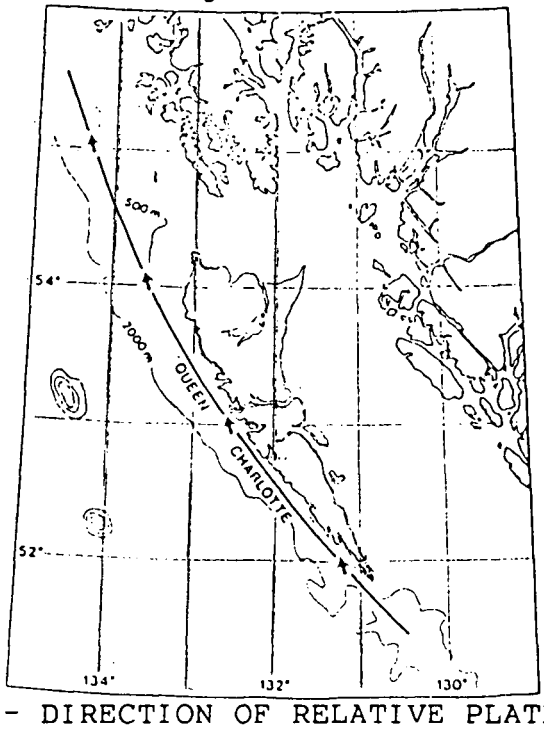

Figure 3 - DIRECTION OF RELATIVE PLATE MOTION

The relative motion arrows show the motion of the Pacific Plate relative to the North American Plate (adapted from Rogers 1983).

The angle of plate interaction suggests there is an element of convergence in the Queen Charlotte region. The convergence could occur by oblique subduction of the Pacific plate or compressive deformation of the Queen Charlotte Islands and adjacent areas, or some combination of both (Perez and Jacob,

1980).

To account for the convergence, Hyndman and Ellis (1981) have suggested an underthrust model, subsequently refined by Hyndman et al. (1982), for the Queen Charlotte fault zone. They suggest oblique subduction could be accomplished first by a series of strike-slip earthquakes, then by oblique convergence until coupling between the overriding and underlying plate is so great that it exceeds the strength of the oceanic lithosphere, and another series of strike-slip events occurs. Thus, by this model, transcurrent faulting occurs in the oceanic lithosphere beneath the continental margin. As the plate is subducted, at intervals in time the faulting must jump seaward to remain near the edge of the continental crust (see figure 4).

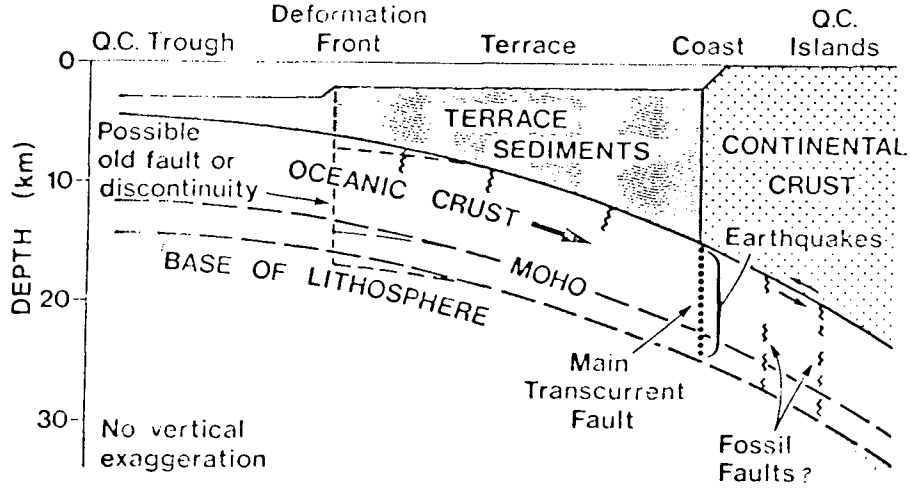

Figure 4 - MODEL OF THE QUEEN CHARLOTTE FAULT ZONE

A possible tectonic model of the Queen Charlotte fault zone. The oblique convergence is resolved into strike-slip motion parallel to the margin on the Queen Charlotte fault and a small component of underthrusting perpendicular to the margin (from Hyndman et al., 1982).

1.1.2 Seismicity Of The Queen Charlotte Fault

The Queen Charlotte region is one of the most seismically active areas of Canada. Indeed, the 1949 Queen Charlotte earthquake (Ms=8.1) which occurred in the middle of the Queen Charlotte Fault is the largest recorded earthquake to have occurred in Canada. Besides the 1949 event, three Ms≥7 earthquakes have occurred since 1900, one in 1929 (Ms=7) at the southern end of the Queen Charlotte Fault, one in 1972 (Ms=7.6) at the northern end of the fault, and the other in 1970 (Ms=7.0) near the southern end of the fault (see Figure 5).

i. Epicenter Locations

Epicenter solutions of earthquakes in the Queen Charlotte Islands region have been obtained by three principal groups of investigators: Tobin and Sykes (1968), Kelleher and Savino (1975), and Rogers (1983). In general, the accuracy of epicenter locations have been limited by the scarcity of seismographs operating in the region. Epicenter uncertainty for events of magnitude M ≥5.0 is ±50 km for most events before 1965 and ±25 km for most events after 1965.

Rogers (1983), after a detailed evaluation of the seismicity data for the Queen Charlotte fault zone, has compiled a seismicity map of the area from 1900 to 1980 (see Figure 5). The seismicity shows a strong correlation with the inner Queen Charlotte fault scarp with little, if any, seismicity inland. This suggests that at present most, if not all, of the Pacific-North American plate motion in this area occurs along the Queen

Charlotte fault.

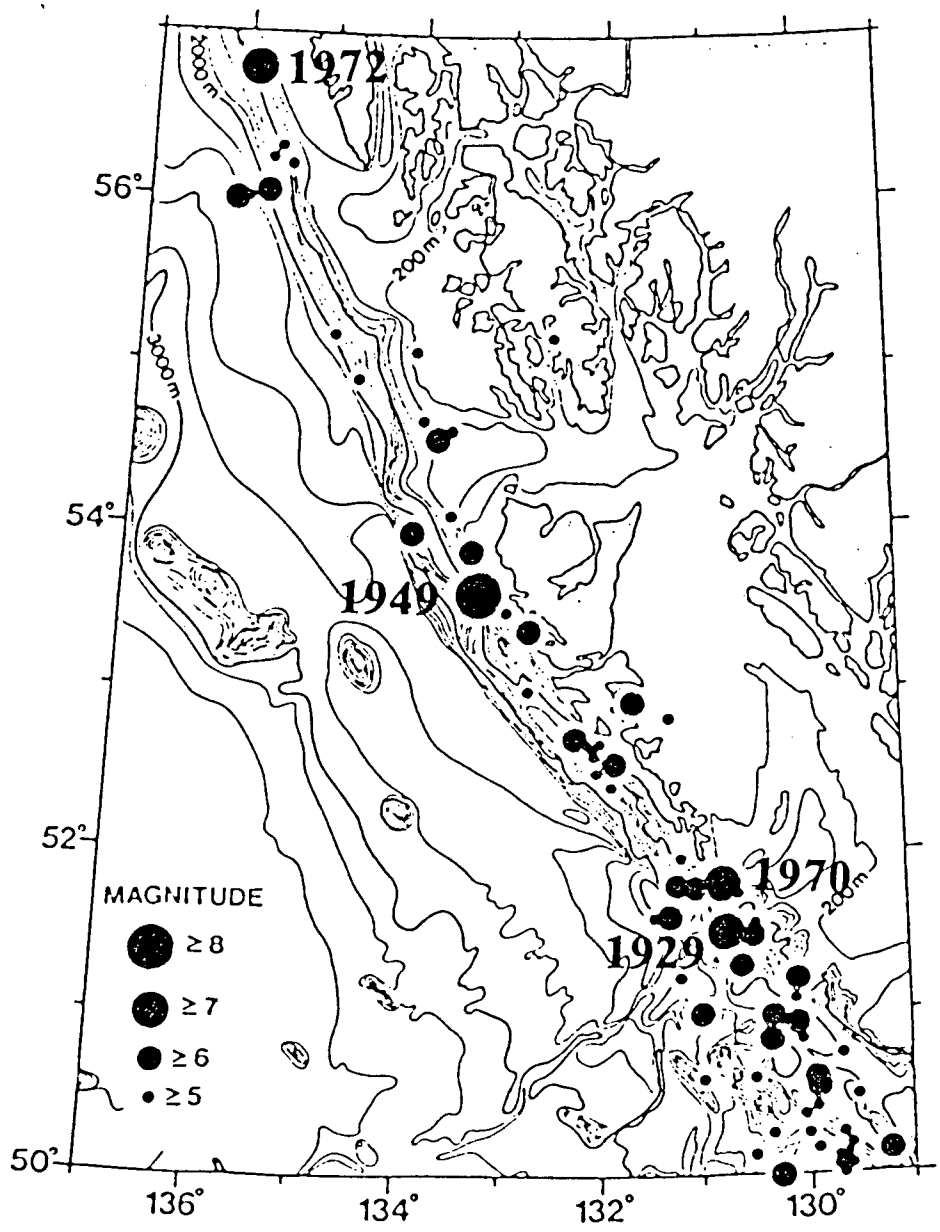

Figure 5 - SEISMICITY OF THE QUEEN CHARLOTTE REGION

Epicenter locations from 1900 to 1980. Through the years the threshold magnitude required for earthquake detection has dropped from M ≥7 between 1900-1917, to M ≥6 between 1917-1948, to M ≥5.0 between 1948-1980 (adapted from Rogers, 1983).

ii. Focal Mechanisms

All published focal mechanisms for earthquakes in the Queen Charlotte Fault Zone are listed in Table 1.

Table I - PUBLISHED FAULT PLANE SOLUTIONS FOR EARTHQUAKES ON THE QUEEN CHARLOTTE FAULT

1927 Oct 24	Stauder,1959; Wickens and Hodgson,1967	strike-slip
1949 Aug 22	Hodgson and Milne,1951; Wickens and Hodgson,1967; Rogers, 1983	strike-slip
1949 Oct 31	Hodgson and Storey,1954; Wickens and Hodgson,1967	thrust
1958 Jul 10	Stauder,1960; Wickens and Hodgson,1967	strike-slip
1970 Jun 24	Chandra,1974; Rogers, 1983	strike-slip
1970 Jun 24	Chandra,1974	strike-slip
1972 Jul 30	Chandra,1974; Perez and Jacob,1980	strike-slip
1972 Aug 04	Chandra,1974	thrust
1972 Aug 15	Perez and Jacob,1980	strike-slip
1973 Jul 01	Chandra,1974; Perez and Jacob,1980	thrust
1973 Jul 03	Chandra,1974; Perez and Jacob,1980	strike-slip
1976 Feb 03	Wetmiller and Horner,1978; Rogers, 1983	strike-slip

The location and orientation of the Queen Charlotte Fault relative to the global distribution of seismographs has effectively limited the size of earthquakes for which well defined P-nodal mechanism solutions have been obtained. The southern extension of the P-nodal fault plane is usually well constrained because it bisects the network of California stations (see Figure 7). But to accurately define the azimuth and dip, the earthquakes must be large enough to record well in Europe. Thus, in the Queen Charlotte Islands region the only well defined fault plane solutions are those for the June 24, 1970 earthquake (Ms=7), and the August 22, 1949 earthquake (Ms=8.1), (Rogers, 1983).

The mechanism solution for the June 24, 1970 earthquake (Chandra 1974; Rogers, 1983) which occurred at the southern end of the Queen Charlotte fault is consistent with predicted plate motions of Minster and Jordan (1978) or Chase (1978) for the area. Perez and Jacob (1980) studied 19 fault plane solutions in the eastern Gulf of Alaska region, four of which occurred on the northern end of the Queen Charlotte fault. The sense of relative plate motion calculated from these earthquake mechanism solutions also corresponds to the predicted relative plate motion of the area. These fault plane solutions imply that the predicted plate motions for the area of Minster and Jordan (1978) or Chase (1978) are correct.

1.1.3 Fault Model

An insight into the cross-sectional structure of the Queen Charlotte fault zone has been provided by the refraction survey across the southern half of the fault zone discussed by Horn et al. (1984). Their interpreted structure section shows three distinctive crustal blocks separated by two major crustally pervasive faults corresponding to the inner and outer Queen Charlotte faults. The rock units making up the westernmost block had velocities consistent with undisturbed oceanic crust. The rock units composing the terrace block had lower velocities at equivalent depths than those of the ocean block or the continental block to the east. The depth to the base of the crustal section of the terrace block increased in depth from 12 to 18 km below sea level, implying an eastward dip of 20° in the

Moho. The inner fault separating the terrace block unit from the continental block appeared to be dipping westward 60°-80°. Figure 6 shows the structural interpretation of by Horn et al. (1984). This interpretation is also consistent with a gravity profile across the area.

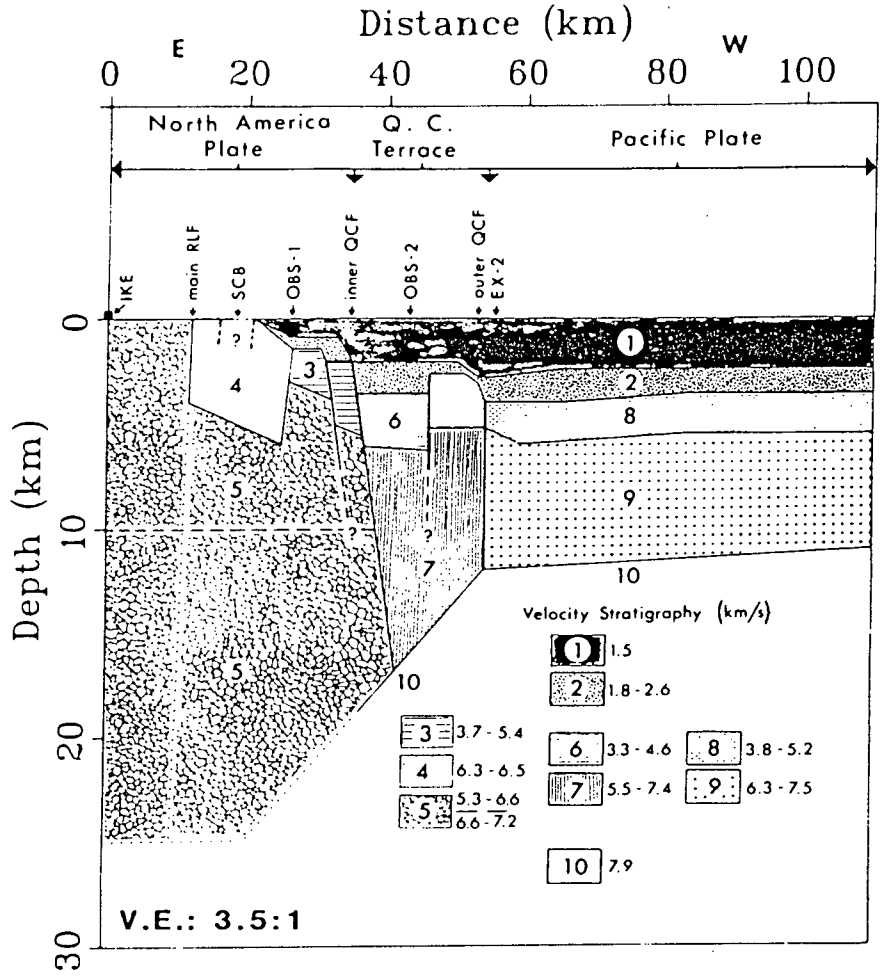

Figure 6 - STRUCTURAL INTERPRETATION OF A REFRACTION SURVEY ACROSS THE QUEEN CHARLOTTE FAULT ZONE

The first number in the velocity stratigraphy gives the velocity at the top of the unit, and the second number gives the velocity at the bottom of the same unit, a linear gradient being assumed. RLF, Louscoone Inlet fault; SCB, San Cristoval batholith (the dashed vertical lines within unit 4 show the surface expression of this batholith); QCF, Queen Charlotte fault; and EX2 shows the location of the perpendicular marine profile.

(From Horn et al., 1984).

The results of Horn et al. (1984) are also consistent with the results of Hyndman and Ellis (1981). In a study of the microearthquake activity along the Queen Charlotte fault zone for a ten day period, Hyndman and Ellis (1981) found almost all the seismicity to be located along what appeared to be a near vertical fault associated with the landward or inner fault scarp; the outer scarp showed no activity. The observed maximum earthquake depth was 21 km.

Using the heat flow results of Hyndman et al. (1981) and thermal elastic arguments, Hyndman and Ellis (1981) also estimated the depth in the crust of the 600°C isotherm, which roughly corresponds to the depth in the crust to which seismic instability or brittle fracture can occur. They found the depth to this boundary to be about 8 km for the ocean basin, 16 km for the submarine terrace and 35 km for the continental crust in the area. These results agree reasonably well with the observed maximum depth of earthquake activity and with the depth of the Moho from Horn et al. (1984).

1.2 THE 1949, M 8.1, QUEEN CHARLOTTE EARTHQUAKE

On Sunday August 22, 1949 at approximately 9:00 P.M. (local time), the Queen Charlotte Islands were shaken by a strong earthquake. The earthquake, felt as far away as Whitehorse (Δ=6.0°) and Jasper (Δ=7.0°) caused considerable excitement. Newspapers reported that "Nervous residents of the Queen Charlottes are wondering if their islands are slowly sinking into the Pacific ocean"; "Small islands have disappeared

in some spots, and new islands have appeared in others following the recent earthquakes off B.C. coast". The seismic hazards in the Queen Charlotte region are vividly illustrated by these newspaper reports and provide a colorful introduction to the 1949 Queen Charlotte Earthquake.

1.2.1 Focal Mechanism

Solutions for the focal mechanism of this earthquake using the first motion of P waves have been obtained by Hodgson and Milne (1951), Wickens and Hodgson (1967), and Rogers (1983). The nine largest aftershocks have been located by Tobin and Sykes (1968), and more recently, relocated by Rogers (1983). The strike of the focal mechanism for the August 22, 1949 earthquake corresponds exactly with the strike of the fault at the latitude of the epicenter. The dip of the fault is very steep and well constrained, with the motion along the fault principally strike-slip coupled with a very small thrust component (see Figure 7). However the direction of the net horizontal motion during this earthquake is significantly different (15^{o}) from the predicted plate motions for the area.

If the plate interaction models are correct, as mechanism solutions of the July 24, 1970 earthquake (Chandra, 1974; Rogers, 1983) and the southern Alaska earthquakes (Perez and Jacob, 1980) imply, then there is a component of convergence, along the Queen Charlotte fault at the latitude of the 1949 earthquake, not taken up by that earthquake.

The convergence might be taken into account in several

ways. One possibility is that the long period motion of the earthquake is different from the motion of the initial first break as indicated by the first motion mechanism solution. Convergence could also be partially taken up in either of the two largest aftershocks on August 23 (M=6.4) and October 31 (M=6.2). Alternatively, this could be one of the large strike-slip earthquakes predicted by the previously mentioned Hyndman and Ellis (1981) model.

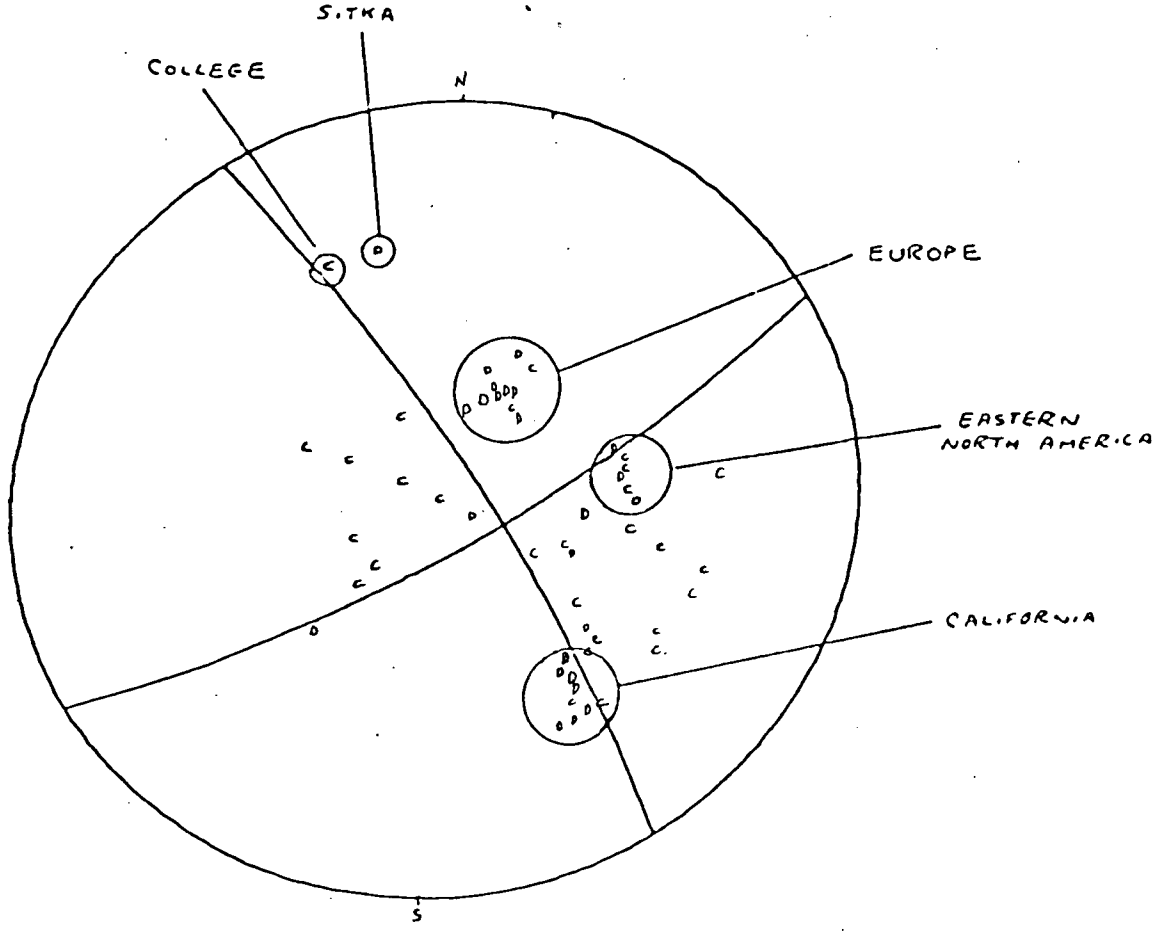

Figure 7 - P-NODAL MECHANISM SOLUTION FOR THE AUGUST 22, 1949 QUEEN CHARLOTTE EARTHQUAKE

August 22, 1949, mechanism solution lower hemisphere projection. Position of key stations are indicated on the focal sphere (Adapted from Rogers, 1983).

1.2.2 Seismic Gap

Kelleher and Savino (1975) have pointed out the possibility of a seismic gap to the north of the August 22, 1949 earthquake (see Figure 8). The uncertainty comes from whether to consider as aftershocks an event located near 56°N on August 23, 1949 and two earthquakes (M=6.25 and 5.5) also near 56°N that occurred on October 31, 1949, more than two months after the main shock. If the northern-most events are aftershocks, the rupture length is 470 km, and no seismic gap exists; if not the rupture length is about 300 km, and a seismic gap does exist.

Although no definite criteria have been established for identification of aftershocks at teleseismic distances, Kelleher (1972), when studying South American rupture zones, did not consider an event an aftershock if it occurred more than two months after the mainshock or if it was isolated by 50 km or more from other aftershocks. By these criteria these events would not be considered as aftershocks and the shorter rupture length of 300 km would be favored. The results of Ben-Menahem (1965, 1978) support this interpretation. Using Love waves (L2 and L3) recorded on the EW strain-meter at Pasadena, Ben-Menahem derived the fault length and rupture velocity of the August 22, 1949 earthquake using the directivity function (Ben-Menahem and Toksoz, 1962) and differential phases (Ben-Menahem, 1961). He obtained a fault length of 265 km and a unilateral rupture velocity of 3.5 km/sec to the northwest.

Most recently, Rogers (1984), has suggested that the seismic gap does not exist. His conclusion is based primarily

on an examination of the SIT (Δ=4.0°) records for the two months following the 1949 earthquake. He noted several S-P intervals of 12-16 seconds which would place them in the distance range of the seismic gap.

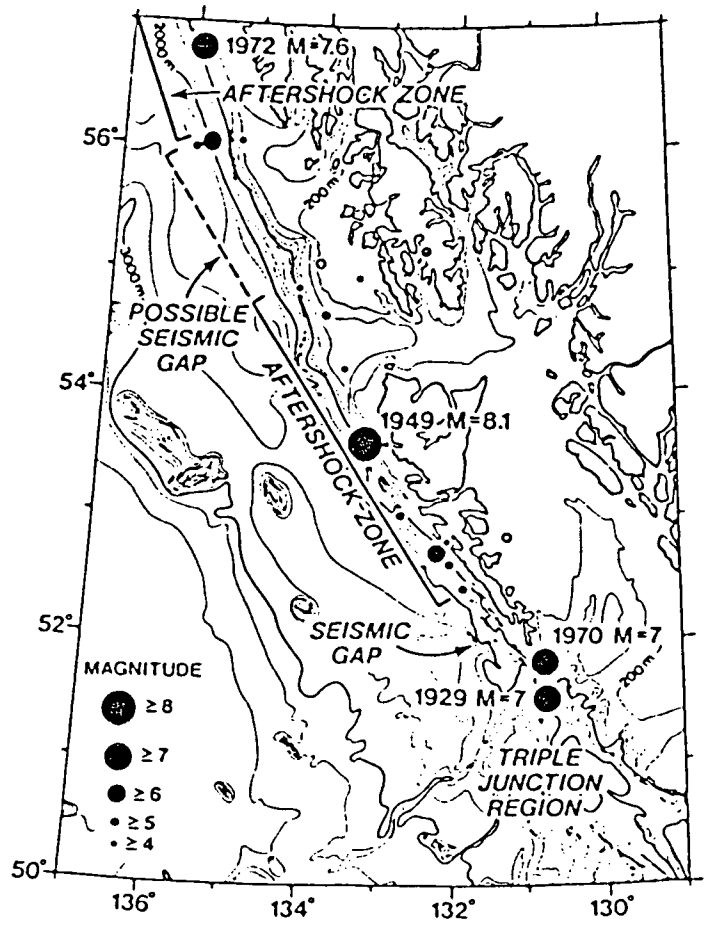

Figure 8 - PROPOSED SEISMIC GAPS ON THE QUEEN CHARLOTTE FAULT

Major earthquakes along the Queen Charlotte Fault zone and the extent of their aftershocks. Shaded circles are poorer solutions (adapted from Rogers 1983).

Rupture length can also be estimated from empirical magnitude-rupture length relationships. Rogers (1983) has pointed out that often-quoted magnitude-rupture length

relationships give estimates which more than cover the range of 300 km to 470 km suggested by the two interpretations of the aftershock zone.

The shorter interpretation of the aftershock zone leaves a seismic gap of about 150 km. If this were all to rupture during one earthquake, the magnitude-fault length relationships of Iida (1965), Tocher (1958) and Acharya (1979) suggest a magnitude 7-3/4 event would occur. The amount of strain that could have been stored in the seismic gap by constant plate motion since the establishment of the Victoria seismograph station is approximately 4.5 meters (84 years X 5.5 cm/yr) (Rogers, 1983). This is equivalent to approximately a 7-3/4 magnitude earthquake. Thus, the stored strain would appear to be equal to that expected to be released during a complete rupture (Rogers, 1983). Hence the existence, or not, of a seismic gap is important for evaluation of seismic risk in the region.

1.3 THESIS OBJECTIVES

As indicated in this introduction, the August 22, 1949 Queen Charlotte earthquake plays an important role in understanding the tectonic dynamics in the Queen Charlotte Islands region. With this in mind, a closer examination of the earthquake was undertaken. There were three parts to this investigation.

1). The aftershock zone was re-examined. A detailed investigation of the aftershock zone became possible when the records from the Sitka seismic station (SIT) were found after

having been lost for many years. SIT was the closest station to the epicenter (Δ=4.0°) lying half again as close to the epicenter as the next nearest station in Victoria (VIC, Δ=8.1°). This allowed earthquakes as small as M ≥2.8 to be used to define the aftershock zone as compared to M ≥4.5 when only VIC was available.

2). To improve the reliability of the rupture length determined from the directivity function and differential phases,Love waves L2,L3, and Rayleigh waves R2,R3, recorded at Tucson (TUO), Honolulu (HON), and Pasadena (PAS) were evaluated to supplement Ben-Menahem's (1967, 1978) results.

This was done because Aki (1966), in a detailed study of the Niigata earthquake of June 16, 1964 (M=7.5), showed that the variability of phase and amplitude spectra over a narrow azimuth due to a) complexity of the source, b) interference between waves undergoing refractions due to lateral heterogeneity of the crust, and c) interference with body waves and higher mode surface waves, was significant. Aki's results indicated that the directivity function and differential phase results derived from a single station were unreliable and that better results could be obtained by averaging the results of several stations within a narrow azimuth.

3). Mechanism solutions of the two largest aftershocks were sought to help define the oblique subduction process. Forward modeling was used to obtain the azimuthal surface wave radiation patterns as a function of earthquake mechanism. These theoretical radiation patterns were then compared to the

observed radiation pattern until a 'best fit' mechanism was determined.

II. AFTERSHOCK ZONE OF THE 1949 QUEEN CHARLOTTE EARTHQUAKE

Analysis of the 1949 Queen Charlotte earthquake began with a new determination of the aftershock zone using the SIT records. The SIT records were examined for events and phase arrival picks were made. The location and magnitude of each earthquake was estimated and used to construct a revised aftershock zone.

2.1 PROCEDURE

Evaluation of the aftershock zone began with construction of a traveltime table using a layer over a halfspace model. Specifically, the standard Earth Physics Branch model was used, a_1=6.2 km/s, a_2=8.2 km/s, h=36 km, and σ=.25. A more sophisticated model derived from recordings on the mainland of explosions in Bird Lake in the Queen Charlotte Islands (Forsyth et al., 1974) produced phase arrival times only slightly different from this simple model. The slow drum speed, 15mm/min, of the SIT records precludes the ability to measure the phase arrival time accurately enough to distinguish between models. Therefore, the simpler standard model was selected.

Phase arrival picks (Pn,Pg,Sn,Sg) were achieved by selecting the most prominent arrival and assigning to it a trial phase. Assuming the phase identification was correct the traveltime table was consulted to determine when the other phases should arrive. The seismogram was then checked to see if the other phase arrivals occurred at the predicted times. If the phase arrivals did not appear at the correct times a new

phase identification of the most prominent arrival was made and the procedure repeated until the predicted and observed phase arrival times coincided.

After the phases were identified and the distance determined from the traveltime table, the local magnitude M was estimated from the log of the maximum trace amplitude and the log of the distance to the earthquake.

$$M = \log(a) + 3\log\Delta - 2.92 + \beta$$

Where a is the maximum ground amplitude in μm, Δ is in km, and β is a station correction (Kasahara, 1981).

The maximum trace amplitude was used instead of the ground displacement, with the constant multiplicative correction needed to convert the trace amplitude to the true ground displacement obsorbed into the empirically determined station correction. The station correction was determined by trying to find a correction which brought my magnitude estimates into agreement with Rogers' (1983) estimates for the 12 earthquakes we had in common. A standard deviation of σ=0.4 is found when Rogers' magnitude estimates, based on the VIC records, are compared to the station corrected SIT estimates (see Table II for a summary of the aftershock information).

After the distance of the earthquake from SIT was determined, the earthquake was arced at the appropriate distance across the Queen Charlotte fault and plotted with the assumption that it occurred on the fault (see Figure 9). The primary justification for locating the epicenters along the fault comes

from the observations that almost all the historical seismicity in the Queen Charlotte Islands region has occurred on the Queen Charlotte fault (see Figure 5). A comparison of the locations of the eight largest aftershocks, considered well located by Rogers (1983), to the SIT epicenter locations found four aftershocks located further north by as much as 50 km from Rogers' location, two located further south by five and ten kilometers, and two agreed perfectly. Rogers' epicenter locations were made using a computer program which utilized the P arrivals reported in the International Seismological Center (ISS) Bulletin and Jeffreys-Bullen (1967) travel time tables. Rogers' epicenter locations are no more accurate (±25 km) than the SIT determinations (±25 km) as he lacked good control of the origin time. Thus, disagreements of ≤50 km in epicenter locations are within the combined uncertainties of both methods and indicate that arcing the epicenters across the Queen Charlotte Fault is a valid procedure.

DATE	SITKA ARRIVAL TIME	SITKA S-P	IMPLIED SITKA DELTA	ROGERS DELTA	SITKA MAX. AMP./PER.	SITKA CODA DURATION	SITKA MAGNITUDE ESTIMATE	ROGERS MAGNITUDE
8/22	05 53 00	38?SG-PG	325KM		4MM/2SEC	120 SEC	4.4?	
8/22	06 07 05	52?SG-PN	375KM		3MM/2SEC	135 SEC	4.4?	
8/22	06 16 29	12?SG-PG	100KM		65MM?	420 SEC	3.7?	
8/22	06 50 07	16?SG-PG	125KM		2MM?	60 SEC	2.8?	
8/22	07 02 01	58?SG-PN	400KM		1MM/2SEC	140 SEC	4.0?	
8/22	07 21 55	TOO SMALL TO PICK			1MM?	100 SEC		
8/22	07 44 09	"			<.5?	48 SEC		
8/22	07 50 23	30 SG-PG	250KM		4MM/2SEC	220 SEC	4.0	
8/22	08 14 31	20 SG-PG	175KM		.5MM/1SEC	56 SEC	3.5	
8/22	08 18 40	68 SG-PG	500KM		4MM/2SEC	240 SEC	4.0	
8/22	09 08 35	40 SG-PG	340KM		2MM/4SEC	160 SEC	4.1	
8/22	09 15 15	40 SG-PN	300KM	270KM-P	12MM/1SEC	270 SEC	4.7	4.5
8/22	12 05 02	20 SG-PG	175KM		2MM/3SEC	90 SEC	3.3	
8/22	12 21 21	15 SG-PG	125KM		41.5MM/2SEC	480 SEC	4.2	
8/22	13 40 25	27 SG-PN	225KM		12.5MM/1SEC	345 SEC	4.4	
8/22	15 27 15	20 SG-PG	175KM		3MM/2SEC	90 SEC	3.4	
8/22	17 55 20	6 SG-PN	125KM		3MM/1SEC	120 SEC	3.0	
8/22	19 46 18	20 SG-PG	175KM		10MM/2SEC	250 SEC	4.0	
8/22	21 41 46	20?SG-PG	170KM		2.5MM/1SEC	120 SEC	3.3?	
8/23	00 37 48	38 SG-PG	320KM		1.5MM/2SEC	75 SEC	3.9	
8/23	01 00 09	42?SG-PN	300KM		2MM/2SEC	120 SEC	4.0?	
8/23	02 59 43	39?SG-PN	300KM	250KM-P	47MM/1SEC	600 SEC	5.3?	5.0
8/23	14 15 34	28 SN-PN	275KM		7MM/4SEC	220 SEC	4.4	
8/23	19 38 45	70?SG-PG	600KM	590KM	4MM/4SEC		5.2	5.0
8/23	19 44 46	54?SN-PN	550KM	570KM	UNREADABLE			5.0
8/23	20 25 44	50 SN-PN	500KM	545KM				6.4
8/23	23 42 44	22 SG-PG	200KM		5MM/2SEC	120 SEC	3.8	
8/24	02 39 35	? SEC TOO EMERGENT TO GUESS			2.5MM/4SEC	450 SEC		
8/24	09 21 02	46 SN-PN	450KM		4MM/4SEC	260 SEC	4.8	
8/24	12 42 48	23 SG-PG	200KM		10MM/2SEC	180 SEC	4.1	
8/24	21 52 14	40 SG-PN	300KM		5MM/2SEC	200 SEC	4.4	
8/24	22 38 24	75 SG-PN	525KM	520KM	10MM/4SEC	600 SEC	5.4	4.9
8/25	15 25 28	24 SG-PN	200KM		4MM/1SEC	105 SEC	3.7	
8/26	05 26 14	40?SG-PN	300KM	120KM-P	65MM/4SEC	23 MIN.	5.5?	4.9
8/26	22 40 19	20 PG-PN	275KM	300KM	18MM/4SEC	20 MIN.	4.8	5.0
8/27	21 31 48	44 SN-PN	425KM	475KM	6MM/4SEC	720 SEC	4.9	5.3
9/02	01 32 06	36 SN-PN	350KM	350KM	5MM/1SEC	240 SEC	4.6	4.6
9/02	05 49 21	36 SG-PN	275KM		3.5MM/2SEC	180 SEC	4.1	
9/02	07 59 52	32?SG-PN	250KM		2MM/2SEC	45 SEC	3.7?	
9/05	06 55 10	42?SN-PN	400KM	425KM-P	9MM/4SEC	300 SEC	5.0?	4.9
9/11	23 29 04	42 SG-PN	225KM		3MM/4SEC	240 SEC	3.8	
9/12	08 36 48	30?SN-PN	275KM	260KM-P	6MM/4SEC	240 SEC	4.3?	4.9
9/12	14 38 31	30?SN-PN	275KM	285KM-P	22MM/2SEC	330 SEC	4.9?	5.0
9/18	07 53 54	44?SG-PN	325KM		2MM/4SEC	120 SEC	4.0?	
9/18	11 59 44	39 SN-PN	370KM		3MM/2SEC	120 SEC	4.4	

Table II - AFTERSHOCK DATA

This table summarizes the aftershock data recorded at SIT. The ? indicates the adjacent value or reading is uncertain.

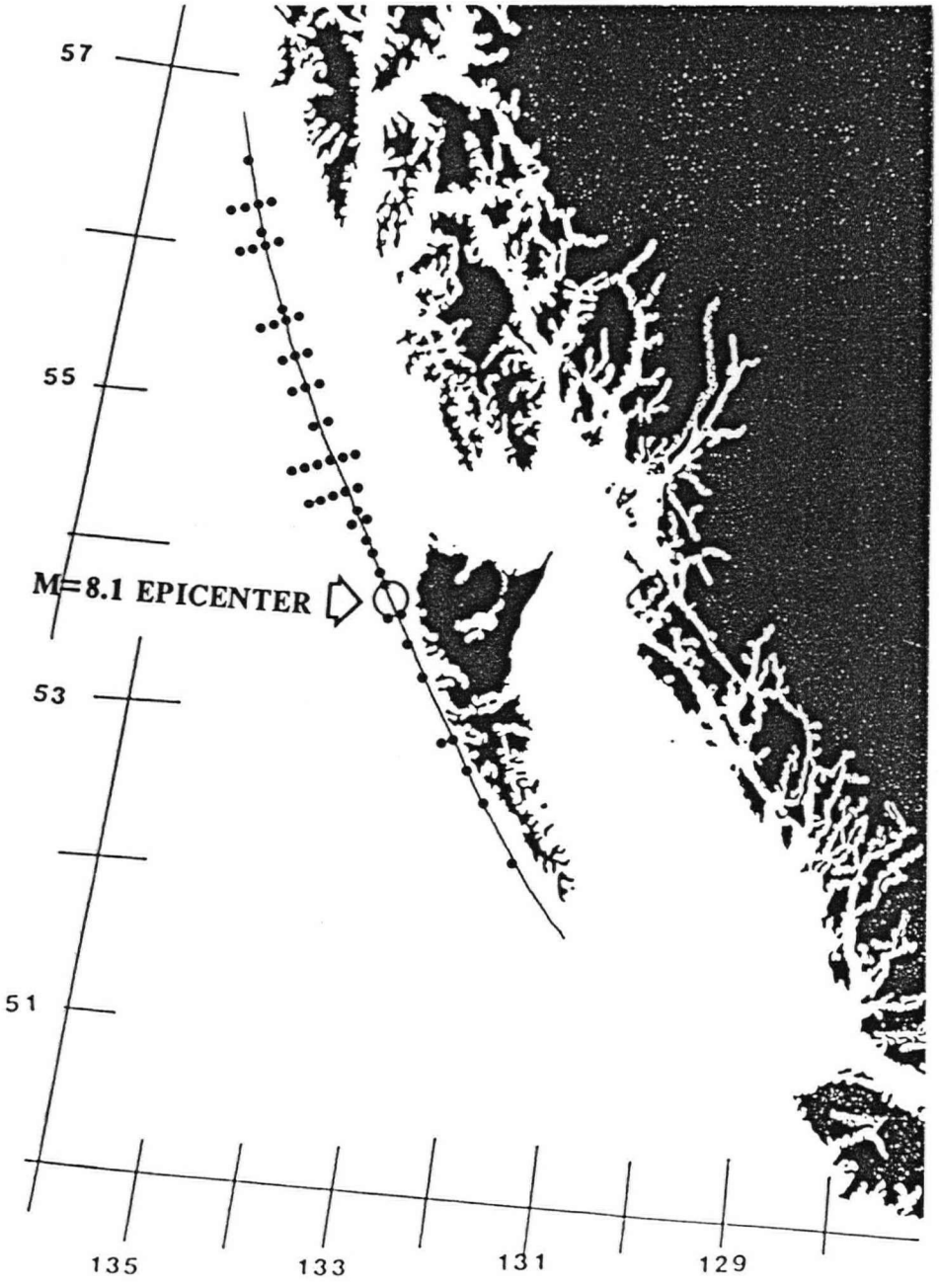

Figure 9 - AFTERSHOCK LOCATIONS

The solid dots indicate the position of aftershocks identified on the SIT records when plotted on the Queen Charlotte Fault. The lateral distribution of epicenters arranged perpendicular to the fault indicates that more than one earthquake was located at the given position on the fault. The primary justification for locating the epicenters along the fault is the observation that almost all historical seismicity in the Queen Charlotte Islands region has occurred along the Queen Charlotte fault.

An attempt was made to constrain the north-south position of the larger events more closely by moving the epicenters slightly north or south to bring the P arrival times at VIC and SIT into agreement. This procedure, applied to six of the larger aftershocks, proved inconclusive. In most cases agreement between VIC and SIT was obtained, but the nature of the seismograms prevented any significant improvement in epicenter location.

In particular, the SIT records have a low noise level and matching horizontal components. They are, however, long period with a slow drum speed (15mm/min) that makes accurate timing difficult. The VIC records consist of a short period vertical which is contaminated by considerable noise. For VIC, accurate S-P times could be determined due to the fast drum speed (60mm/min) if the arrivals of S and P are clear. However, the measured P arrival times for the M=8.1, M=6.2, and M=6.4 events do not agree with the times reported in the ISS Bulletin, which makes absolute arrival times suspect. Thus, instead of comparing P arrivals at VIC and SIT, I ended up comparing S-P times.

The level of noise, along with the emergent character of the phase arrivals at VIC, meant that the phase arrival picks were often uncertain by several seconds. In general, the apparent phase arrival times were consistent with the expected arrival times based on the SIT epicenter locations. However, the uncertainty in the precise VIC phase arrival times means that the epicenter location could vary by as much as 20 km and

still appear to satisfy the VIC phase arrival times.

Generally, however, the 15 mm/min drum speed of SIT is the main factor in limiting the accuracy of epicenter location. At best, an arrival at SIT can be identified to within 0.2 mm, which translates to an uncertainty in arrival time of 0.8 s. For an S-P time, the combined uncertainty is 1.6 s corresponding to a 15 km uncertainty in epicenter distance. Few, however, of the SIT phase arrivals can be measured to the accuracy given above; instead, an uncertainty of ±25 km is more typical. Thus, if the assumption that the epicenters lie on the Queen Charlotte Fault is valid, then epicenter locations using SIT are probably uncertain to ±25 km.

The possiblity that the earthquakes might instead lie on the Fairweather or Chatham Strait faults was also considered (see Figure 10). Although the Chatham Strait fault moved in Cenozoic time (Lathram,1964; Page,1969), there is no evidence that it is still active. No major earthquakes have occurred near the Chatham Strait fault in historic times, and there was no microearthquake activity along it during a 1969 field study (Rogers,1976; Horner, 1983). There is no direct evidence against the occurrence of the earthquakes on the Fairweather Fault. However, the complete absence of seismic activity in the SIT region for several months immediately preceding the M=8.1 event, coupled with the sudden onset of events immediately following the M=8.1 event, suggests that the earthquakes are related to the M=8.1 event, and as such, lie on the Queen Charlotte Fault and not the Fairweather Fault. The successful

cross-check with VIC of six of the earthquakes also implies that all the earthquakes lie on the Queen Charlotte fault.

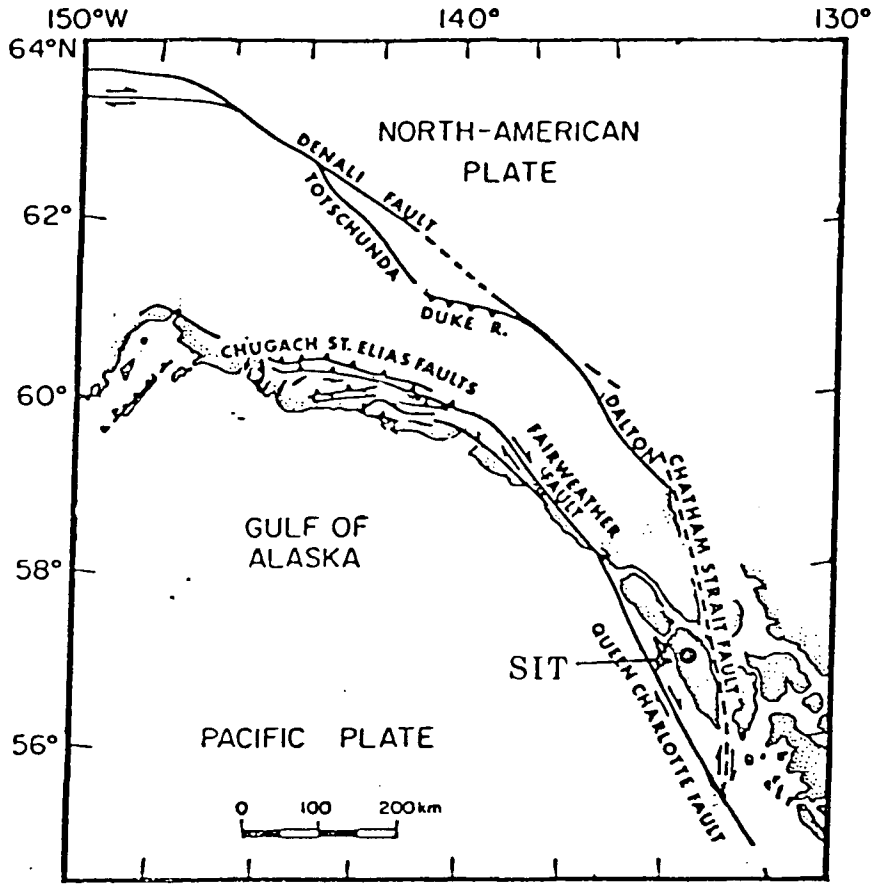

Figure 10 - RELATIONSHIP OF THE CHATHAM STRAIT AND FAIRWEATHER FAULTS TO THE QUEEN CHARLOTTE FAULT

The location of SIT is shown relative to the Chatham Strait fault and the Fairweather fault. The earthquakes are assumed to have occurred on the Queen Charlotte fault as the Chatham Strait fault shows no evidence of still being active, and the time correlation between the M=8.1 event and the other earthquakes suggests that the earthquakes are aftershocks of the M=8.1 event, and, as such, lie on the Queen Charlotte fault and not the Fairweather fault (adapted from Perez and Jacob, 1980).

2.2 RESULTS

A time history of the aftershocks is shown in Figure 11. The empirical rule for aftershock frequency first pointed out by Omori, and given in Richter (1958), is,

$$A=N(1+kt)$$

A=Number of aftershocks in a specified time interval.
k,N=Constants chosen to fit the data.

The aftershocks do appear to follow Omori's law, although the statistics are poor due to the small number of measurable earthquakes.

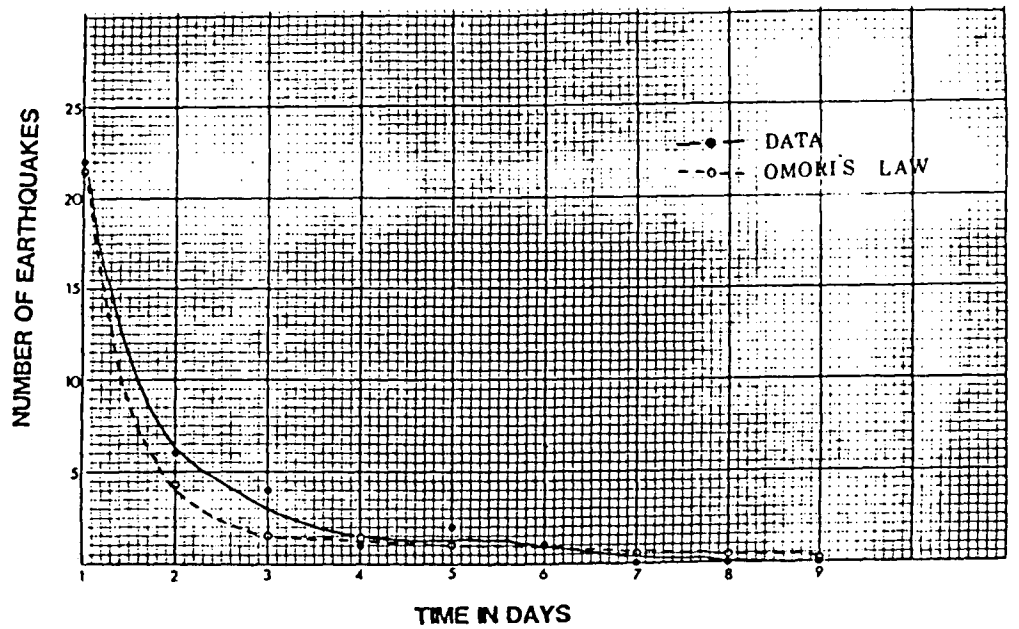

Figure 11 - TIME DISTRIBUTION OF AFTERSHOCKS

This plot shows the number of earthquakes which occurred on successive days following the M=8.1 event.

During the first six days of aftershocks the earthquakes range in location from 300 km to the north of the M=8.1

epicenter to 190 km to the south, yielding an aftershock zone of 490 km (see Figure 9).

Using primarily aftershock data to define the rupture length, Acharya (1979) derived regional magnitude-rupture length and magnitude-rupture area relationships for seven different parts of the world (see Figures 12 and 13). He found that the correlation between rupture length and magnitude is high for each region, but that variations from region to region are significant. It is not clear how much of the regional variations are due to the type of plate interaction, and how much are due to the nature of the lithosphere of the interacting plates. For instance, Acharya's relationship for the Andean subduction region is significantly different from his relationships for both the San Andreas strike-slip region and the Japan subduction region (see Figure 12).

None of the seven regions for which Acharya found magnitude-rupture length relationships match the nature and style of the Queen Charlotte Fault Zone, and, therefore, the applicability of his relationships to the Queen Charlotte fault is questionable. Likewise regional or worldwide-averaged relationships derived by other authors are of uncertain usefulness. For instance, the western U.S. relationship of Acharya (1979) predicts a rupture-length for the 1949 Queen Charlotte Islands earthquake of 301 km, but the Alaska-Aleutian relationship predicts a rupture-length of 494 km.

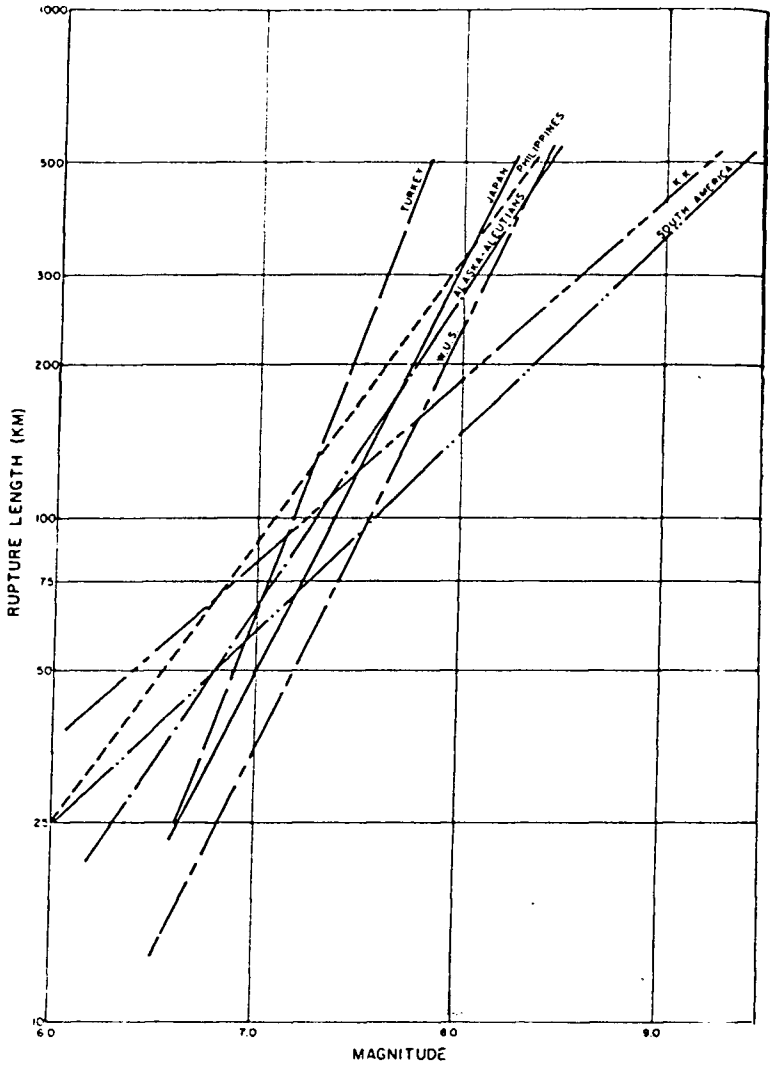

Figure 12 - EMPIRICAL MAGNITUDE RUPTURE-LENGTH RELATIONSHIP FOR 7 REGIONS OF THE WORLD

This figure shows the large variability in magnitude rupture-length relationships obtained by Acharya for different regions of the world (from Acharya, 1979).

Wyss (1978) has suggested that since long but thin faults produce less powerful earthquakes than long and wide faults, earthquake magnitude should be estimated on the basis of rupture area. The relationship suggested by Wyss, Ms=logA+4.2 where A=fault area, consistently predicts a smaller rupture area than

Acharya's magnitude-rupture area relationship for any individual region (see Figure 13). Thus, Wyss' relationship can be used to suggest a minimum rupture area for a given earthquake.

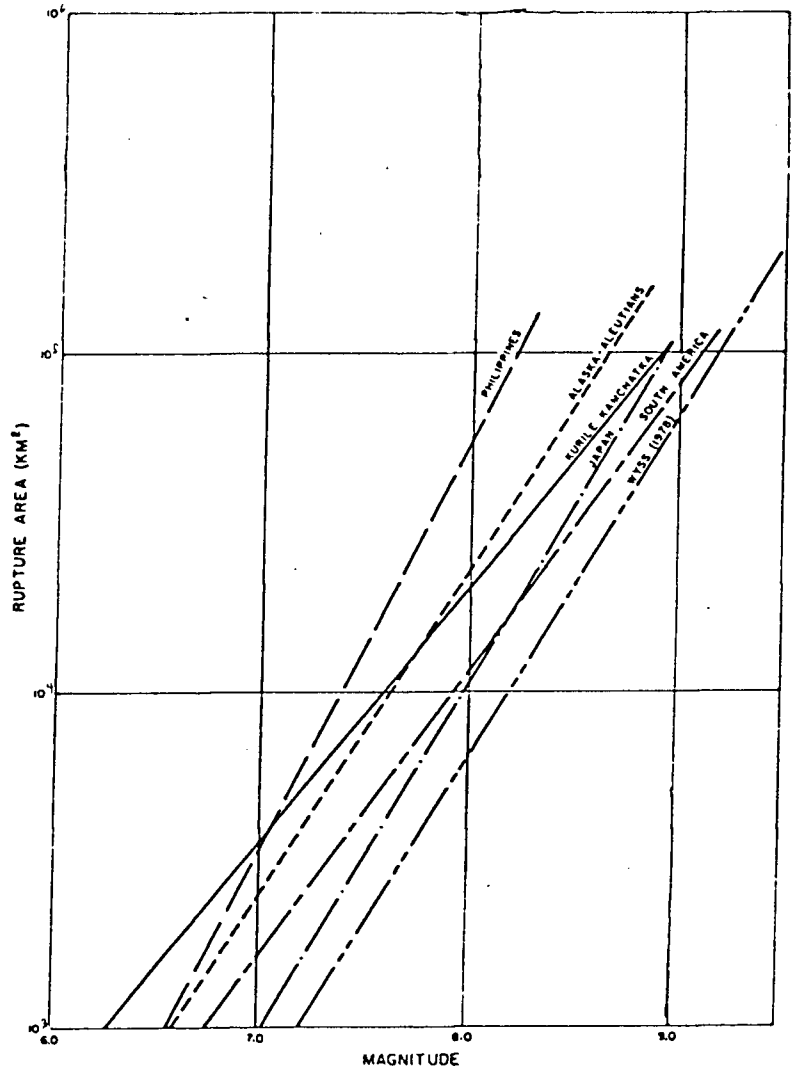

Figure 13 - MAGNITUDE RUPTURE-AREA RELATIONSHIPS

This figure shows the variability of the magnitude rupture-area relationships derived by Acharya for five different regions of the world. Note that the relationship of Wyss (1978) can be used as a lower limit for all regions (from Acharya, 1979).

For the 1949 Queen Charlotte Islands earthquake, Wyss' relationship predicts a rupture area of 7943 km^2. If this rupture area is divided by 16 km, the depth to which Hyndman and Ellis (1981) have suggested that brittle fracture can occur in the submarine terrace (the oceanward side of the presumed active Queen Charlotte fault), then the predicted rupture length is 496 km. If the width of the fault is assumed to be 21 km, the maximum observed depth of microearthquakes along the Queen Charlotte Fault (Hyndman and Ellis, 1981), then the predicted rupture length is 378 km. Bearing in mind that these numbers suggest a minimum rupture length, they are in reasonable agreement with the SIT aftershock zone. Wyss (1979), in a more recent paper in which he fits a least squares line to a selection of worldwide data, suggests the constant in the formula should be 4.15 not 4.2. With this change, a rupture length of 557 km is derived for a fault width of 16 km, and 424 km for a fault width of 21 km.

If the spatial and time development of the aftershocks are examined in detail, a distinct trend is observed. Twenty-two of the 23 earthquakes occurring in the 34 hours immediately following the main shock are located to the north of the M=8.1 epicenter, while five of eight earthquakes that occurred in the second 34 hours are located to the south of the main shock (see Figure 14). These aftershocks are caused by the slow reworking and readjustment of the strain along the fault in response to the rapid change in stress and strain of the main rupture. Apparently the reworking occurred more rapidly to the north of

the main shock epicenter than to the south. The readjustment also appears to have occurred with smaller but more numerous events to the north than to the south.

The October 31, M=6.2 earthquake, though located within the northern end of the M=8.1 aftershock zone, is separated from previous aftershocks by an absence of seismic activity for 1-1/2 months. Therefore, the October 31 shock and the three events occurring during the 34 hours immediately following it, though related to the M=8.1 event, could be considered by Kelleher's (1972) criteria to be a separate, distinct earthquake sequence at the northern end of the M=8.1 rupture zone, and not neccesarily aftershocks of the M=8.1 event. However, it is important to note that regardless of whether or not the October 31 events are considered to be aftershocks of the August 21 event, the overall aftershock zone of the August 21 earthquake does not change in size.

In summary, over 50 earthquakes were identified from the SIT records, including 38 which had not previously been recognized. The earthquakes, when plotted along the Queen Charlotte Fault indicate a rupture length of 490 km. This fault length implies that a suggested seismic gap to the north of the August 22 earthquake does not exist. The aftershock distribution also suggests a time variation in the rupture sequence, with the aftershocks clustering first to the north, and then to the south of the main shock epicenter.

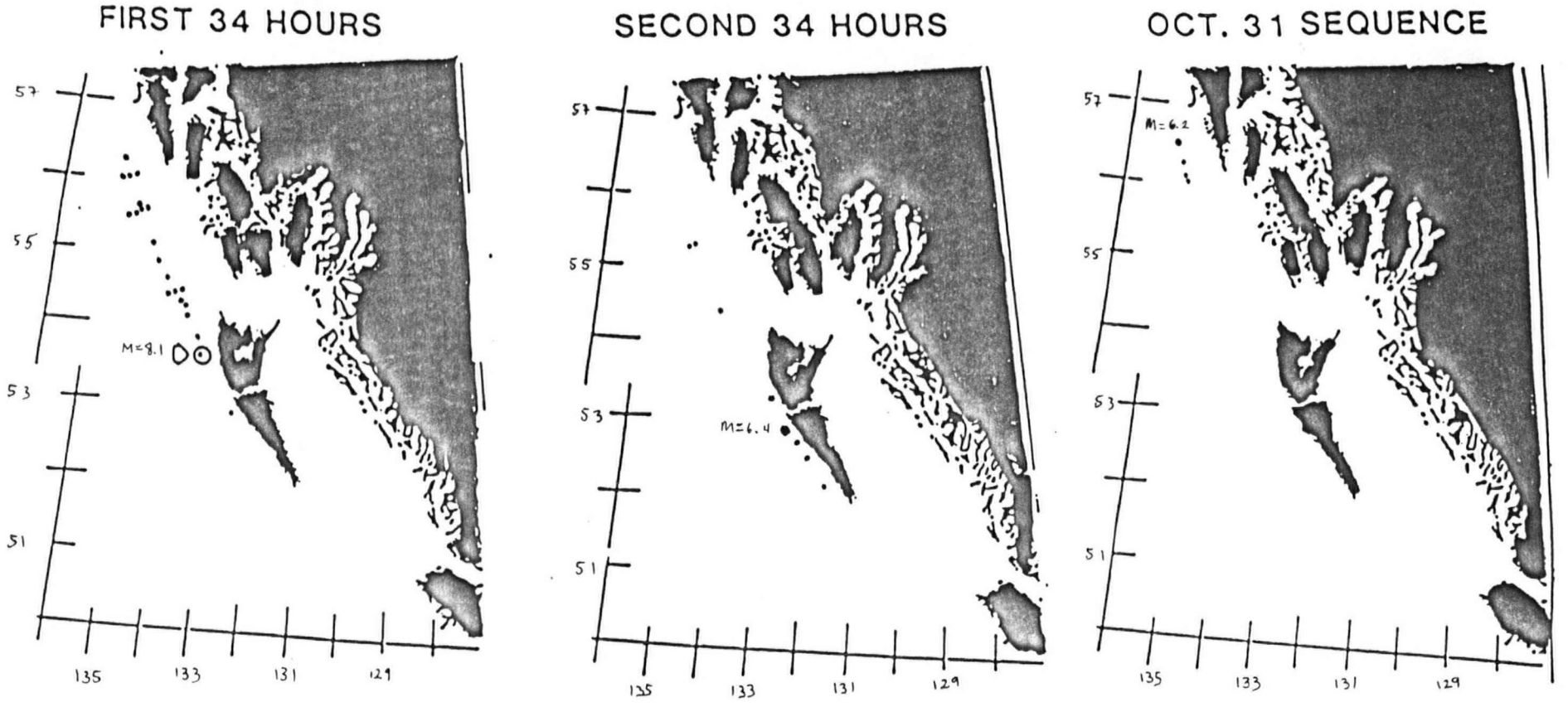

Figure 14 - TIME PROGRESSION OF AFTERSHOCKS

During the first 34 hours after the M=8.1 event, 22 of 23 earthquakes occurred to the north of the M=8.1 epicenter. During the second 34 hours, 5 of 8 earthquakes occurred to the south of the M=8.1 epicenter. The October 31 sequence is within the aftershock zone, though at the very nothern end of it, and separated in time from the other earthquakes by over a month of seismic inactivity.

III. SURFACE WAVE ANALYSIS

3.1 POINT SOURCE MECHANISM SOLUTION

3.1.1 Introduction

The azimuthal radiation pattern of Love waves and Rayleigh waves is sensitive to the earthquake mechanism and focal depth. For those earthquakes which can be represented by a point source the theoretical surface wave radiation pattern can be calculated in a straightforward manner. By comparing the calculated surface wave radiation pattern to the observed radiation pattern the earthquake mechanism and depth can be deduced. This is done by trying many different earthquake mechanisms until a mechanism and depth is found for which the calculated surface wave radiation pattern matches the observed one. For earthquakes whose spatial dimensions are small compared to the wavelength of the surface waves being analyzed, a point source approximation can be used. Applying Wyss' (1978) magnitude-rupture area relationship to a M=6.4 earthquake and dividing by 16 km for the Queen Charlotte fault, the resulting fault length is 9.9 km. Thus, if surface waves of period $\geq$20 s are analysed, the point source approximation is valid (Tsai and Aki, 1970) and can be used for the August 23 M=6.4 earthquake and the October 31 M=6.2 earthquake.

3.1.2 Theory And Computer Programs

The computer programs used to evaluate the source mechanism were developed by Herrmann (1978). These programs essentially follow Harkrider (1970) in their method of solving the differential equations which arise when trying to evaluate the theoretical surface wave amplitude spectrum recorded at a station of arbitrary azimuth and distance from a given earthquake in a layered earth.

The theory is outlined as follows:

The basic equation to be solved is Newton's second law applied within an elastic body,

$$\rho\ddot{U}=f_i+\tau_{ij} \qquad (1)$$

where,

ρ is the density
U is the ith component of ground acceleration
f is the i-th component of the applied body forces
τ is the i-th component of traction across the plane with a normal to the j-th axis.

Rayleigh wave solutions are sought of the form,

$$U=r_1(k,z,\omega)\exp(i(kx-\omega t))$$
$$V=0 \qquad (2)$$
$$W=ir_2(k,z,\omega)\exp(i(kx-\omega t))$$

With,

U=total displacement in the x direction
V=total displacement in the y direction
W=total displacement in the z direction
k=wave number

ω=frequency
$r_1(k,z,\omega)$=horizontal displacement
$r_2(k,z,\omega)$=vertical displacement

This corresponds, for positive real values of r_1 and r_2, to prograde motion in the x-z plane. The boundary conditions are,

i. Traction=0 at the free surface (z=0).

ii. No source exists at $z=\infty$.

iii. Traction and displacement must be continuous across interfaces where medium properties have discontinuities.

With these boundary conditions and the assumption that each layer is homogeneous and isotropic, the stress components become

$$\tau_{yz}=\tau_{xy}=0$$
$$\tau_{zz}=ir_4(k,z,\omega)\exp(ikx-\omega t))$$
$$\tau_{xx}=i(\lambda(dr_2/dz)+k\lambda+2\mu r_1)\exp(i(kx-\omega t)) \qquad (3)$$
$$\tau_{yy}=i(\lambda(dr_2/dz)+k\lambda r_1)\exp(i(kx-\omega t))$$
$$\tau_{zx}=ir_3(k,z,\omega)\exp(i(kx-\omega t))$$

with

$r_3(k,z,\omega)$=shear (or horizontal) stress
$r_4(k,z,\omega)$=normal (or vertical) stress
λ and μ=Lamé constants.

Substitution of (2) and (3) into (1) provides a set of differential equations for the stress-motion vector (r_1, r_2, r_3, r_4) which can be written in matrix form as,

$$\frac{d}{dz}\begin{pmatrix} r_1 \\ r_2 \\ r_3 \\ r_4 \end{pmatrix} = \begin{pmatrix} 0 & k & -\mu^{-1}(z) & 0 \\ -k\lambda(z)[\lambda(z)+2\mu(z)]^{-1} & 0 & 0 & [\lambda(z)+2\mu(z)]^{-1} \\ k^2\gamma(z)-\omega^2\rho(z) & 0 & 0 & k\lambda(z)[\lambda(z)+2\mu(z)]^{-1} \\ 0 & -\omega^2\rho(z) & -k & 0 \end{pmatrix}\begin{pmatrix} r_1 \\ r_2 \\ r_3 \\ r_4 \end{pmatrix} \quad (4)$$

The boundary conditions of vanishing traction at the free surface z=0 and no motion at z=∞

$$\text{i.e.} \quad r_1, r_2 \longrightarrow 0 \text{ as } z \longrightarrow \infty$$

$$r_3, r_4 \longrightarrow 0 \text{ as } z = z_0 = 0$$

mean that for a given ω nonvanishing solutions exist only for certain $K=Kn(\omega)$ (Aki and Richards, 1980). Phase velocity $Cn=\omega/Kn(\omega)$ is also discretized.

This is an eigenvalue-eigenfunction problem. The first computer program, SURFACE, takes as input an earth model and a selected range of frequencies for which the eigenvalues or phase velocities are to be determined. To find the solution to this eigenvalue problem in a multilayered medium, a Thompson-Haskell matrix formulation (Haskell, 1953) is used. In this method it is assumed that the medium parameters remain constant within a given layer so that a matrix operator can be derived which relates the stress-motion vector at one side of an elastic solid layer to the vector at the other side of the same layer. Repeated application of this method allows one to start at the

halfspace at the bottom and work up to the surface layer-by-layer.

Briefly, the computation proceeds by applying a series of matrix transformations to Equation (4) to obtain a homogeneous matrix equation known as the frequency or period function. The frequency function is solved by seeking the zeros of the equation as a function of phase velocity, wave number, and the elastic constants of the layers. This is done by initially specifying the wave number, Kn, and a trial phase velocity, Cn. The elements of the Thompson-Haskell matrix are then formed for each layer and multiplied by the matrix for the layer above it, starting with the half space. The numerical value of the frequency function is calculated from elements of the final product matrix and stored.

The frequency function has the important feature that its values are positive for Cn's larger than the root in the lowest mode. A new trial value of Cn is chosen (larger or smaller depending on whether the sign of the frequency equation is positive or negative) until a change in sign of the frequency equation is detected. After the root is bracketed an interval halving procedure is used and then finally a linear interpolation scheme is followed to produce Cn to the required accuracy. The resulting eigenvalue, Cn, is passed to a second program, REIGEN, which numerically integrates Equations (4) from the bottom up to find the eigenfunction (r_1, r_2, r_3, r_4) as a function of depth. A similiar set of equations and procedure is followed for Love waves.

The eigenvalues and eigenfunctions are earth model dependent but not source or station dependent. Once the appropriate earth model has been selected both programs are run, and the resulting eigenvalues and eigenfunctions are stored.

The third computer program, WIGGLE, takes the eigenvalues and eigenfunctions stored on tape and computes the surface displacement at an arbitrary point for a point source at a selected depth. Using the eigenvalues and eigenfunctions the impulse response of the medium, the Green's functions, can be evaluated. The Rayleigh Green's function for a point force F(w) acting at $\xi(0,0,h)$ is (Aki and Richards, 1980),

$$G_{Rayleigh} = \sum_n \frac{1}{8CU_g I} \begin{pmatrix} r_1(z)r_1(h)\cos^2\phi & r_1(z)r_1(h)\cos\phi\sin\phi & -ir_1(z)r_2(h)\cos\phi \\ r_1(z)r_1(h)\sin\phi\cos\phi & r_1(z)r_1(h)\sin^2\phi & -ir_1(z)r_2(h)\sin\phi \\ ir_2(z)r_1(h)\cos\phi & ir_2(z)r_1(h)\sin\phi & r_2(z)r_2(h) \end{pmatrix} \left(\frac{2}{\pi k_n r_1}\right)^{1/2} \exp\left[i\left(k_n r + \frac{\pi}{4}\right)\right]$$

where we have transformed into a more appropriate cylindrical polar coordinate system.

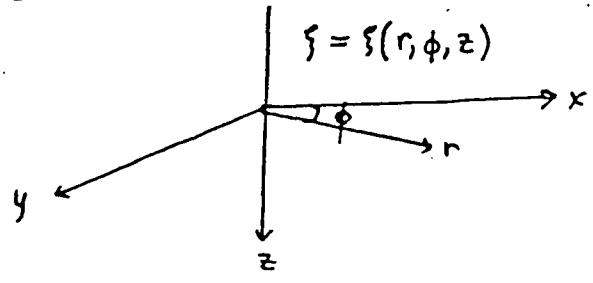

I in this equation is given by,

$$I = 1/2 \quad \rho(r_1 + r_2)dz$$

and the group velocity, Ug, is determined by differentiating Cn.

The computer program is written in terms of equivalent body forces; however, for this outline the results can be obtained

faster by using the moment tensor formulation (see Aki and Richards, 1980).

$$U_i(\vec{X},\omega) = M_{pq}(\omega)\, \partial/\partial\xi\, G_{ip}(\vec{X},\xi,\omega)$$

where

U =i-th component of receiver displacement
X=the vector position of the receiver
Mpq=elements of the moment tensor
Gip=elements of the Green's function (i-th component of displacement due to an impulse force in the in the p-th direction).

In differentiating the Green's function only the largest or far field terms are retained. The moment tensor components M_{pq} can be computed from the earthquake fault parameters (eg., Box 4.4 in Aki and Richards, 1980).

The program QUESTION accepts the observed azimuthal variation Love and Rayleigh wave amplitude spectra for an earthquake. The program then searches through a parameter space of focal mechanism orientations and focal depths, and computes several goodness-of-fit characteristics which are used to determine the best focal mechanism and focal depth combination which satisfies the observations. These goodness of fit characteristics include:

a) The correlation coefficient between the observed and theoretical Rayleigh or Love wave amplitude spectra for the totality of data from all azimuths and periods.

b) Seismic moment estimate from Love waves.

c) Seismic moment estimate from Rayleigh waves.

d) Sum of square residuals between observed and theoretical Rayleigh wave amplitude spectra using the average seismic moment estimate.

e) Square root of the sum of Love and Rayleigh wave square residuals.

The best focal mechanism estimate is usually the one with the largest correlation coefficents and for which the two independent seismic moment estimates are as equal as possible. Other programs are available to plot and display the results from this program.

3.2 RUPTURE PARAMETERS

3.2.1 Introduction

For large earthquakes the point source approximation is no longer valid as the surface wave radiation pattern is affected by the large spatial extent of the earthquake. The finite dimensions of an earthquake introduce an asymmetry into the surface wave radiation pattern. This asymmetry corresponds to the doppler effect from a moving point source. By analysis of the asymmetry, the earthquake rupture length and rupture velocity can be derived. Both rupture length and rupture velocity are parameters of interest for the M=8.1 earthquake and can be derived for this earthquake as it is sufficiently large that the asymmetery in the surface wave radiation pattern is large and easily measured.

Ben-Menahem (1961) was the first to describe the effect on the far-field surface wave amplitude spectrum of rupture propagation along a fault. He did this by examining the far-field displacement caused by a moving horizontal dipole with harmonic time dependence in a layered elastic halfspace. For a vertical strike-slip fault of vertical extent d, which propagates along a fault of length b with velocity v, he found the far-field vertical Rayleigh wave displacement U to be given by,

$$U(\omega)=(\sin(2\theta)/\sqrt{r})(g(\omega)k(\sin(X)/X)\exp\{i(\phi+3\pi/4)\}$$

$$\text{where } X=(\pi b/\lambda)(c/v-\cos\theta) \qquad (5)$$

$$\phi=\omega(t-r/c)-X$$

and where c is the Rayleigh wave phase velocity, r the epicentral distance, θ the azimuth to the station measured counterclockwise from the strike of the fault and k the wave number of shear waves. $g(\omega)$ is a function which depends on the source time function, the width of the fault, depth and frequency.

For our purposes, two components of this expression are useful for examination of the 1949 earthquake.

3.2.2 Directivity Function Theory

The effect of the finite dimensions is contained in the term X. The effect of the finiteness of the fault on the amplitude spectrum is expressed by the factor sin(X)/X which has nodes at $X=\pi,2\pi,3\pi,\ldots$

To isolate the effect of the finite dimensions, Ben-Menahem (1961) defined the directivity function as the ratio of the spectral amplitudes leaving the source at azimuth θ to those leaving the source with azimuth $\theta+\pi$.

$$\text{directivity function} = |U(\omega)[\theta)]| \;/\; |U(\omega)[\theta+\pi]|$$

$$\left| \frac{(c/v+\cos\theta)\sin\{(\omega b/2c)(c/v-\cos\theta)\}}{(c/v-\cos\theta)\sin\{(\omega b/2c)(c/v+\cos\theta)\}} \right|$$

For a pure strike-slip fault this function is independent of dip angle, source time function, or the layering of the elastic half space model. For a pure dip-slip fault this function is undefined. When only one station is available, a trial and error approach is used to generate theoretical directivity curves until a combination of rupture velocity and rupture length is found which produces a directivity curve that best fits the observed curve.

With more than one station, a least squares technique can be used. The first extremum will occur when $X=\pi$.

$$X=(\pi b/\lambda)(c/v-\cos\theta)=\pi$$

This can be rewritten as

$$\lambda/c=(b/c)(c/v-\cos\theta)=T(max)$$

which corresponds to the maximum period at which an extremum will occur. This can again be rewritten as,

$$b=T(max)c/(c/v-\cos\theta)=T(max)/(1/v-\cos\theta/c)$$

If the following substitutions are made,

$$x=T(max),\ y=\cos\theta/c,\ a=b,\ B=1/v$$

then,

$$a=x/(B-y)$$

or,

$$y=-(1/a)x+B = Ax+B \qquad A=-1/a=-1/b.$$

Each station can be plotted as a point with an x value equal to the maximum period at which an extremum occurs, and the y value equal to $\cos\theta/c$. A least squares line through the points can be determined with the negative reciprocal of the slope yielding the rupture length, and the reciprocal of the y-intercept giving the rupture velocity.

Thus, to use this method, one forms the observed directivity function curve by taking the spectral amplitude ratio of R2 and R3. A graph is then constructed with one point plotted for each station. The y value for a given point is the maximum period at which an extremum occurs in the observed directivity function (Tmax). The x value is the cosine of the azimuth to the particular station divided by the phase velocity corresponding to Tmax. A point is plotted for each station and a least squares line drawn through the resulting array of points. The negative reciprocal of the slope of the least squares line will give the rupture length. The reciprocal of the y-intercept will give the rupture velocity.

3.2.3 Differential Phases Theory

The effect of the finite fault dimensions on the phase spectrum can also be utilized. The difference in phase of waves radiating into opposite azimuths is given from (5) as

$$\Delta\phi=\phi(\theta)-\phi(\theta+\pi)$$

$$=\{\omega(t_1-r_1/c)-X_1\}-\{|\omega(t_2-r_2/c)-X_2\}$$

where t_1 = time for the wave to travel from the focus to the station at θ

t_2 = time for the wave to travel from focus to the station at $\theta+\pi$
r_1 = the distance to station θ
r_2 = the distance to station $\theta+\pi$
$X_1 = (\pi b/\lambda)(c/v-\cos\theta)$
$X_2 = (\pi b/\lambda)(c/v-\cos\theta+\pi)$.

This can be rewritten as,

$$\Delta\phi=(1/\lambda)(40,000-2r_1+b\cos\theta)+m+1/4. \qquad (6)$$

The $40,000-2r_1$ and $m+1/4$ terms are propagation terms which arise from the fact that the two waves must travel different distances to reach the recording station. By correcting the phase of each wave train for propagation effects we obtain the initial focal phase,

$$\phi(\text{focal})=\phi(\text{FFT})-\phi(\text{dispersion})-\phi(\text{digitization})-\phi(\text{instrument}).$$

In this process, we subtract from the phase part of the Fourier transformed seismogram ϕ(FFT) all phase advances (taken as positive). The ϕ(dispersion) term is the compensation for dispersion which a wave experiences when it travels a distance Δ km with a phase velocity C.

$$\phi(\text{dispersion})=f\Delta/C$$

where f is frequency, C is phase velocity and Δ is measured in km.

The ϕ(digitization) term accounts for the difference between the origin time of the earthquake and the fiducial time at which the beginning of the digitizing window was chosen.

$$\phi(\text{digitization})=fT_0$$

where T_0 is the time delay from the earthquake origin time to the start of digitization.

The ϕ(instrument) term is the correction for the phase response of the seismograph.

Once the focal phase for each wave is obtained the difference is taken.

$$\phi_1(\text{focal})-\phi_2(\text{focal})=\Delta\phi(\text{focal})$$

The propagation terms in Equation (6) have been subtracted out in obtaining the focal phases. Therefore the differential focal phases will be from Equation (6),

$$\Delta\phi(\text{focal})=b\cos\theta/\lambda$$

from which the rupture length, b, can be derived.

$$b=\lambda\Delta\phi(\text{focal})/\cos\theta$$

Unlike the directivity function, this method provides an estimate of the rupture length which is independent of the rupture velocity.

3.3 PROCESSING

3.3.1 Data Acquisition

The data were obtained by writing to stations and networks known to be operating relatively long period instruments in 1949, and to the World Data Center A for copies of relevant records from long period stations in their film library. There was variety in the type of seismogram copies sent by the responding stations. In some cases full sized copies were sent, but in most cases photographic copies on microfilm were received. Unfortunately, not all of the stations responded,

and, of those that did respond, not all sent seismogram copies. Often important instrument parameters such as seismometer period and static magnification were not included with the station responses. Even when this information was included the reliability of the quoted parameter values was frequently questionable. Without this information the seismograms were of little use (for a complete list of stations requested and their replies, see Appendix A).

In total, the data collected represent a menagerie of seismograph instrument types, instrument periods, and hard copy record styles. In all cases, original records provided the most information. The full sized photocopies, though generally useful, tended to have two problems. In some cases simply poor photocopying was the problem, too light and smudged to be useful. A more subtle problem with them was that an edge or end of the seismogram would sometimes be clipped off.

Microfilm presented problems too. Because of the limitations of the department dark room facility, it was not possible to make full sized seismogram copies on only one print. Instead, a series of prints had to be made, each of only one section of the seismogram. These sections were then overlapped and taped together to reassemble the full sized seismogram. Despite efforts to avoid it, skews could easily develop in the seismic trace in the process of reconstructing the full sized seismogram. An occasional problem with the microfilm was that some of the seismograms had their edges curled under when microfilmed.

Of more than 30 stations originally requested only eight stations were eventually used. Only three stations were suitable for use in finding the directivity function and differential phases, and only five and eight staions could be used in determining the surface wave radiation pattern of the August 23 and October 31 earthquakes, respectively. A problem with all stations was the lack of true long period instruments (the response curves for the eight stations used in this thesis are shown in Appendix D). The low power for long periods meant that the useable signal was effectively bandpassed for short periods by scattering due to inhomogeneities in the crust and for long periods by attenuation due to instrument response.

3.3.2 Data Processing

The data processing began with digitizing the seismic records within group velocity windows. The windows were selected after consulting world averaged group velocity tables for Love and Rayleigh waves (Kovach, 1965). The windows were chosen to contain Love and Rayleigh wave arrivals for periods between 10 s and 300 s. The digitizing window was typically between 4.5 km/s and 2.5 km/s for the August 23 (M=6.4) and October 31 (M=6.2), earthquakes, and between 3.9 km/s and 3.5 km/s for Rayleigh waves and between 4.5 km/s and 4.2 km/s for Love waves of the August 21 (M=8.1) earthquake. Full size plots were made and placed over the original to check the faithfulness of the digitization.

After digitization, the time series was interpolated to a

sampling interval of 2 s, and the trend and the d.c. offset removed. The time series was then transformed into the frequency domain where instrument corrections were applied and the NS and EW components rotated into radial and tangential parts. In all cases the instrument response was calculated with critical damping assumed. For electromagnetic seismometers, there was assumed to be no feedback coupling between the galvanometer and the seismometer. These processes were performed by Herrmann's (1978) program EXSPEC.

3.3.3 Amplitude Data

The Fourier transformed ground motion which resulted from the use of EXSPEC was next passed to Herrmann's program FILTER. This program applied a narrow bandpass Gaussian filter to the real frequencies of the Fourier transform of the ground motion. The inverse Fourier transform was then taken and the envelope of the filtered signal found by using both the real and imaginary components of the inverse transform. This envelope was plotted as a function of the group velocity, and the center period, To, of the filter passband. The envelope was searched for local maximums, which, as long as two or more modes do not arrive too close together, will reflect the spectral amplitudes of the various modes making up the signal. The peak of the envelope was multiplied by a factor of 4To, so the result was dimensionally a spectral amplitude. This procedure was repeated for a range of center periods so that the resulting plot represented a form of the group velocity dispersion curve.

Essentially the plot shows the amount of energy arriving at a given group velocity versus the energy's period. The result of this filtering is the ability to identify the various mode arrivals and obtain their spectral amplitudes as a function of period.

FILTER as it was originally written by Herrmann (1978) displayed the filtering results by tabulating a list of all the local spectral amplitude maximums. The spectral amplitude maximum was listed along with the period and group velocity for which the local maximum occurred. While this method of displaying the results gave all the needed facts, it was difficult to identify patterns in the local maximums and to distinguish the arrivals of different modes. The output was therefore modified to include the plots mentioned above. These plots made it easier to associate a given local spectral amplitude maximum with a specific mode arrival.

Once identified and obtained, the spectral amplitudes were corrected for amplitude decrease due to anelastic attenuation and geometrical spreading to a selected reference distance.

$$\text{Amp(corrected)}=\text{Amp}(\sin(\Delta_1/\Delta_2)^{0.5}\exp(-(\Delta_1-\Delta_2)\gamma)$$

where Δ_2 is the reference distance and γ is the attenuation factor given by

$$\gamma=\pi/QTU$$

with Q=quality factor
T=the period
U=the group velocity.

For the August 23 and October 31 data, the reference distance was 1000 km as only R1 and L1 data were used. For the August 22

data, the reference distance was 39960 km, which is approximately half way between the distance the R2 and R3 or L2 and L3 waves must travel.

The corrected amplitudes were then used in ratios to form the directivity function or plotted azimuthally to derive the radiation pattern.

3.3.4 Phase Data

After circling the Earth once or twice the wave trains of the August 22 data consist almost exclusively of the fundamental mode, the higher modes having been attenuated. With this in mind, the phase part of the Fourier transform of the ground motion was used without bandpass filtering. To obtain the focal phase the observed phase was corrected for the time delay due to the start of digitization and the phase delay due to propagation from the source to the receiver. Corrections for the phase delay caused by polar crossings (Aki, 1966) were also made.

$$\phi(\text{focal})=\phi(\text{FFT})-\phi(\text{dispersion})-\phi(\text{instrument})-\phi(\text{digitization})$$

By taking the difference of the focal phase between waves radiated into opposite azimuths, the rupture length of the generating earthquake was derived using equation (6).

IV. RESULTS FOR THE M 8.1 EARTHQUAKE OF AUGUST 22

The methods of differential phases and directivity require a wave pair of oppositely traveling waves. Unfortunately, for the August 22 M=8.1 earthquake almost all of the stations had L1 and R1 arrivals off scale and L3 and R3 arrivals either indiscernible or too small to be useful. Only three stations had the required wave pairs clear and on scale. At Tucson (TUO), both Rayleigh wave (R2,R3) and Love wave (L2,L3) pairs were obtained. For Pasadena (PAS), Love waves (L2,L3) were obtained on the Wood-Anderson instruments, but the R3 arrivals were too small for Rayleigh waves to be used. At Honolulu (HON), only Rayleigh waves (R2,R3) were used as the L2 waves were off scale.

The digitized seismograms are shown in Figure 15 and 16. The group velocity curves are shown in Figures 18 and 19 respectively. Over the period range 50-210 seconds the dispersion curve should be relatively flat with a gentle valley around 200 seconds (see Figure 17). The fundamental mode was identified by looking for a series of arrivals that smoothly varied and which arrived with a group velocity close to the expected group velocity. It turned out that the largest of the local energy maximums for a given period was usually chosen as the fundamental mode arrival. The dispersion curve data appears to be affected by scattering with large holes of energy and a general ragged appearance.

The dispersion curves do not closely resemble those shown in Figure 17. There are several reasons for this. First, the

curves shown in Figure 17 are smoothed with the data points scattering about the smoothed curves. Second, scattering of the shorter period waves by crustal inhomogeneities affects the short period part of the dispersion curves. Third, the low power at long periods of the seismographs means that the amplitude of the seismic signal tends to be down at the normal seismogram noise level, and hence the long period part of the dispersion curve is infected with noise.

These curves give the best indication of the quality of the data and indicate how not having true long period seismographs limits the amount of long period surface wave analysis which can be done.

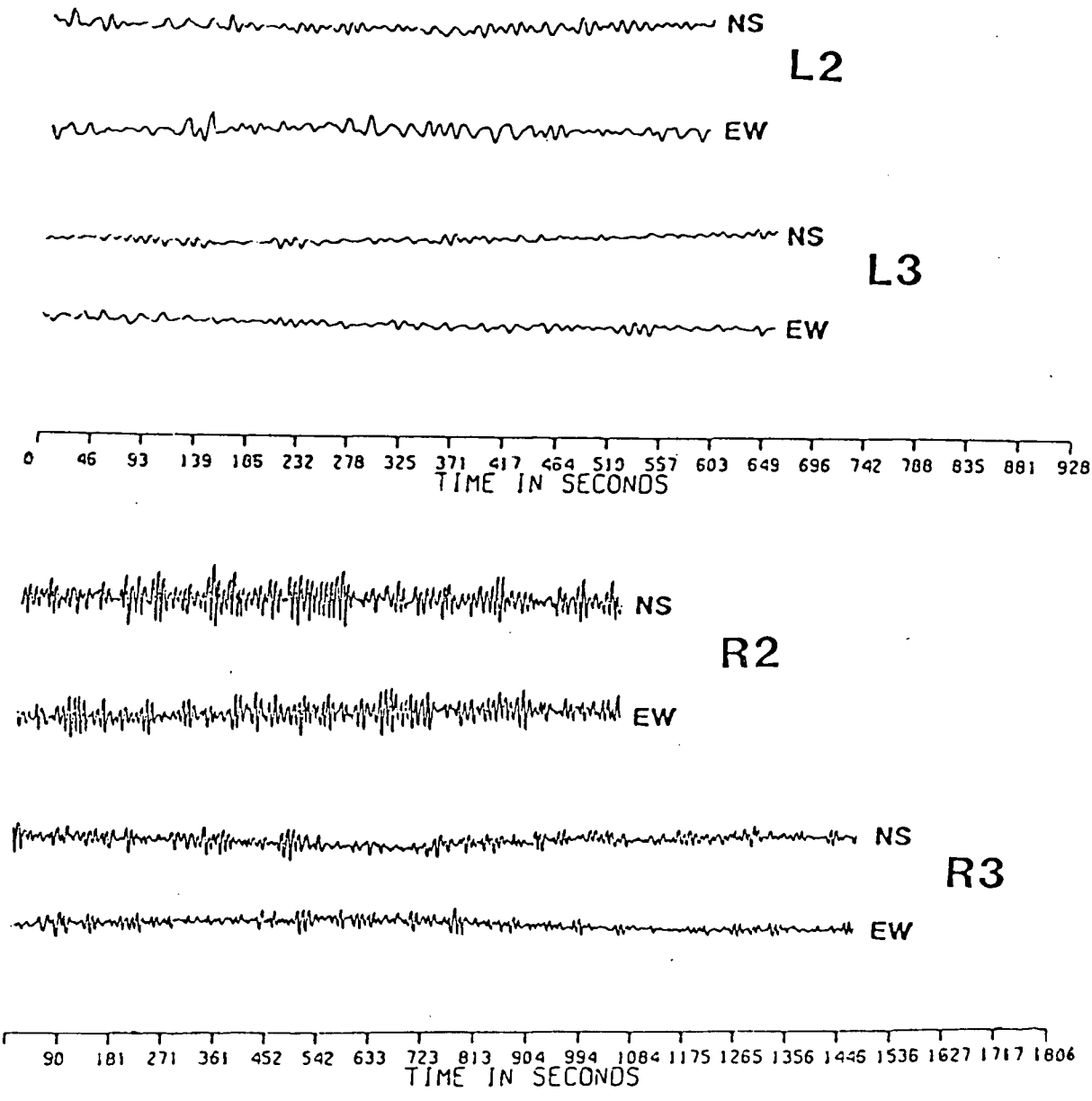

Figure 15 - DIGITIZED TUO SEISMOGRAMS FOR THE AUGUST 22 EARTHQUAKE (M=8.1)

There is a 4.5:1 vertical exaggeration as the time scale has been divided by 4.5 to allow plotting of the whole seismogram on one page. The seismograms have been reduced in scale as well. The amount of reduction can be determined by noting that before reduction the time scale marks were 1 cm apart.

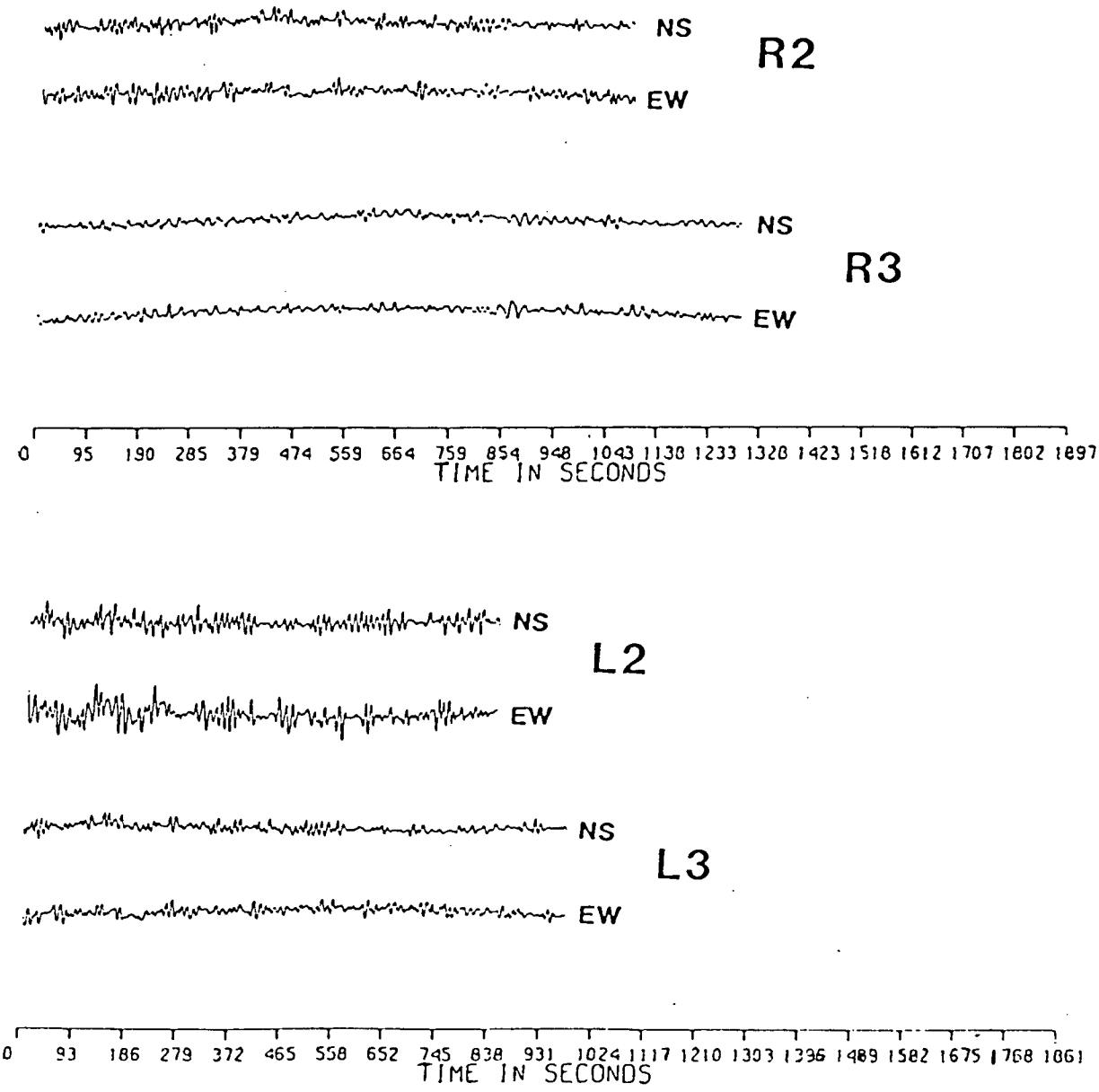

Figure 16 - DIGITIZED PAS AND HON SEISMOGRAMS FOR THE AUGUST 22 EARTHQUAKE (M=8.1)

The upper set of seismograms were recorded at HON, the lower set on the PAS Wood-Andersons. In all cases there is a 4.5:1 vertical exaggeration as the time scale has been divided by 4.5 to allow plotting of the whole seismogram on one page. The seismograms have been reduced in scale as well. The amount of reduction can be determined by noting that before reduction the time scale marks were 1 cm apart.

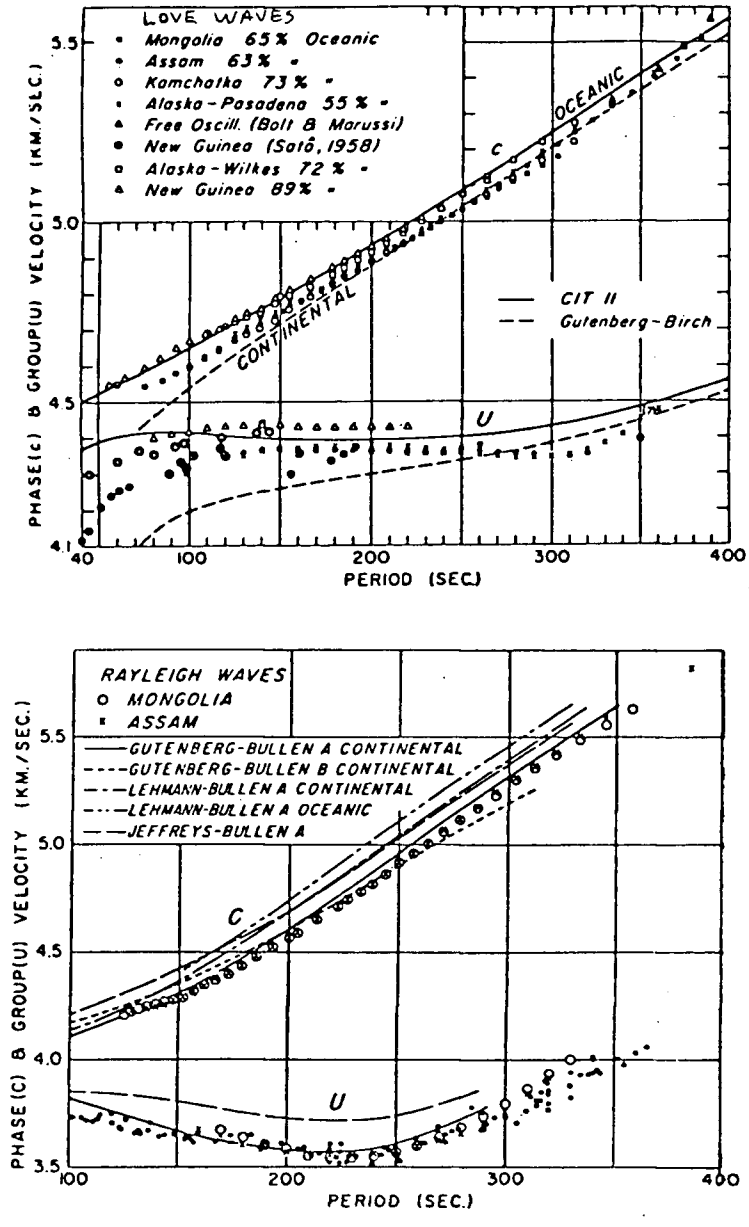

Figure 17 - TYPICAL GROUP VELOCITY CURVES FOR LOVE AND RAYLEIGH WAVES

These plots show surface wave group velocity curves (U) obtained by various investigators. These curves provide a standard against which the group velocity curves for the August 22 data can be compared (adapted from Kovach, 1965).

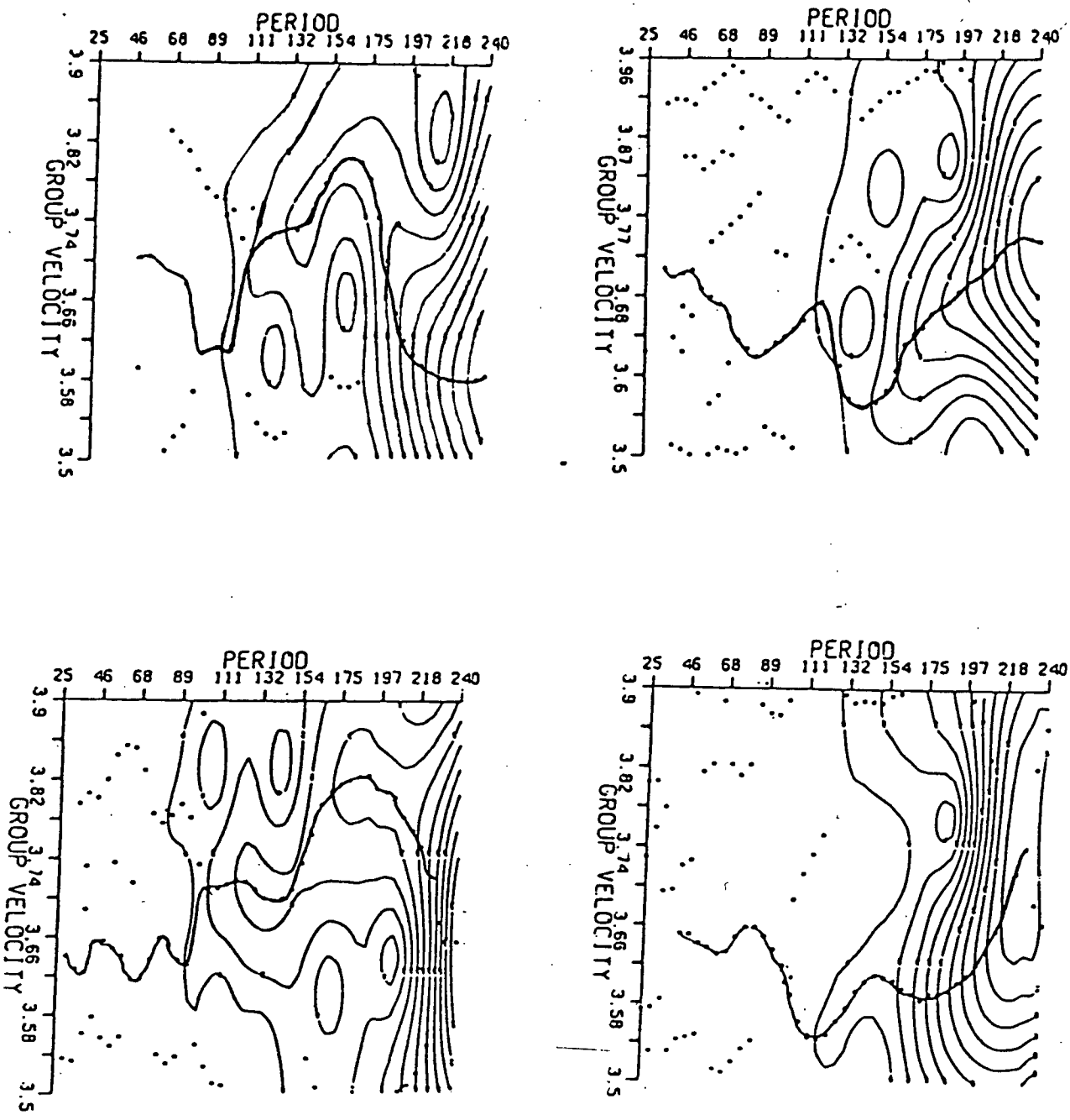

Figure 18 - GROUP VELOCITY CURVES FOR THE AUGUST 22 DATA

The upper pair of plots are of the Rayleigh data recorded at HON. The lower pair of plots are of the Rayleigh data recorded at TUO. The dots are the positions of local maximums in the spectral amplitude. The solid line indicates the energy arrivals selected as corresponding to the fundamental mode. The curves do not closely resemble the standard ones shown in Figure 17, indicating how strongly the data are affected by crustal scattering at short periods and instrument response at long periods.

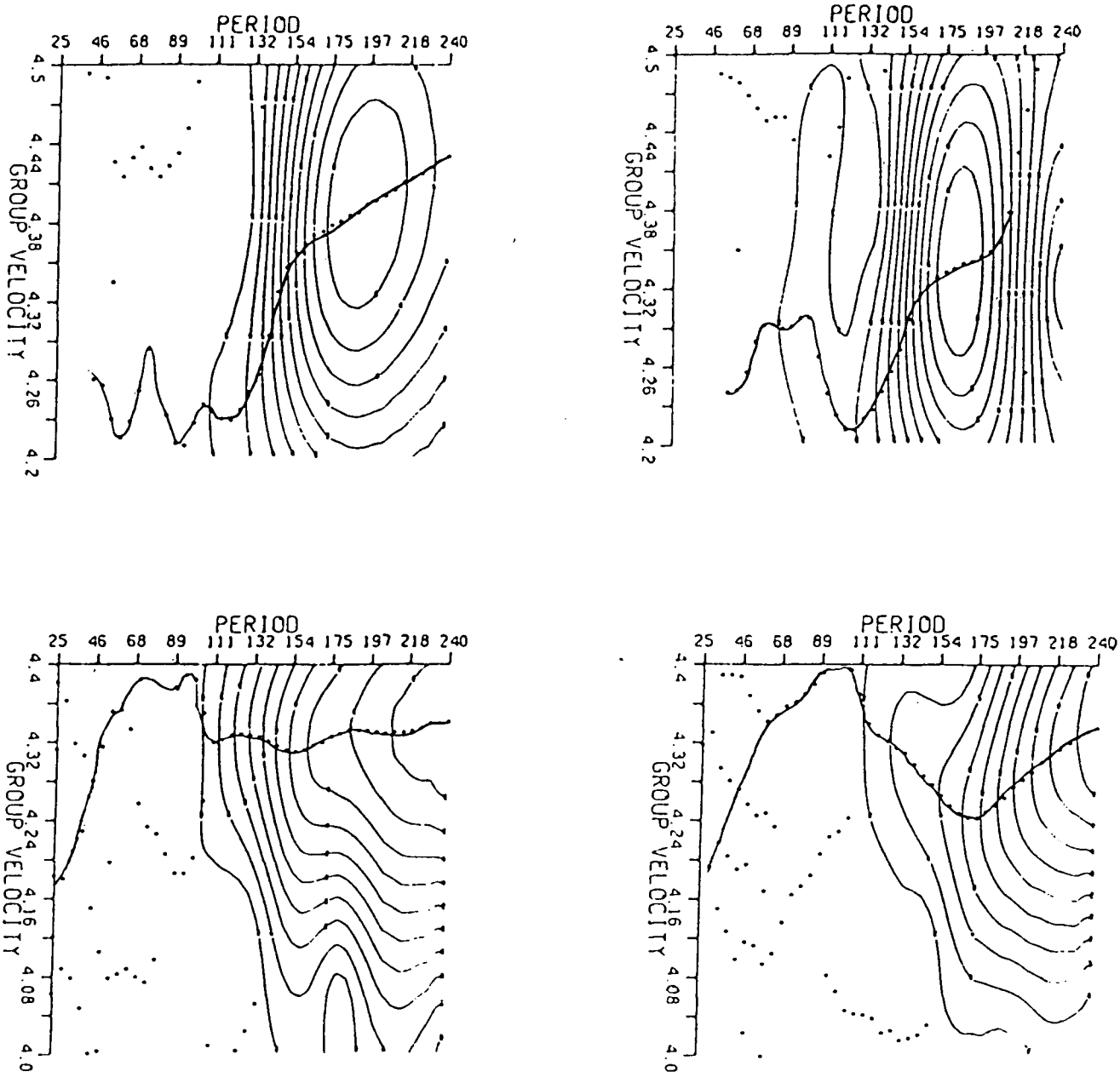

Figure 19 - GROUP VELOCITY CURVES FOR THE AUGUST 22 DATA

The upper pair of plots are of the Love data recorded at PAS. The lower pair of plots are of the Love data recorded at TUO. The dots are the positions of local maximums in the spectral amplitude. The solid line indicates the energy arrivals selected as corresponding to the fundamental mode. The curves do not closely resemble the standard ones shown in Figures 17, indicating how strongly the data are affected by crustal scattering at short periods and instrument response at long periods.

4.1 DIRECTIVITY FUNCTION

The directivity function was derived by taking the ratio of spectral amplitudes of oppositely traveling waves as measured on the same instrument. This meant that inaccuracies in correcting for instrument parameters and calibration were canceled out, a significant advantage when instrument magnifications are not accurately known. Phase velocities and Q values were taken from averaged whole world paths (see Appendix B). Theoretical directivity function curves were computed and compared to the observed directivity function until the combination of rupture length and rupture velocity was found which gave the best match between the observed and theoretical curves. It was found that increasing the size of the rupture length, b, moved the location of the Tmax extremum to longer periods and introduced new extremes in the short period range. Increasing the rupture velocity, Vr, moved the Tmax extreme to shorter periods and widened the spacing between extremes.

The best fit was obtained with a rupture length of 265 km and a rupture velocity between 3.1 km/s and 3.5 km/s (see Figure 20). The key features of the best fit theoretical curves are similiar to the observed curves. In particular, the local maximums and minimums of the observed and theoretical curves appear at approximately the same place with the exception of the local maximum in the observed curves around 75 seconds which is not seen in the theorectical curves of PAS and TUO (Rayleigh), or a similiar discrepancy around 100 seconds for HON. The biggest difference between the observed and theoretical curves

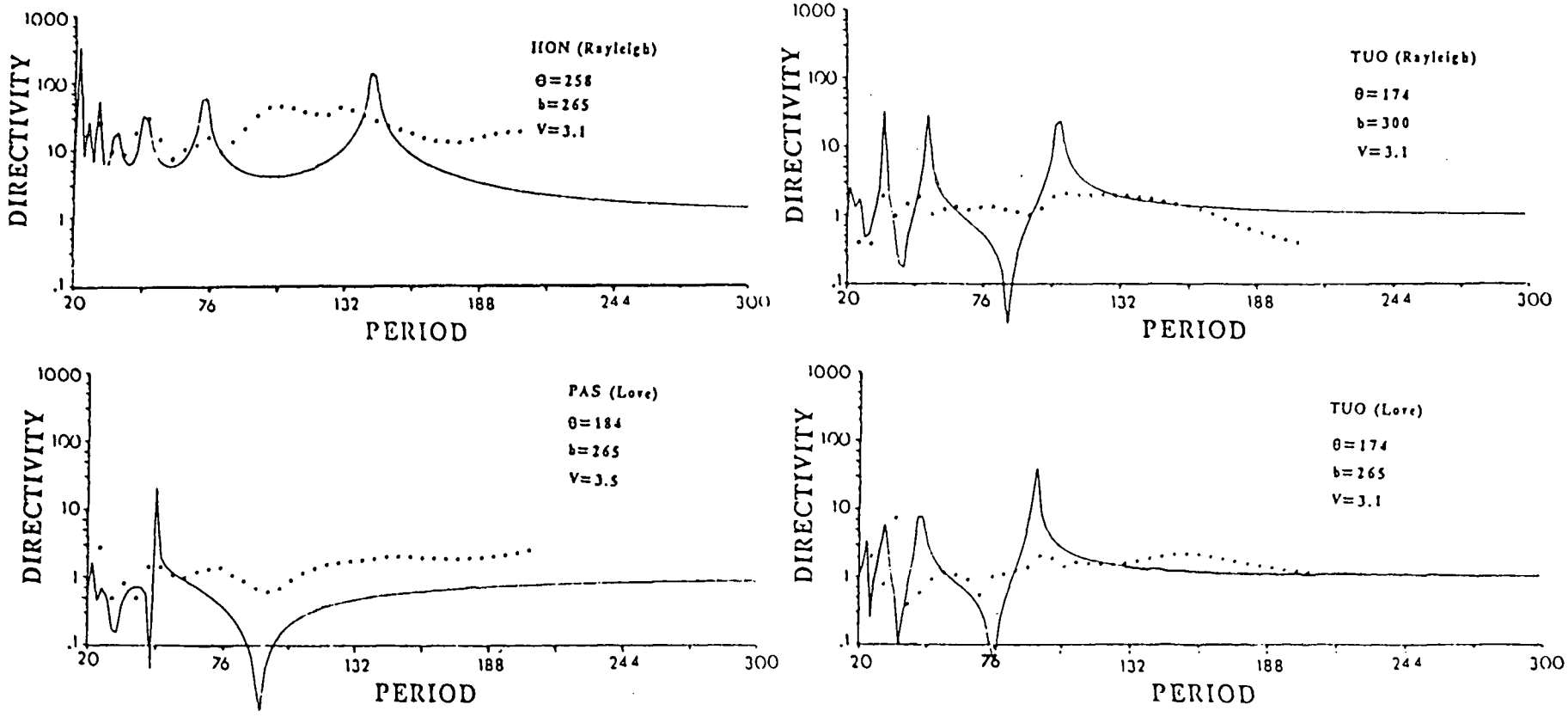

Figure 20 - DIRECTIVITY FUNCTION CURVES

The solid lines are the best fit theoretical curves. These curves correspond to a unilateral fault propagating with rupture velocity Vr=3.5 km/sec and fault length b=265 km. The circles are the data points.

is the size of the extremes. The theoretical extremes are much larger than the observed extremes which appear to be significantly smoothed.

Modification of the theoretical model was tried to better fit the data. Ben-Menahem and Toksoz (1962) have given the relationships to calculate the directivity for a decaying source of variable strength given by $L=L_0\exp(-2\xi/b_0)$, with $0\leq\xi\leq b$, and for bilateral faulting. A variable strength source seems physically reasonable, and the theoretical curves generated with a decay constant $\xi/b_0=\beta=0.75$ fit the data significantly better. The effect of the decaying source was to flatten all the extremes (see Figure 21).

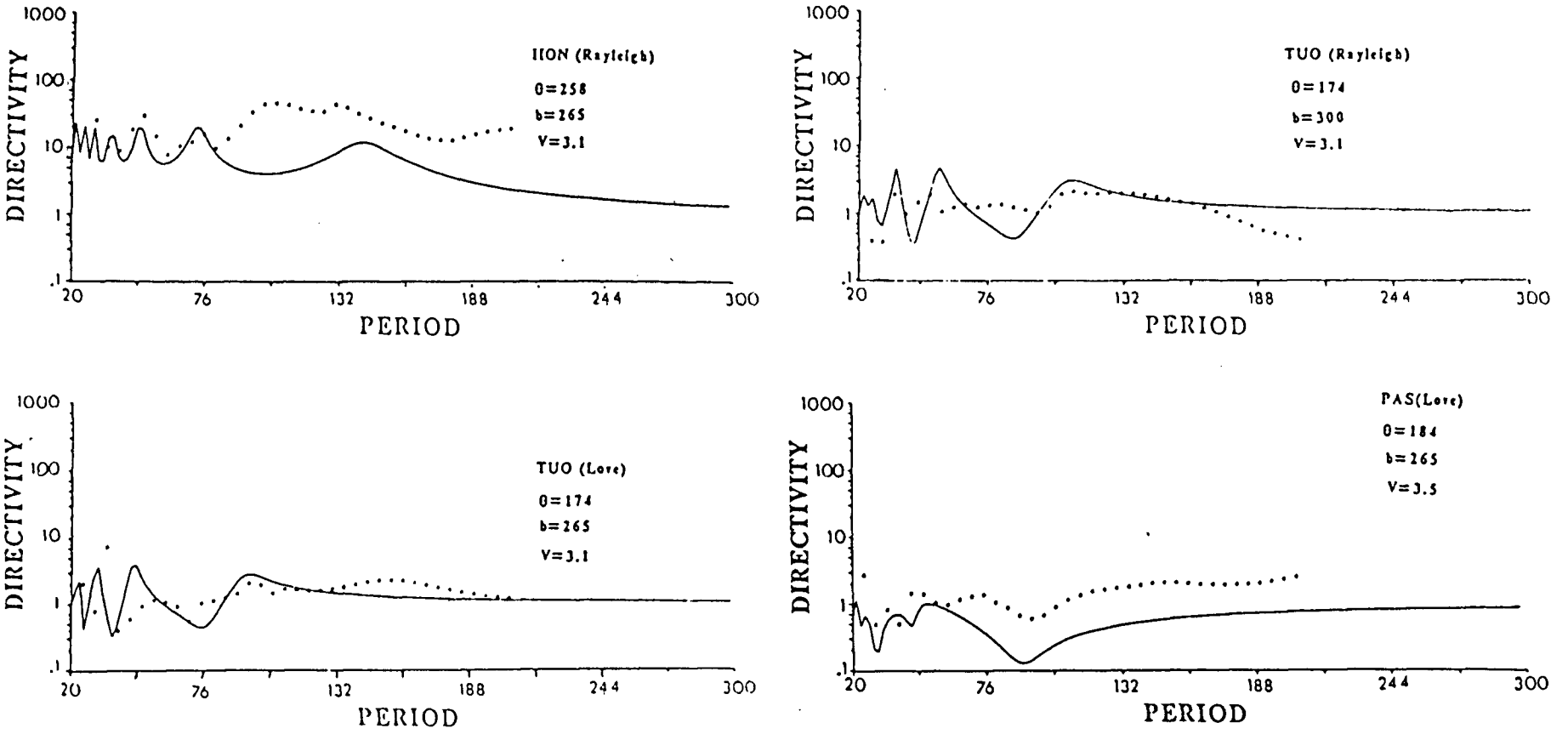

Figure 21 - DECAYING SOURCE DIRECTIVITY FUNCTION CURVES

The solid lines are theoretical curves using an exponentially decaying source function with a decay constant β=0.75, rupture velocity Vr=3.5 km/sec, and fault length b=265 km.

An attempt was made to bring the 490 km aftershock zone into agreement with the directivity function fault length by using Ben-Menahem and Toksoz's (1962) directivity relationships for bilateral faulting. The effect on the directivity function of bilateral rupture was to smooth and displace the long period extremes and damp out or eliminate the shorter period extremes (see Figure 22). No suitable bilateral rupture could be found to fit the data.

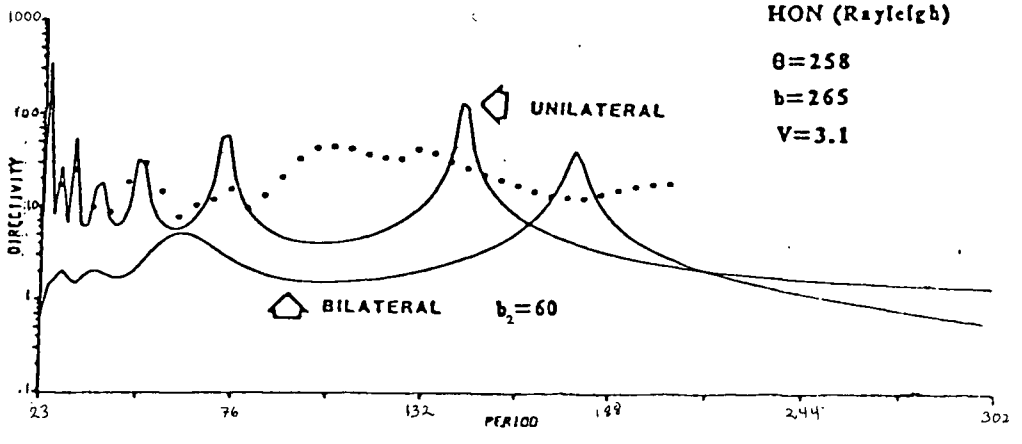

Figure 22 - THE EFFECT OF BILATERAL RUPTURE ON THE DIRECTIVITY FUNCTION

The effect of bilateral rupture on the directivity function is to smooth and slightly displace the long-period extremes, and eliminate the short period extremes.

Since the directivity was obtained from more than one station, an alternate approach to finding the rupture parameters using the least squares technique described in Section 2.2 could be applied. Using this least squares method a rupture length of

170 km and a rupture velocity 1.9 km/s was found . These values gave a good fit of the maximum period extreme, but introduced new extremes which did not exist in the data. When plotted (see Figure 23) it was found that the parameter values were being determined primarily by the values of HON and were not reliable values for the ensemble.

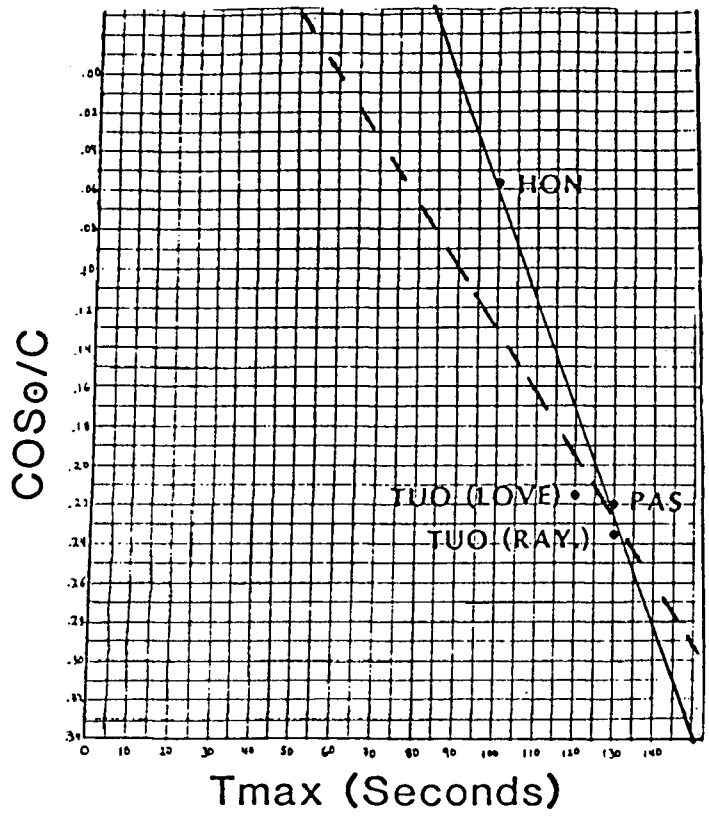

Figure 23 - LEAST SQUARES SOLUTION TO THE DATA

The solid line is the least squares line. The dashed line corresponds to the best fit solution shown in Figure 20.

For the directivity function the azimuthal angle between the fault and the seismic station, θ, is measured clockwise from the direction of rupture propagation. This means that even though the strike of the fault plane is known for a given earthquake there are two possible θ's for a given station depending upon which direction the rupture progressed. The theoretical curves should match the data for only one of the two θ's. By noting which of the two possible θ's fits the data, the direction of rupture propagation is determined. In order to fit the data for the August 22 M=8.1 earthquake, a rupture direction to the northwest had to be used. This is in agreement with Ben-Menahem's (1967) results.

4.2 DIFFERENTIAL PHASES

The differential phase at a given period between opposite traveling wave pairs was obtained at a variety of periods for each station (see Table III). The fault lengths obtained from the differential phase method show considerable scatter within a given station for all the stations except PAS. This scatter is not suprising in view of the ragged appearance of the dispersion curves. Because of the relative coherence of the PAS results these results were selected as the most reliable.

TUO (LOVE)

PERIOD	DIFFERENTIAL PHASE	LAMBDA	FAULT LENGTH
90.35	0.2556	417.92	114.24
93.00	0.1984	430.78	91.41
99.10	0.8330	460.54	410.33
102.40	0.5796	476.88	295.63
105.93	0.2751	494.57	145.55
113.78	0.2122	534.11	121.20
118.15	0.2383	555.65	141.66
122.88	0.2128	579.05	131.79
128.00	0.1781	604.48	115.15
139.64	0.2785	663.76	197.74
146.29	0.3016	698.08	225.18
153.60	0.2693	736.18	212.08
161.68	0.2940	778.64	244.83
170.67	0.3815	826.42	337.24
192.00	0.5898	941.76	594.09

AVERAGE FAULT LENGTH= 225.21

PAS (LOVE)

PERIOD	DIFFERENTIAL PHASE	LAMBDA	FAULT LENGTH
90.35	0.7330	417.92	346.59
96.00	0.4583	445.40	230.96
99.10	0.4107	460.54	214.01
102.40	0.6174	476.88	333.14
105.93	0.6072	494.57	339.78
109.71	0.4801	513.60	279.00
113.78	0.5482	534.11	331.28
118.15	0.2207	555.65	138.75
122.88	0.1553	579.05	101.77
128.00	0.2765	604.48	189.11
133.57	0.7235	632.69	517.92
139.64	0.2514	663.76	188.82
170.67	0.1205	826.42	112.65
192.00	0.2193	941.76	233.67

AVERAGE FAULT LENGTH= 254.10

TUO (RAYLEIGH)

PERIOD	DIFFERENTIAL PHASE	LAMBDA	FAULT LENGTH
90.35	0.8717	368.63	692.80
93.09	1.0122	380.43	830.24
96.00	0.3641	393.28	308.70
99.10	0.7663	407.03	672.45
102.40	0.7548	421.75	686.33
105.93	0.7158	437.56	675.30
109.71	0.6666	454.60	653.31
113.78	1.1638	473.05	1186.98
118.15	0.3775	492.99	401.20
122.88	0.7416	514.71	822.94
133.57	0.9765	565.04	1189.54
139.64	0.5719	594.11	732.51
153.60	1.2902	660.40	1837.02
170.67	0.8729	736.58	1366.29
192.00	0.2948	862.73	548.33

AVERAGE FAULT LENGTH= 841.59

HON (RAYLEIGH)

PERIOD	DIFFERENTIAL PHASE	LAMBDA	FAULT LENGTH
90.35	0.9164	368.63	551.49
93.09	1.5652	380.43	972.03
96.00	0.9997	393.28	641.85
99.10	1.2905	407.03	857.53
105.93	0.5259	437.56	375.66
113.78	0.8785	473.05	678.42
118.15	0.7201	492.99	579.49
122.88	0.4773	514.71	401.08
128.00	1.1336	538.62	996.74
133.57	0.9651	565.04	890.23
139.64	0.1579	594.11	153.17
161.68	0.4668	696.39	530.66
180.71	0.2665	791.19	344.24
192.00	0.6498	862.73	915.18

AVERAGE FAULT LENGTH= 634.84

Table III - DIFFERENTIAL PHASE FAULT LENGTHS

The poor consistency of the results within a given station for the differential phases is not suprising. In the literature (e.g., Kanamori, 1970) it is frequently recommended that differential phases only be applied to periods greater than 200

seconds. These recommendations, based on results derived from long period instruments of the world wide seismic network, imply that crustal scattering strongly affects the coherency of waves with periods shorter than 200 seconds. The lack of coherence is likely to be further accentuated if one does not have the luxury of a true long period insrument but must rely on instruments with a peak response around 12 seconds. At periods $\leq$ 100 seconds crustal scattering strongly affects the coherence, while for periods longer than 100 seconds the response of the short period seismographs are so poor that the signal becomes buried in noise and, hence, is incoherent at long periods as well as short. The results from PAS show the best internal consistency and agree with Ben-Menahem (1967, 1978).

Following the suggestion of Aki(1966), a weighted average of the differential phases fault lengths from all four stations was taken. Though there was no specific formula for determining the weighting, I tried to make the weighting an individual station received correspond to the internal consistency of the results of that station. With the weighting of PAS=1.0, HON=0.5, TUC (Love)=0.25, and TUC (Rayleigh)=0.25 an average rupture length, from the weighted average of the differential phases, of 358 km was derived.

4.3 ERROR ANALYSIS

The attempts in this thesis to extract information from surface waves perhaps demonstrate one thing more than any other: quality seismographs with appropriate response curves are essential for obtaining detailed information about earthquake source parameters. Old low power seismographs introduce too many uncertainties into the seismogram and unduly influence the subsequent analysis.

If the fundamental mode arrival is correctly identified with its amplitude and phase unaffected by seismic noise and crustal scattering, then the error in the calculated differential phase would come from three possible sources:

1) error in the instrument phase response correction
2) improper T_o
3) wrong phase velocities used.

The effect on the results of (1) would depend on how far off the true instrument response was from the correction. An estimate of 20% instrument response uncertainty seems reasonable for these older instruments. This implies a possible 20% error in radians of the differential phase results. An error Δt in T_o would lead to a

$$\delta\phi=\omega\Delta t=2\pi f\Delta t \text{ error in radians.}$$

An error in the phase velocity, c, would lead to,

$$\delta\phi=\delta(\omega r/c)=\omega r\ \partial c/c^2 \text{ error in radians}$$

where

∂c = error in c

c = phase velocity
r = length of path over which the phase velocity is in error.

The fact is, however, that the data are greatly influenced by crustal scattering and seismograph noise, the effects of which are difficult to assess, and which as a result make an overall error estimate impractical.

Estimates of the directivity uncertainty are subject to the same difficulties as above. For both the differential phase fault length and the directivity function, the size of the scatter of the results among the three stations is probably the best indication of the uncertainty of the results.

4.4 SEISMIC MOMENT AND STRESS DROP

The seismic moment for the 1949 Queen Charlotte earthquake was calculated using the results of Ben-Menahem (1978). Ben-Menahem did not explicitly determine the seismic moment for this earthquake. He derived the directivity and differential phases, and using these results obtained what he called the equalized potency. This potency is related to the seismic moment by the rigidity μ. I chose to use his data over mine as he was using a true long period instrument which allowed him to measure the surface wave amplitude at a period of 200 seconds where the effect of crustal inhomogeneities is minimized. I could not get a good measure of the surface wave amplitude at this long period since the response curves for all of my instruments meant that the amplitude of the seismic signal was at the noise level (see Figure 24 and Appendix D to compare the response of the PAS

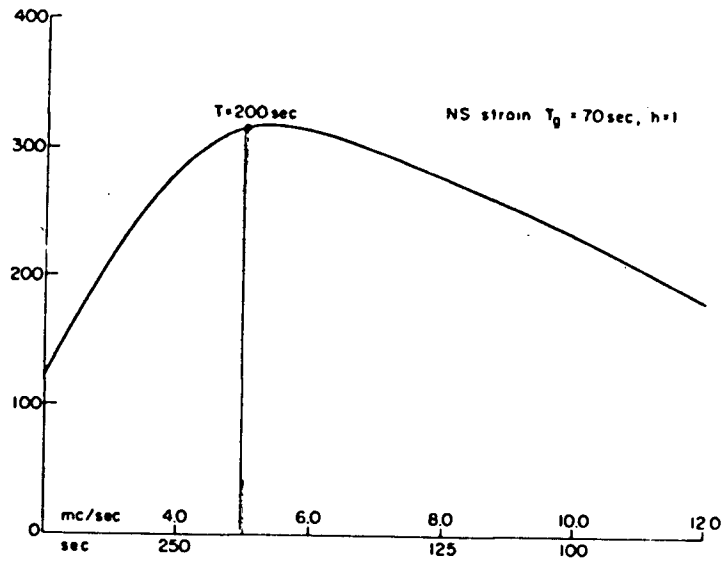

Figure 24 - RESPONSE CURVE FOR THE PAS STRAIN METER

(Adapted from Ben-Menahem, 1978)

strain meter with the response of the instruments used in this thesis).

The seismic moment is derived from spectral amplitudes by correcting for the finiteness of the rupture process (derived from the directivity results), radiation pattern, and the Love or Rayleigh crustal transfer function. All of this was done by Ben-Menahem in obtaining the equalized potency. Using his results and $\mu=3.2\times10^{11}$ dyne/cm^2, a seismic moment $Mo=1.15 \times 10^{28}$ dyne cm was found. This compares well to the Mo found using Geller and Kanamori's (1977) relation,

$$Mo=1.23\times10^{22} \times S^{1.5}$$

where S is the fault surface area in km^2.

With S=(495)x(20) an Mo of 1.2×10^{28} is obtained.

Using Gutenberg and Richter's (Richter, 1958) formula for seismic energy E ,

$$\text{LogE} = 11.8 + 1.5\text{Ms} \qquad \text{For Ms} \geq 6.5$$

For Ms=8.1 $E = 8.9 \times 10^{23}$ ergs,

and Aki's (1966) relation for apparent stress drop σ ,

$$\sigma_a = \eta\bar{\sigma} = \mu E / M_0$$

where
μ=rigidity
E_s=seismic energy
η=efficiency coefficient of strain energy released into seismic energy.
$\bar{\sigma}$=average stress,

the apparent stress drop was calculated to be σ_a=25 bars. The average displacement along the fault can be derived using the the standard expression for the seismic moment (Kanamori and Anderson, 1975).

$$M_0 = \mu LW\bar{D}$$

L=fault length
W=fault width
$\bar{D}$=average displacement along the fault

Solving this equation for the average displacement using a fault width of 21 km one obtains,

D=6.5 m for L=265 km

D=3.5 m for L=495 km

for an overall average displacement of $\bar{D}$=5.0 m.

If we follow Ben-Menahem (1978) and break the seismic moment into the sum of the moments generated by the displacement along two different parts of the fault, namely the part for which the displacement is largest (the directivity fault length) and the part for which the displacement is the least (that part of the rupture which is beyond the directivity length; see the discussion section of the Summary and Discussion chapter for an explanation of this), then we can write the relation for the seismic moment as,

$$M_0=\mu W(L_1\bar{D}_1+L_2\bar{D}_2).$$

If we assume $\bar{D}_1$=4.96 m, L_1=265 km, and L_2=(495km-265km)=230 km, then $\bar{D}_2$=1.7 m. Therefore, the average displacement along the whole fault is 4.96 m, but along the ends of the fault only 1.7 m.

The stress drop was calculated using the relationship between stress drop and the seismic moment for a strike-slip fault (Kanamori and Anderson, 1975),

$$M_0=(\pi/2)W^2L\Delta\sigma.$$

The stress drop, $\Delta\sigma$, was found to be $\Delta\sigma$=34 bars. The strain energy was also calculated using Kamamori and Anderson's (1975) relationship between the strain energy, ΔW, and the apparent and average stress,

$$\Delta W=(\pi W^2L/2\mu)\Delta\sigma\bar{\sigma}.$$

The strain energy was found to be $\Delta W=9.5 \times 10^{23}$ ergs. This allowed the efficiency constant η to be determined:.

$$\eta=E_s/\Delta W=0.93 .$$

The average stress was calculated:

$$\bar{\sigma}=\sigma_a/\eta=26.9 \text{ bars} .$$

And finally the frictional stress, σ_f was calculated,

$$\sigma_f=\bar{\sigma}-\sigma_a=1.9 \text{ bars}$$ (Kamamori and Anderson, 1975).

Ben-Menahem (1978) derives a fault depth of 40 km for this earthquake, in stark contrast to the results of Horn et. al. (1984), and Hyndman and Ellis (1981) who suggest a crustal depth in the area of only 16-21 km. Ben-Menahem's value for the depth was derived by assuming the fault length to be 265 km with an average displacement along the fault arbitrarily chosen to be 3.5 m. If an average displacement of 4.96 m and a fault length of 495 km is used, his calculations will yield a depth consistent with the estimated crustal depth.

V. RESULTS FOR THE EARTHQUAKES OF AUGUST 23 AND OCTOBER 31

As mentioned earlier, out of more than 30 stations originally requested, only five could be used in determining the surface wave radiation pattern for the August 23 (M=6.4) earthquake and only eight for the October 31 (M=6.2) earthquake. The general problem was the lack of true long period instruments coupled with an uncertainty of both instrument parameters and calibration accuracy. In general, the instrument magnification was estimated as known only to within twenty percent.

The digitized seismograms for the August 23 and October 31 earthquakes are shown in Figures 25-29. The group velocity dispersion curves are shown in Figures 30-36. These dispersion curves give an indication of the quality of the data. For instance, the fundamental mode arrival was clearly discernible out to 60 seconds for the August 23 DBN data (Figures 30, 31). In contrast, the data from August 23 OTT (Figure 31) does not display any clear mode arrival. The difference between DBN and OTT is partly explained by noting that the waves arriving at DBN have had twice as long to disperse and separate as those arriving at OTT. Therefore, the dispersion curve used to identify mode arrival is more clearly seen by this filtering technique at DBN than at OTT. The rapid and steady rise for OTT in amplitude for almost all group velocities starting around 55 seconds indicates that beyond 55 seconds instrument response has dropped off so much that in correcting for instrument response only noise is being amplified.

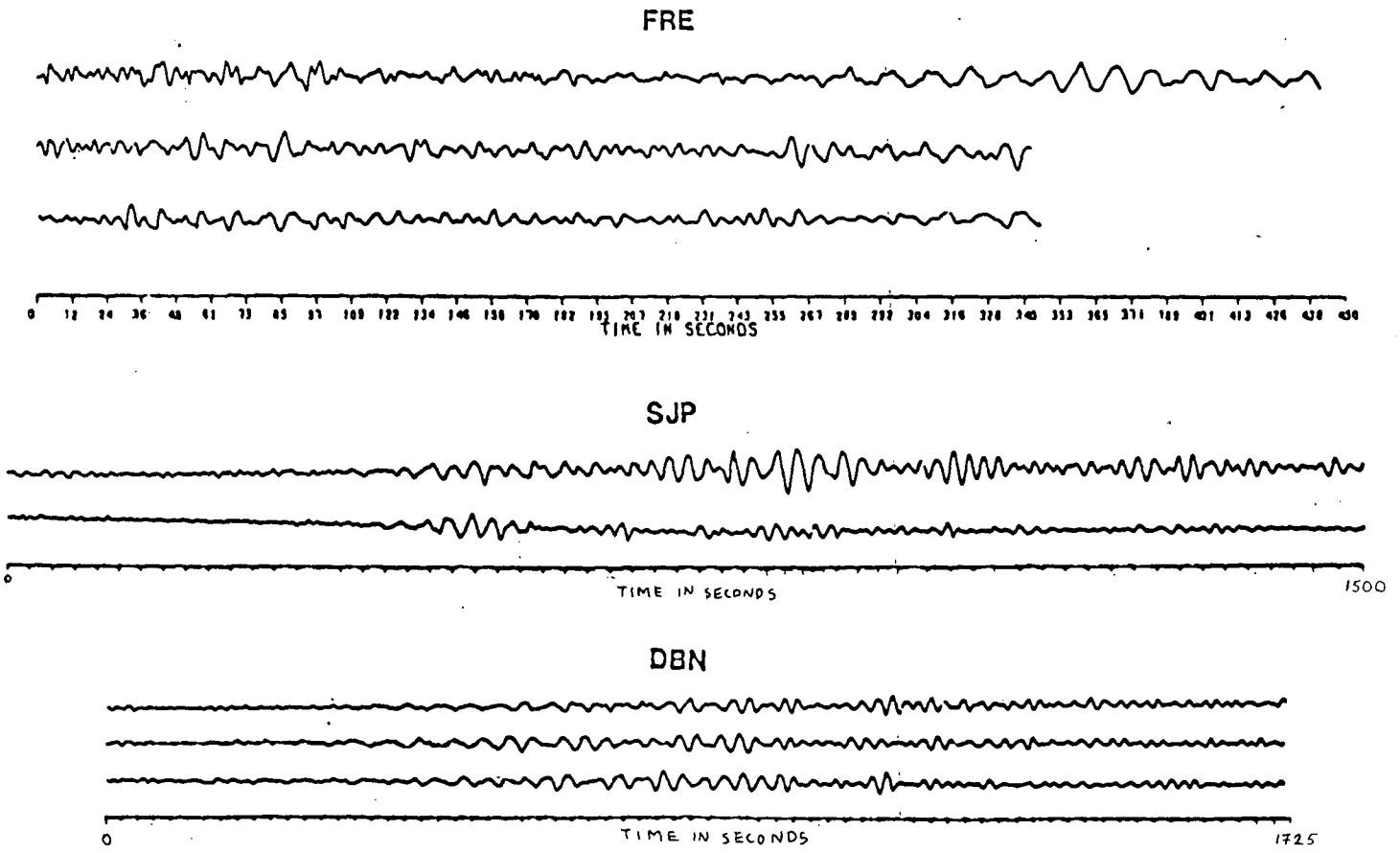

Figure 25 - DIGITIZED SEISMOGRAMS FOR THE AUGUST 23 EARTHQUAKE (M=6.4)

The upper trace for FRE and DBN was recorded on the vertical seismograph, the middle trace on the north-south seismograph, and the lower trace on the east-west seismograph. The SJP set of seismograms has no vertical, and, hence, the upper trace corresponds to the north-south seismogram, and the lower trace to the east-west seismogram.

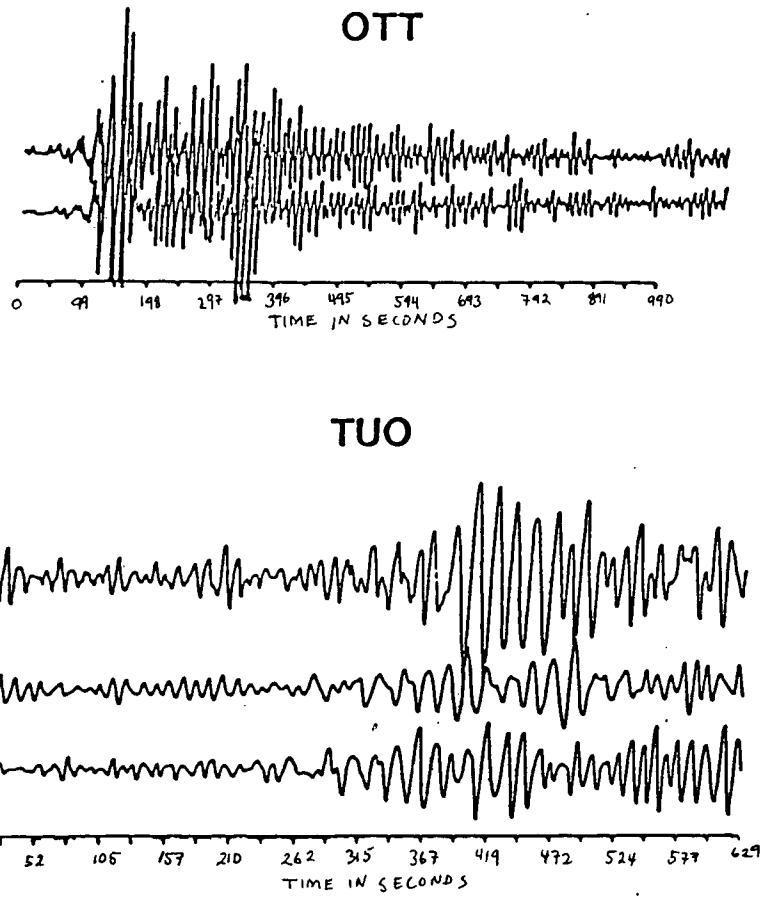

Figure 26 - DIGITIZED SEISMOGRAMS FOR THE AUGUST 23 EARTHQUAKE (M=6.4)

The upper trace for OTT corresponds to the north-south seismogram, and the lower trace the east-west seismogram. The order of the seismograms for TUO is the same as OTT except that the top seismogram is a vertical seismogram.

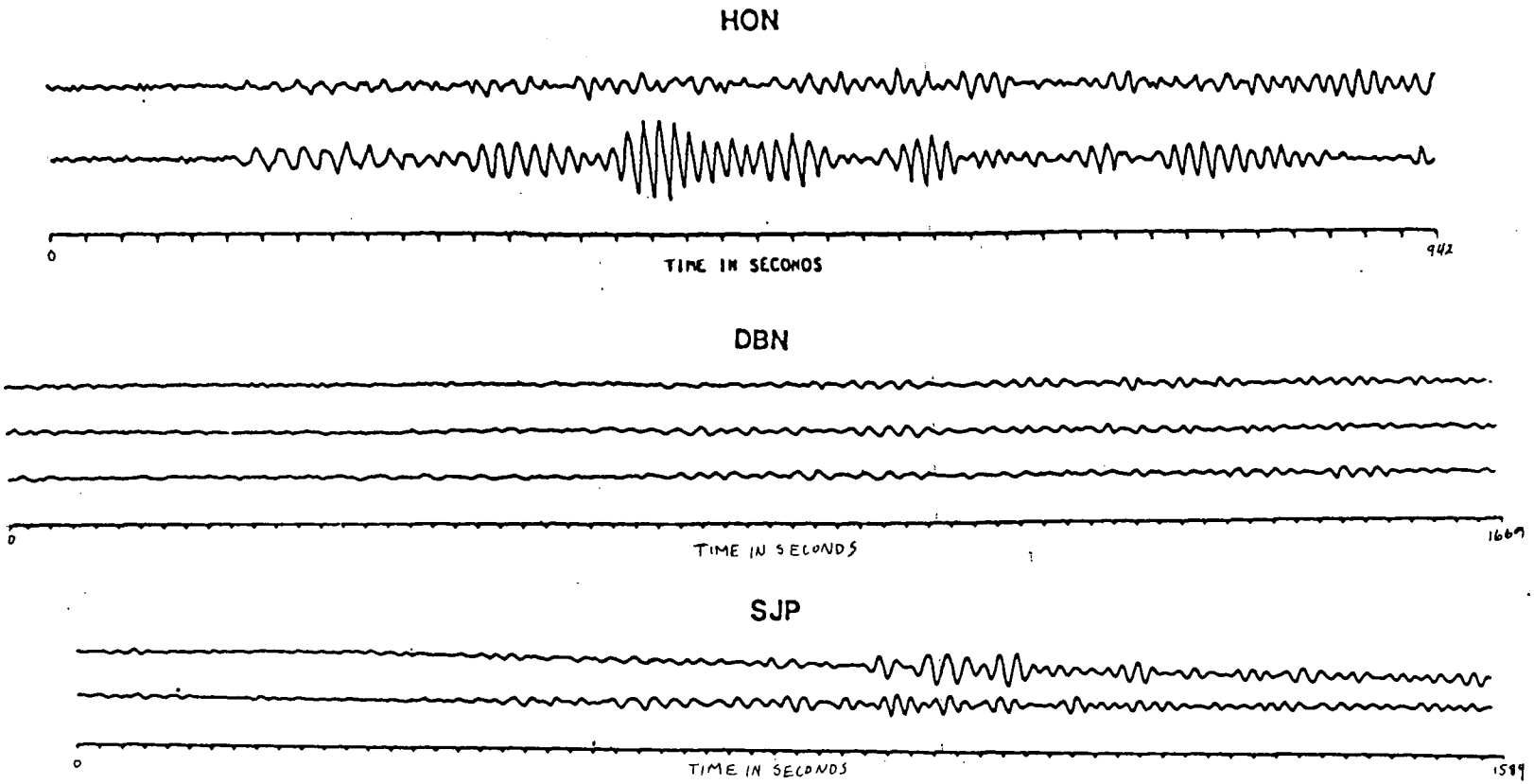

Figure 27 - DIGITIZED SEISMOGRAMS FOR THE OCTOBER 31 EARTHQUAKE (M=6.2)

The upper trace for DBN is the vertical seismogram, the middle trace the north-south seismogram, and the lower trace the east-west seismogram. The ordering of the traces for HON and SJP is the same as for DBN except that there is no vertical seismogram.

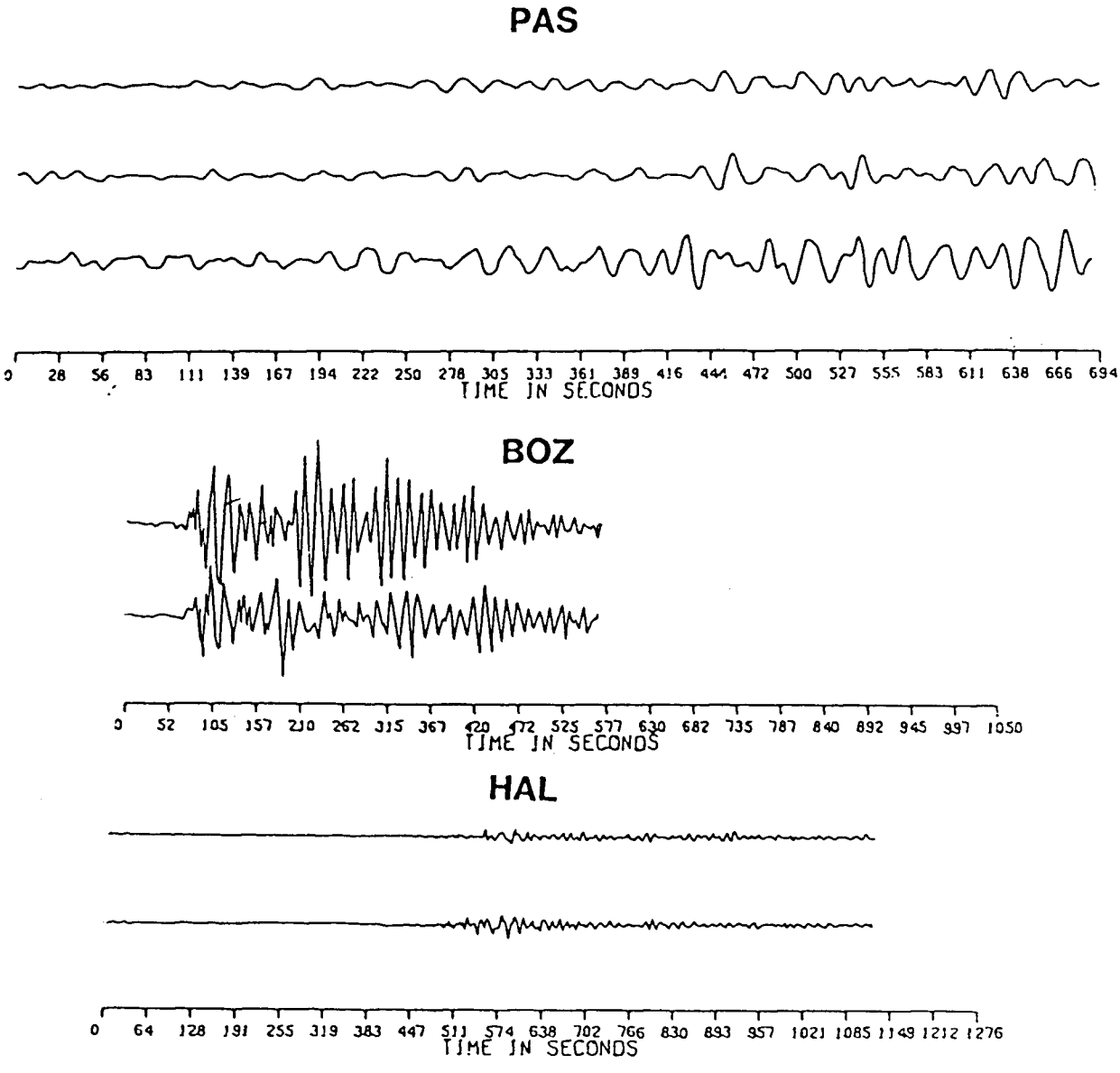

Figure 28 - DIGITIZED SEISMOGRAMS FOR THE OCTOBER 31 EARTHQUAKE (M=6.2)

The upper trace for PAS is the vertical seismogram, the middle trace the north-south seismogram, and the lower trace the east-west seismogram. The ordering of the traces for BOZ and HAL is the same as for PAS except that there is no vertical seismogram.

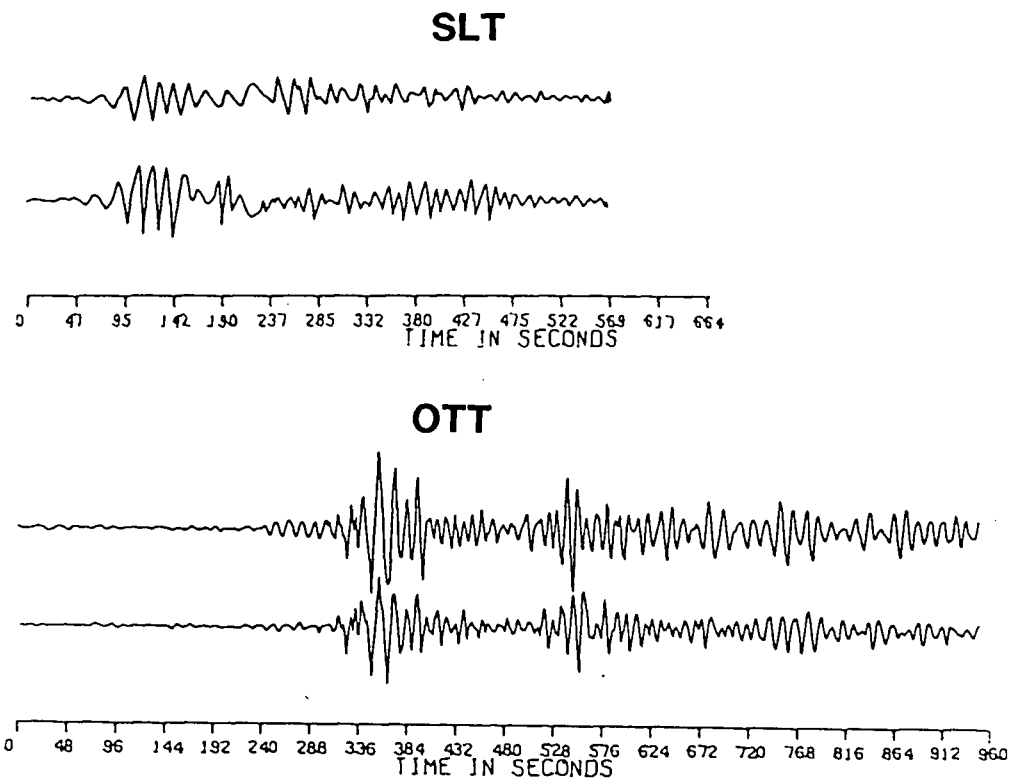

Figure 29 - DIGITIZED SEISMOGRAMS FOR THE OCTOBER 31 EARTHQUAKE (M=6.2)

For both SLT and OTT the upper trace is the north-south seismogram, and the lower trace is the east-west seismogram.

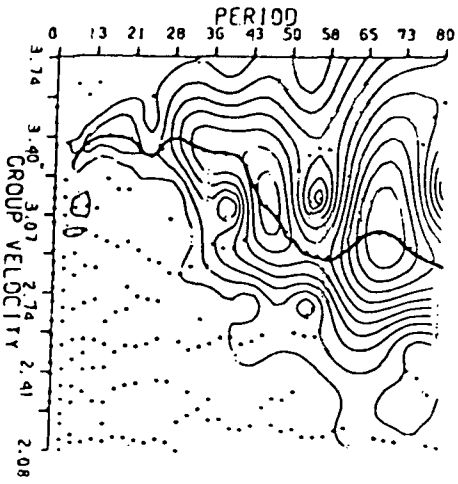

OTT UT

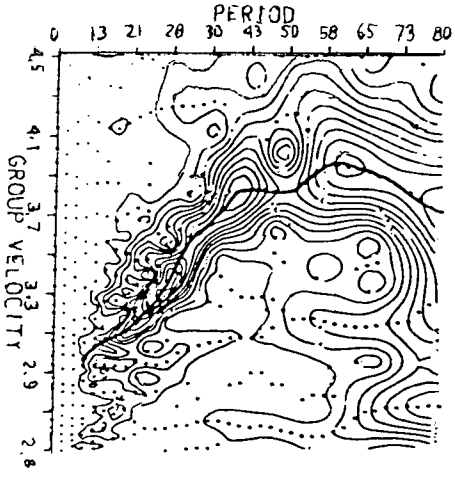

DBN UT

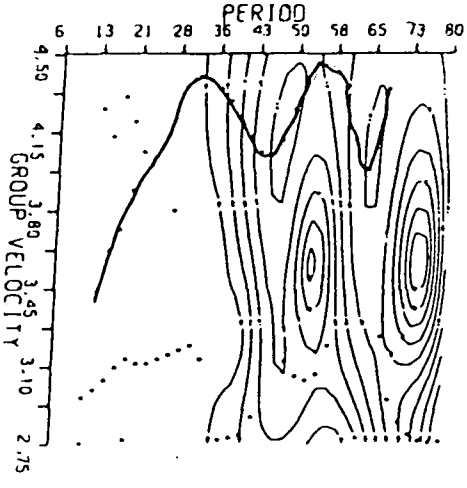

FRE UT

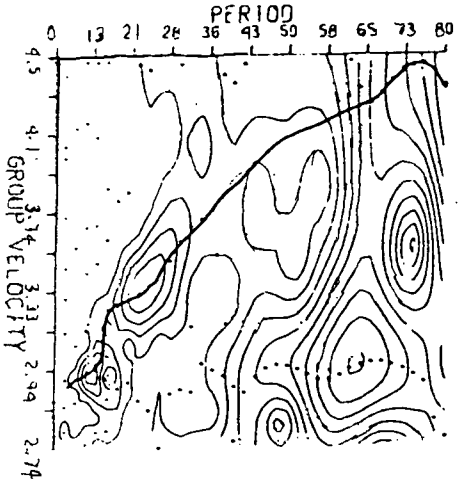

TUC UT

Figure 30 - GROUP VELOCITY CURVES FOR THE AUGUST 23 LOVE WAVE DATA

The dots indicate the positions of local maximums of the spectral amplitude. The solid line indicates the energy arrivals selected as corresponding to the fundamental mode. UT means only the tangential component of the seismograms is analyzed.

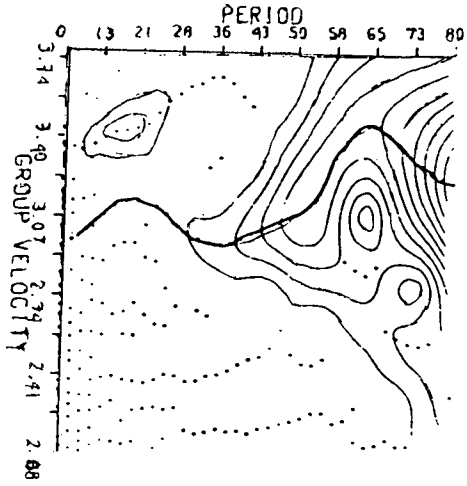

OTT UR

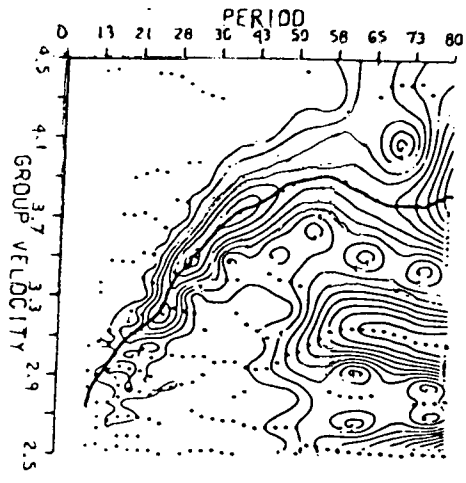

DBN Z

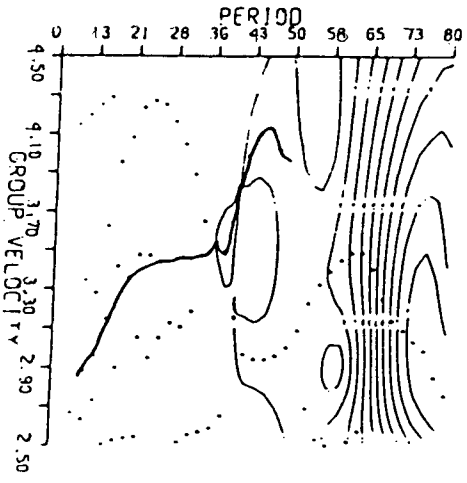

FRE Z

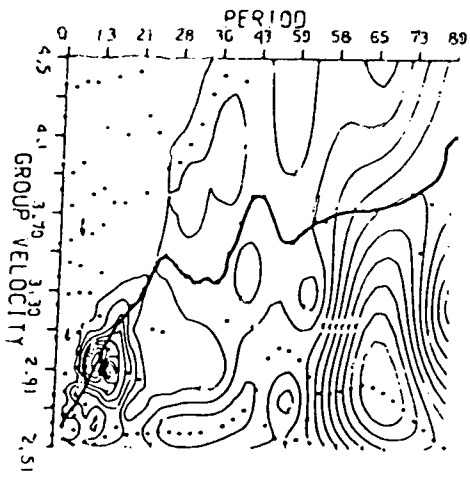

TUC Z

Figure 31 - GROUP VELOCITY CURVES FOR THE AUGUST 23 RAYLEIGH WAVE DATA

The dots indicate the positions of local maximums of the spectral amplitude. The solid line indicates the energy arrivals selected as corresponding to the fundamental mode. UR means only the radial (UR) component of the seismograms is analyzed. Z means only vertical data is be analyzed.

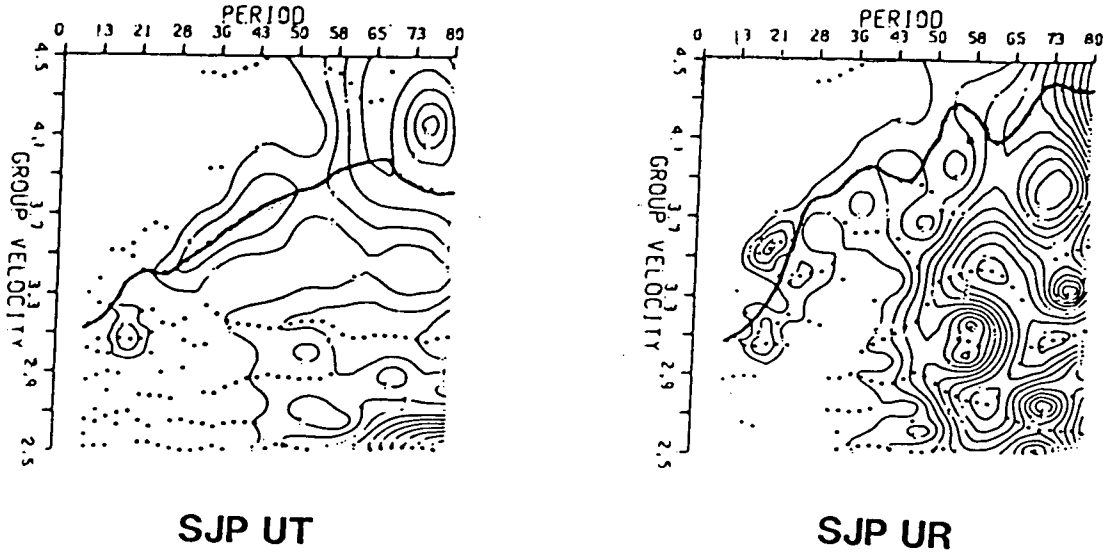

Figure 32 - GROUP VELOCITY CURVES FOR THE AUGUST 23 SJP DATA

The dots indicate the positions of local maximums of the spectral amplitude. The solid line indicates the energy arrivals selected as corresponding to the fundamental mode.

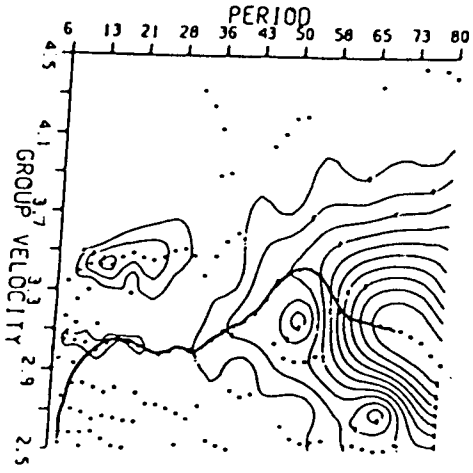

OTT UR

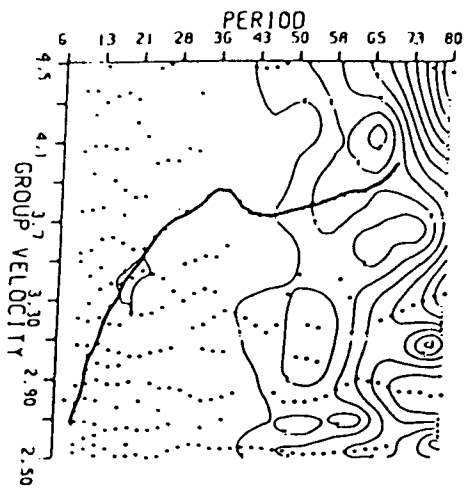

SJP UR

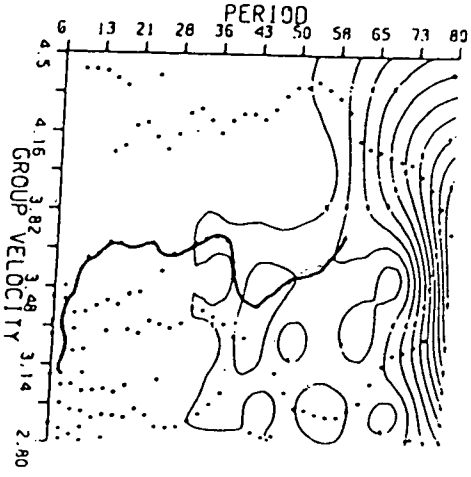

HAL UR

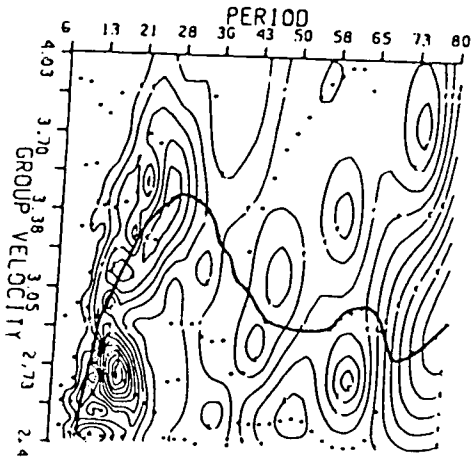

PAS Z

Figure 33 - GROUP VELOCITY CURVES FOR THE OCTOBER 31 LOVE WAVE DATA

The dots indicate the positions of local maximums of the spectral amplitude. The solid line indicates the energy arrivals selected as corresponding to the fundamental mode.

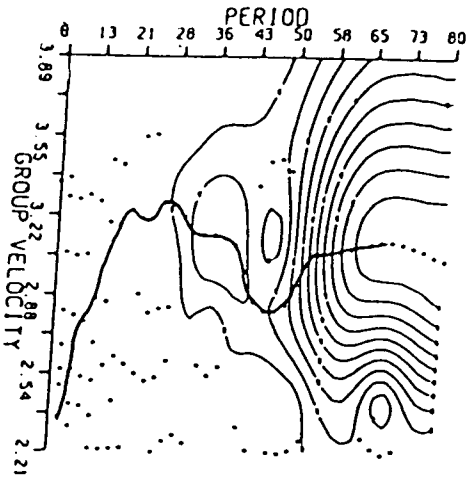

SLT UR

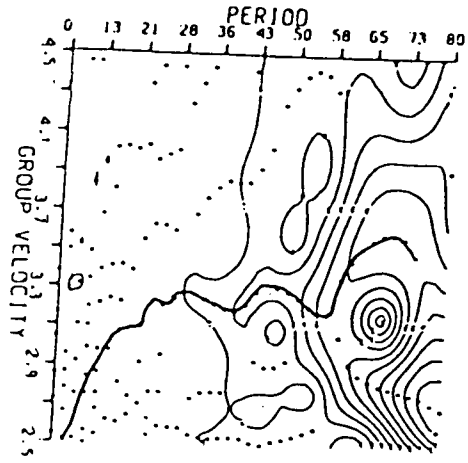

HON UR

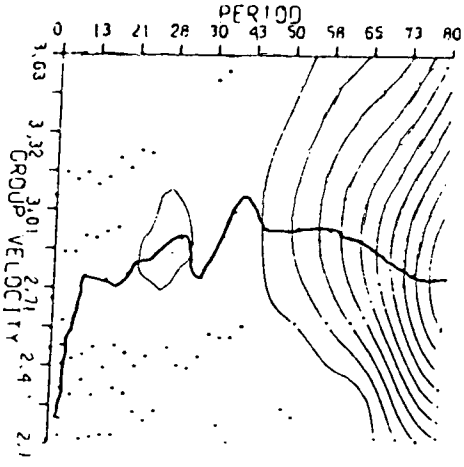

BOZ UR

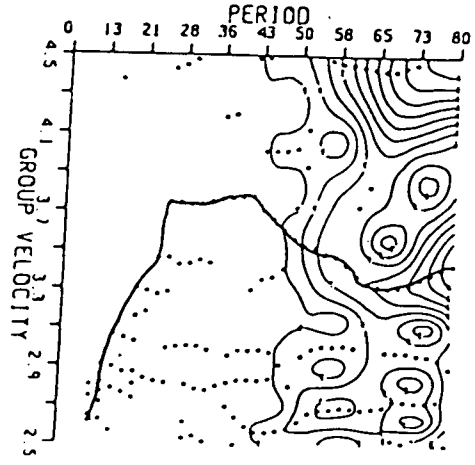

DBN Z

Figure 34 - GROUP VELOCITY CURVES FOR THE OCTOBER 31 LOVE WAVE DATA

The dots indicate the positions of local maximums of the spectral amplitude. The solid line indicates the energy arrivals selected as corresponding to the fundamental mode.

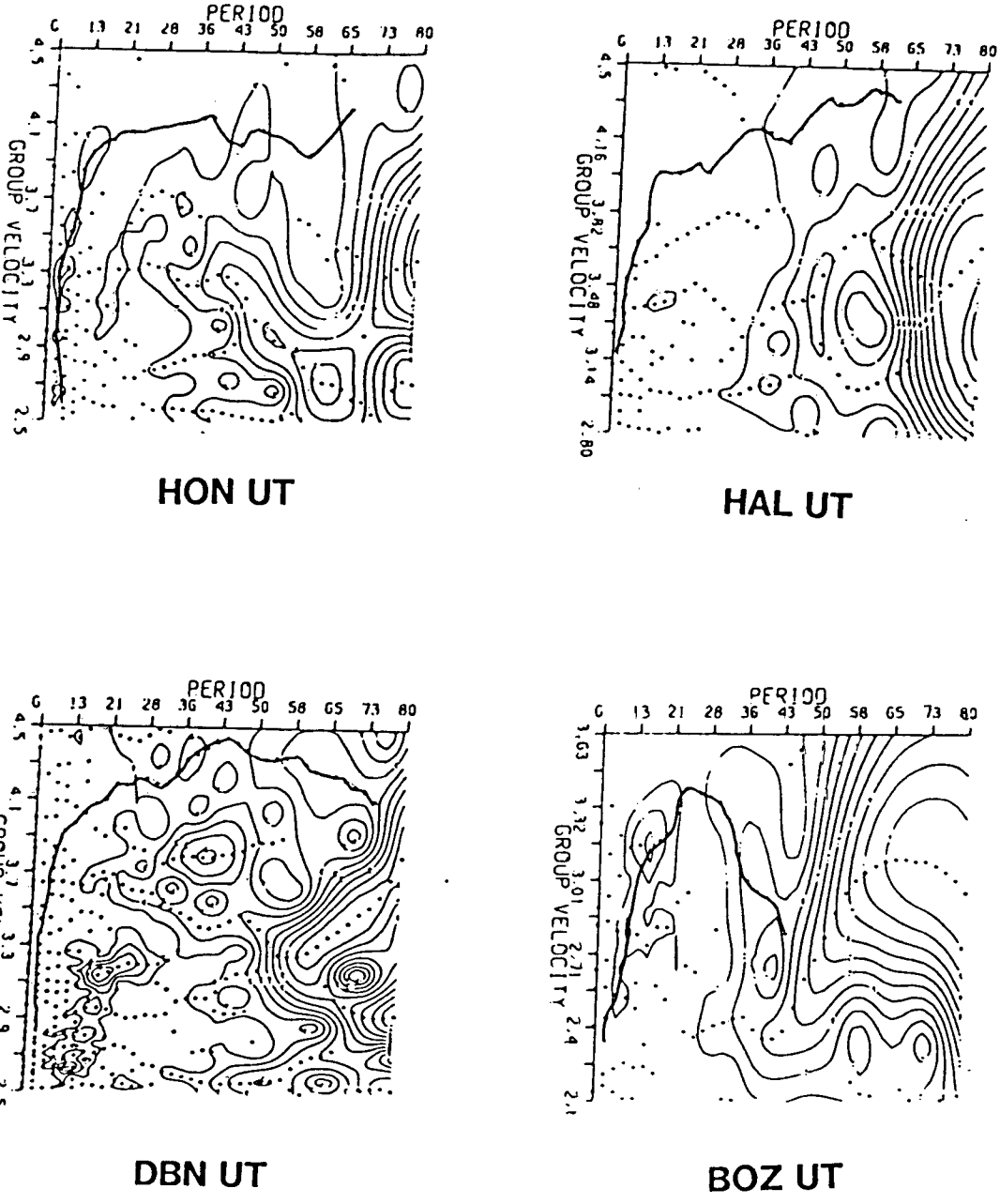

Figure 35 - GROUP VELOCITY CURVES FOR THE OCTOBER 31 RAYLEIGH WAVE DATA

The dots indicate the positions of local maximums of the spectral amplitude. The solid line indicates the energy arrivals selected as corresponding to the fundamental mode.

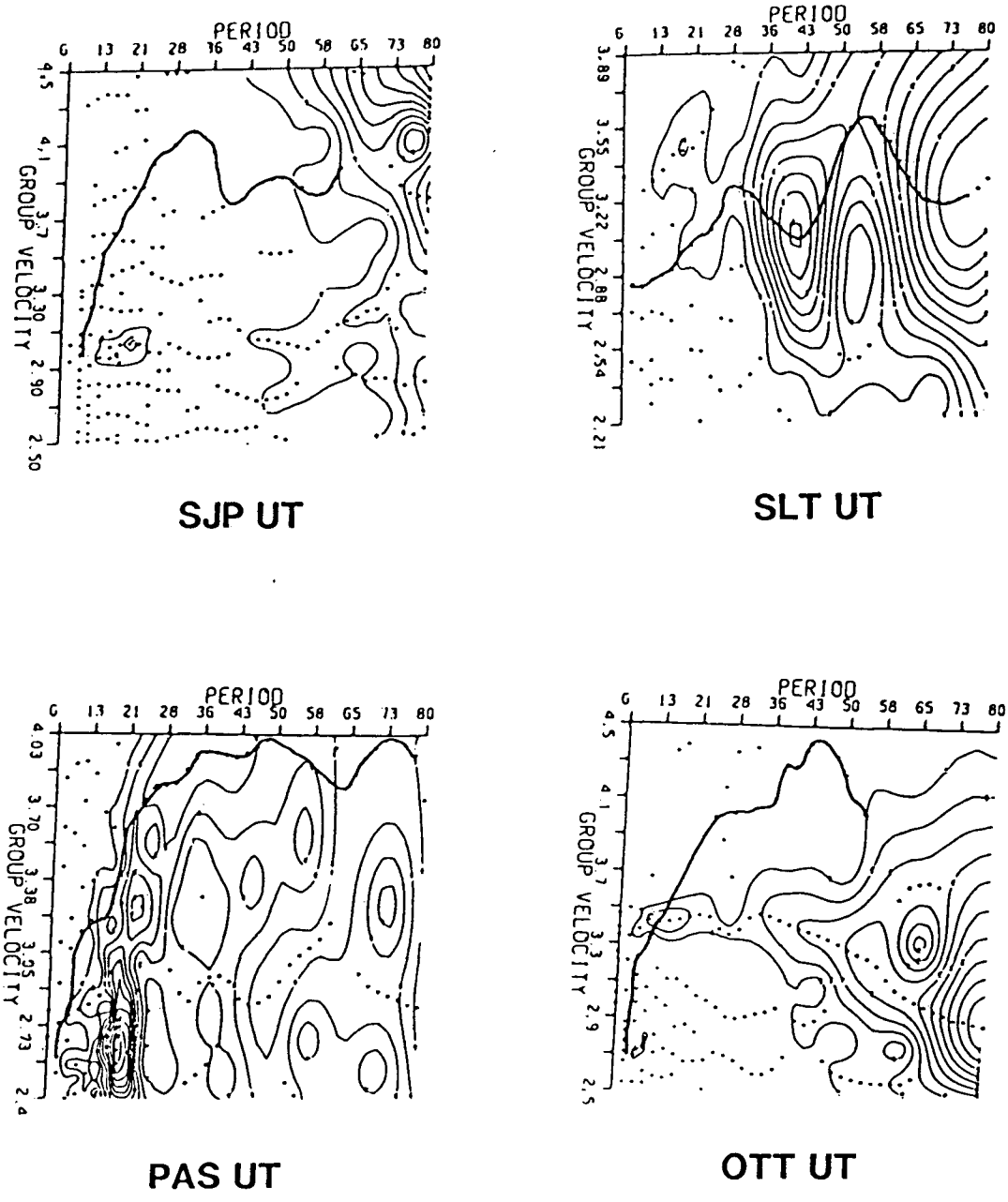

Figure 36 - GROUP VELOCITY CURVES FOR THE OCTOBER 31 RAYLEIGH WAVE DATA

The dots indicate the positions of local maximums of the spectral amplitude. The solid line indicates the energy arrivals selected as corresponding to the fundamental mode.

MECHANISM SOLUTIONS

Depending on the station, spectral amplitudes for periods from 16 seconds to 65 seconds were used. For each period, the observed azimuthal variation in amplitude was plotted. Using a six layer Earth model of North America (see Appendix C) and the Herrmann (1978) program QUESTION, the observed azimuthal amplitudes were compared to theoretical amplitudes until a 'best fit' mechanism was found. The seismic moment was calculated separately from Love waves and then from Rayleigh waves. The best fit mechanism was chosen as the mechanism for which the two separate moment estimates from Love and Rayleigh waves were in closest agreement.

Due to the small number of stations coupled with the uncertainty in the instrument magnifications the solutions obtained from this comparison process are not meaningful. The 'best fit' mechanism was not a 'good fit' mechanism for either the August 23 or the October 31 earthquake. The fit of the observed surface wave radiation pattern to the best fit model is shown for the August 23 (M=6.4) earthquake in Figures 37 and 38, and for the October 31 (M=6.2) earthquake in Figures 39 and 40. Focal sphere plots of the best fit mechanisms are shown in Figure 41. The Wickens and Hodgson (1967) first motion solution for the October 31 earthquake is also shown in Figure 41 along with the few first motions available for the August 23 earthquake.

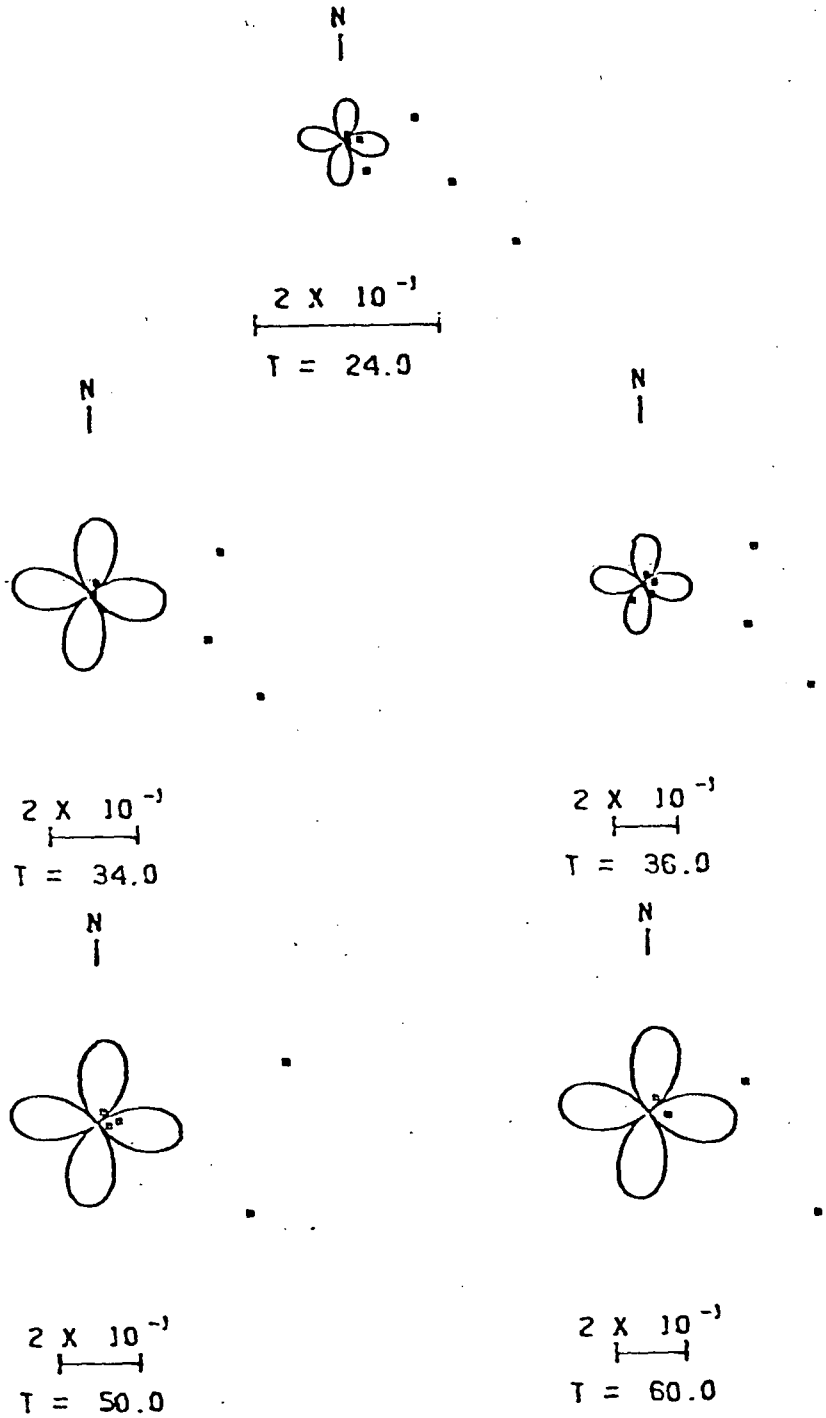

Figure 37 - THEORETICAL LOVE WAVE RADIATION PATTERN FOR THE AUGUST 23 EARTHQUAKE

The radiation patterns are scaled to fit in a square 2-3/4 inches on a side. Beneath each radiation pattern the period is written along with a scale relating the plot size to units of dyne-cm. The radiation pattern shown is of the best fit mechanism solution. The dots indicate the observed data. Each dot represents a station, with the azimuth of the dot corresponding to the station azimuth, and the distance of the dot from the center of the radiation pattern.

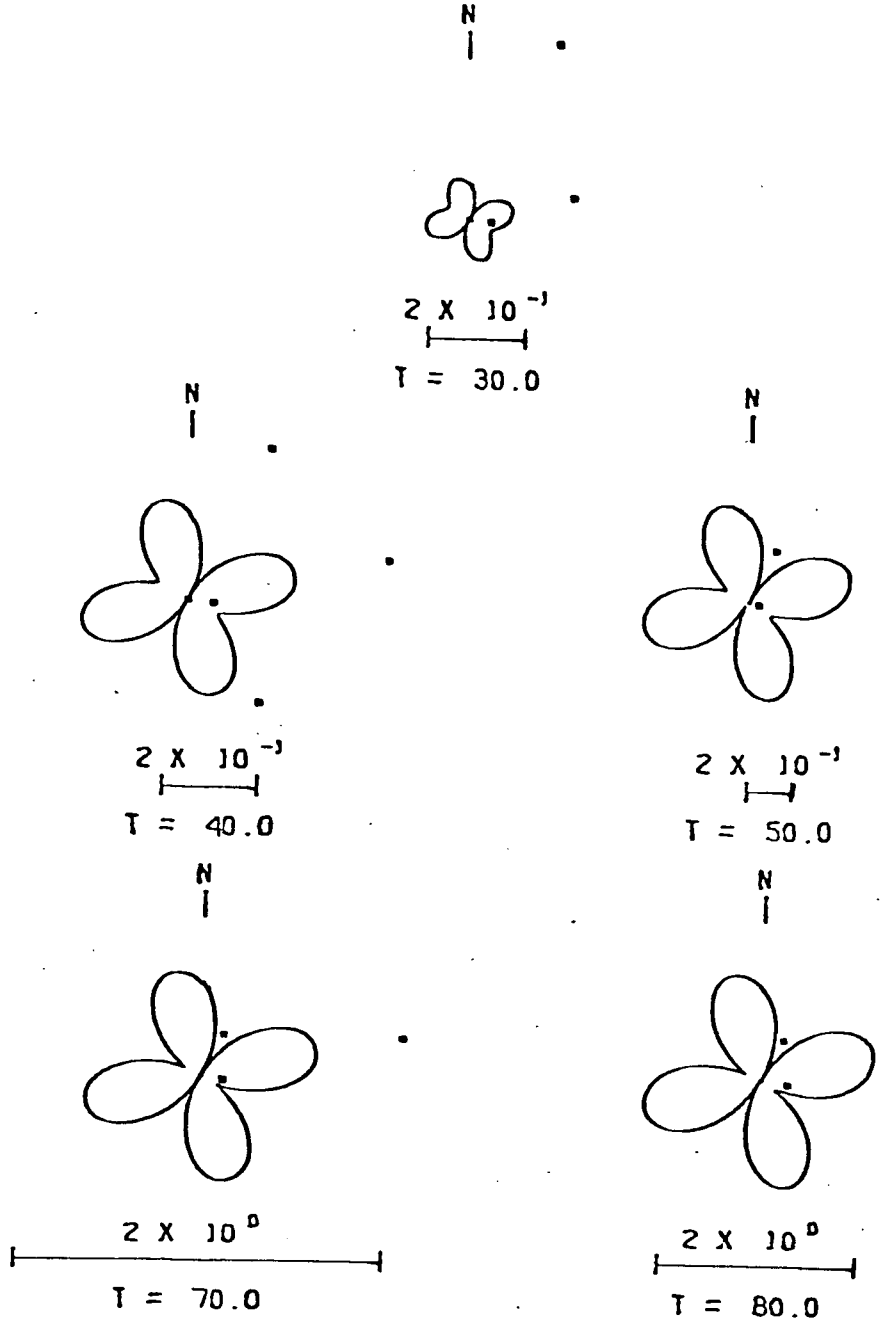

Figure 38 - THEORETICAL RAYLEIGH WAVE RADIATION PATTERN FOR THE AUGUST 23 EARTHQUAKE

The radiation patterns are scaled to fit in a square 2-3/4 inches on a side. Beneath each radiation pattern the period is written along with a scale relating the plot size to units of dyne-cm. The radiation pattern shown is of the best fit mechanism solution. The dots indicate the observed data. Each dot represents a station, with the azimuth of the dot corresponding to the station azimuth, and the distance of the dot from the center of the radiation pattern.

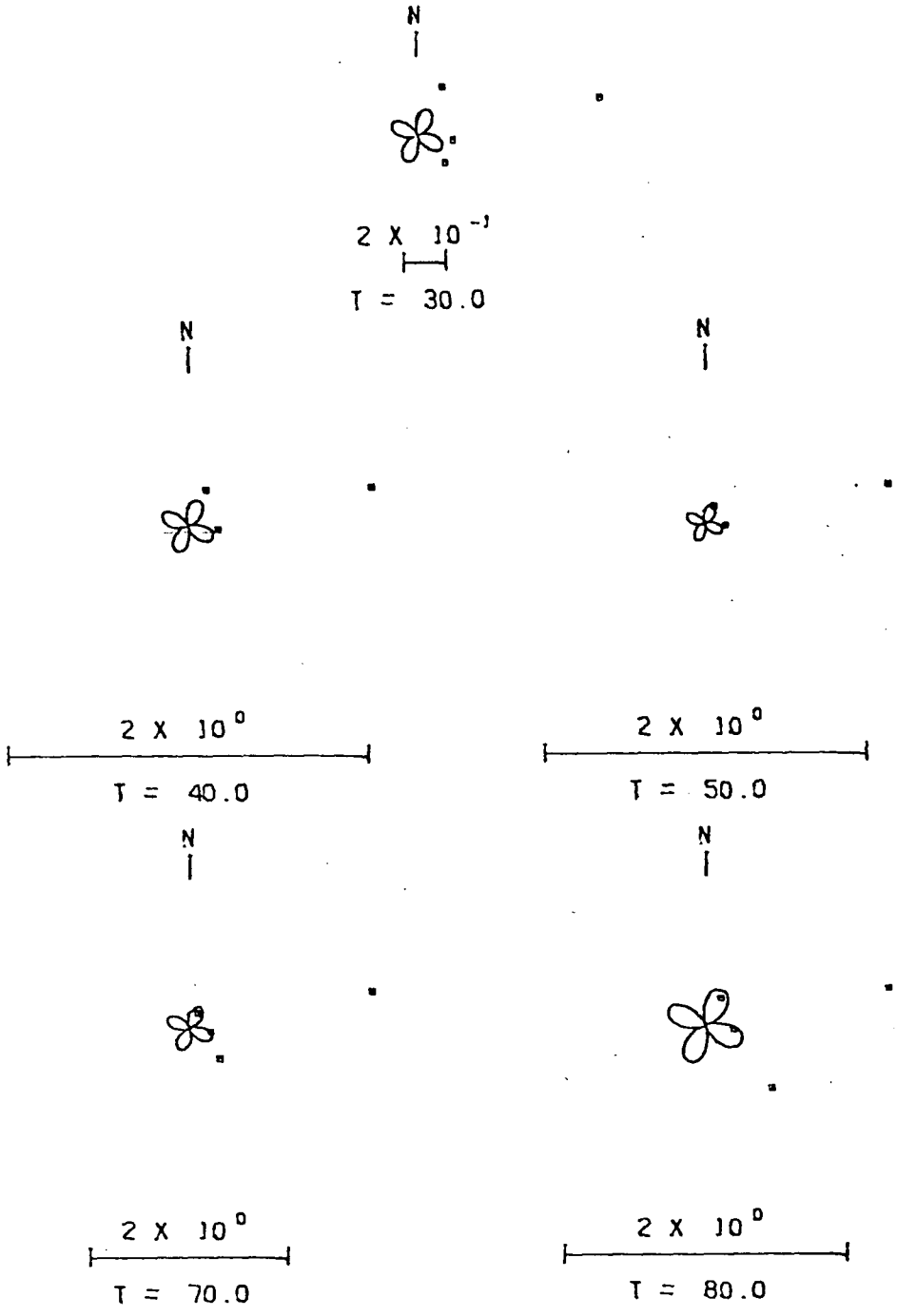

Figure 39 - THEORETICAL LOVE WAVE RADIATION PATTERN FOR THE OCTOBER 31 EARTHQUAKE

The radiation patterns are scaled to fit in a square 2-3/4 inches on a side. Beneath each radiation pattern the period is written along with a scale relating the plot size to units of dyne-cm. The radiation pattern shown is of the best fit mechanism solution. The dots indicate the observed data. Each dot represents a station, with the azimuth of the dot corresponding to the station azimuth, and the distance of the dot from the center of the radiation pattern.

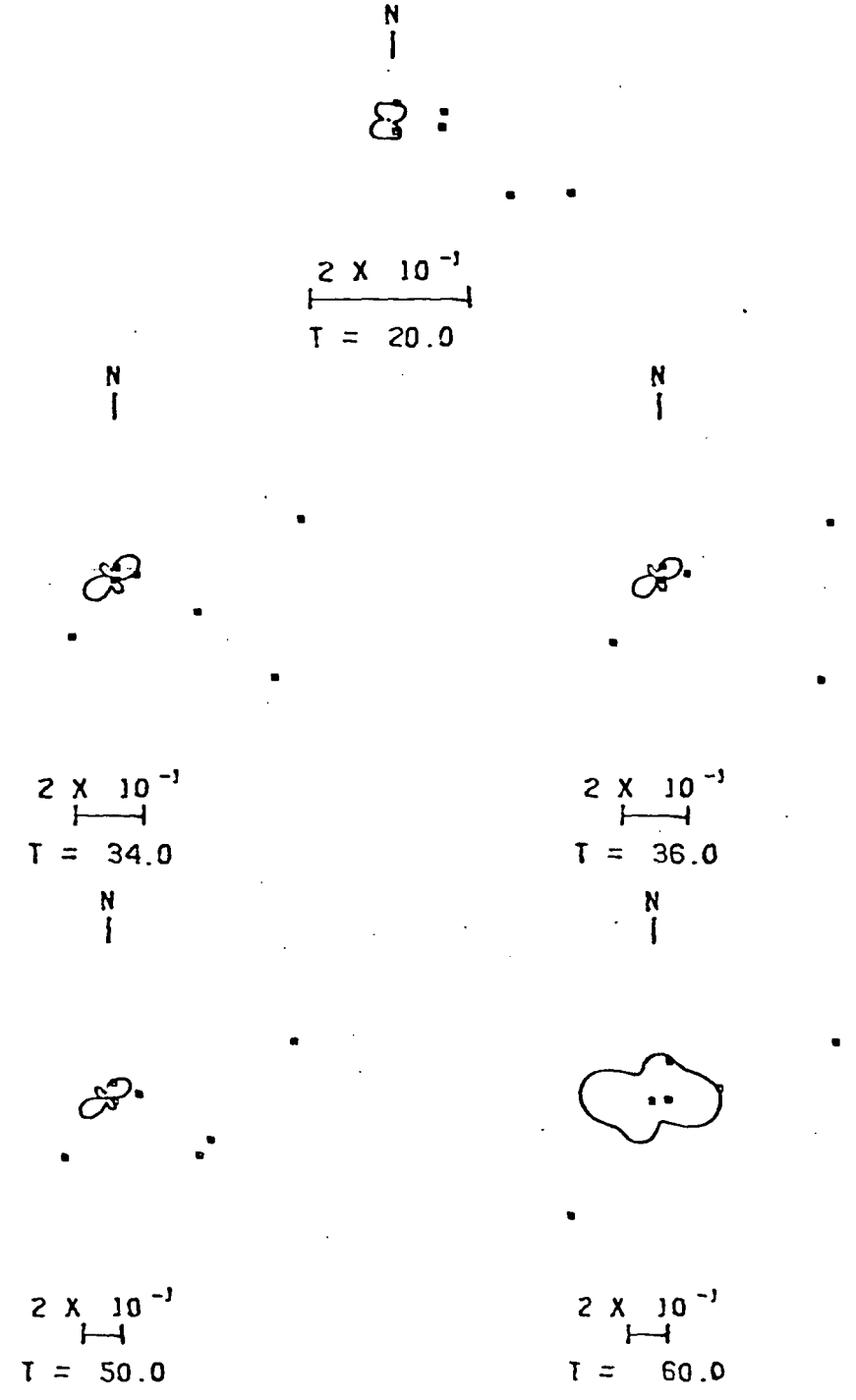

Figure 40 - THEORETICAL RAYLEIGH WAVE RADIATION PATTERN FOR THE OCTOBER 31 EARTHQUAKE

The radiation patterns are scaled to fit in a square 2-3/4 inches on a side. Beneath each radiation pattern the period is written along with a scale relating the plot size to units of dyne-cm. The radiation pattern shown is of the best fit mechanism solution. The dots indicate the observed data. Each dot represents a station, with the azimuth of the dot corresponding to the station azimuth, and the distance of the dot from the center of the radiation pattern.

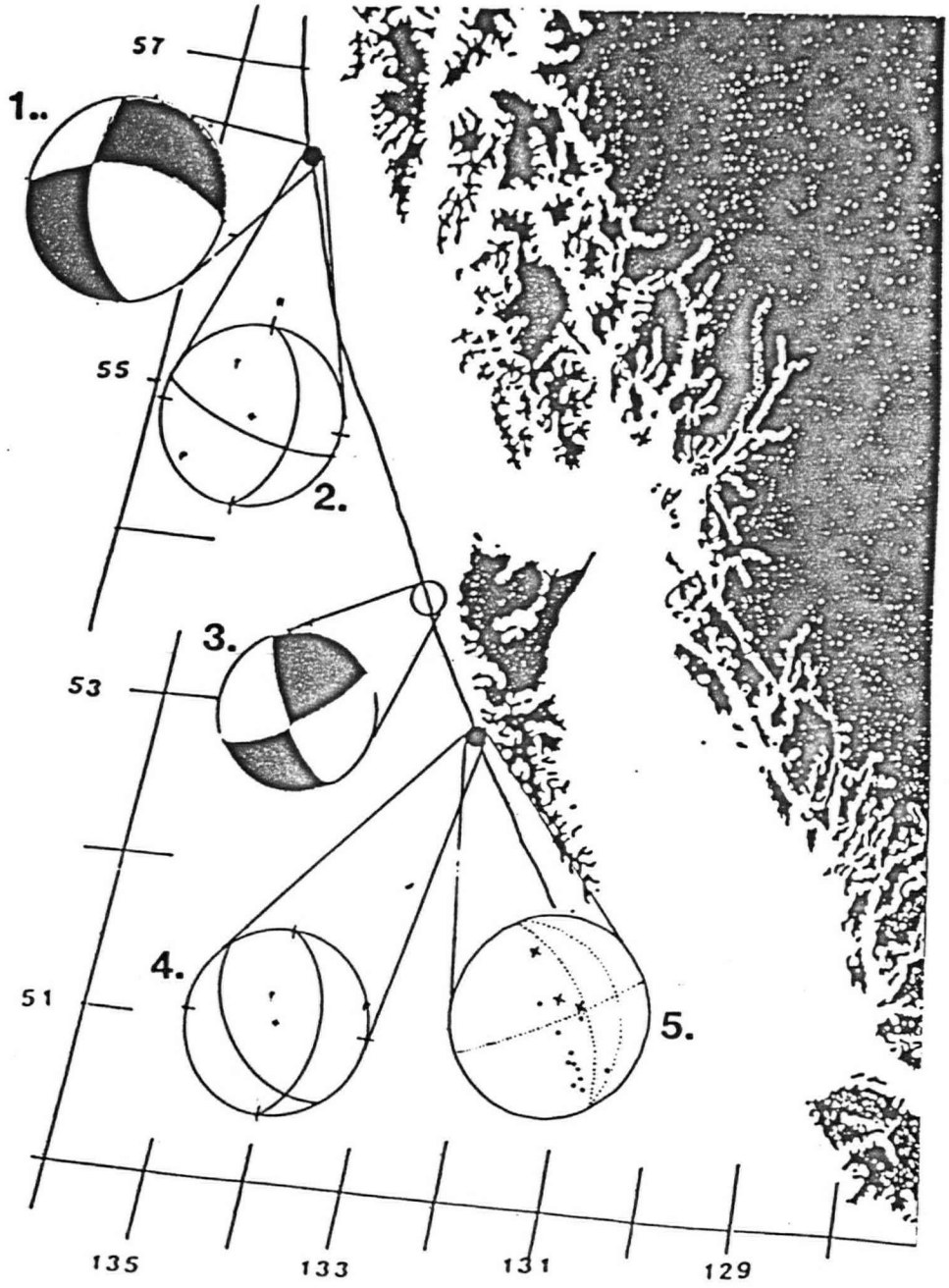

Figure 41 - FOCAL MECHANISMS OF THE AUGUST 23 AND OCTOBER 31 EARTHQUAKES

Dipicted in this figure are lower hemisphere focal sphere projections of: 1) The poorly defined P-nodal solution of Wickens and Hodgson (1967) for the October 31 earthquake (M=6.2), 2) The very poorly constrained best fit surface wave mechanism solution for the October 31 earthquake, 3) The well defined P-nodal solution of Rogers (1983) for the August 22 (M=8.1) earthquake. 4) The very poorly constrained best fit surface wave mechanism solution for the August 23 earthquake (M=6.4), 5) Suggested possible nodal planes from the few first motion readings available for the August 23 earthquake. Note that the position of the pressure and tension axes for best fit surface wave mechanisms can be reversed, as right-lateral or left-lateral strike-slip motion can not be distinguished from amplitude data alone (Herrmann, 1978).

The correct surface wave solution must be compatible with the first motion data unless the focal mechanism changed radically as the rupture progressed. If the first motion data is used as a constraint, the surface wave mechanisms obtained for the August 23 earthquake must be wrong.

The conclusion drawn from this study is that the method of using the azimuthal surface wave radiation pattern to obtain the focal mechanism is ineffective for this area and period in history when station coverage was sparse and the quality of instrument calibrations poor.

VI. SUMMARY AND DISCUSSION

6.1 DISCUSSION

The directivity function and differential phases were analyzed at three stations. The results imply a unilateral rupture propagating to the northwest for approximately 265 km at a rupture velocity between 3.1 km/s and 3.5 km/s. These rupture velocity results are in good agreeement with other investigators who have found that the the rupture velocity for other earthquakes is in the range of 3.1 km/s to 3.5 km/s. In general, it appears that the rupture velocity is usually slightly less than the shear wave velocity in the crust.

The rupture length of the 1949 Queen Charlotte earthquake derived from the directivity and differential phase functions does not agree with the fault length of 490 km derived from the aftershock zone. It is tempting to resolve this apparent conflict by dismissing the surface wave results as being too limited and influenced by the poor quality of the data. To some extent this may be true, as the precise values for rupture length and rupture velocity are uncertain; nevertheless, the data are good enough to indicate that they are incompatible with a surface wave fault length of 490 km. In fact, while my data were limited to short period instruments, Ben-Menahem's analysis of this earthquake was made using the Pasadena EW strain-meter (Tg=70 s), a true long period instrument. His results of 265 km for the differential phases fault length in the period range 125-277 seconds show excellent coherence and cannot be dismissed

as affected by noise.

The relationship between aftershock zone and fault rupture length can be seen more clearly by looking at the results other investigaters have obtained. Other examples of source parameter determination from directivity and differential phase functions are listed in Table IV.

	DIRECTIVITY FAULT LENGTH (KM)	DIFFERENTIAL FAULT LENGTH (KM)	AFTERSHOCK FAULT LENGTH (KM)	REFERENCE
Chile May 22, 1960 M=8.5	725		1000	Press et al. (1961)
Kamchatka Nov. 4, 1952 M=8.25	700	426	675	Ben-Menahem and Toksoz (1963a)
Mongolia Dec. 4, 1957 M=8.0	560		500	Ben-Menahem and Toksoz (1962)
San Francisco June 6, 1906 M=8.0	240		400	Ben-Menahem (1978)
Alaska July 10, 1958 M=8.0	350	279	380	Ben-Menahem and Toksoz (1963b)
Kurile Islands Oct. 13, 1963 M=8.0		250	300	Furumoto (1979)
Sanriku March 2, 1933 M=8.0	270		270	Ben-Menahem (1967)

Table IV - RUPTURE LENGTH FROM DIRECTIVITY AND DIFFERENTIAL PHASES

Examples from the literature of fault lengths derived from the differential phases and or the directivity function. The examples are listed in decreasing order of fault length.

Clearly there can be a discrepancy of 40% between the surface wave rupture length and the rupture length defined from

aftershocks. Ben-Menahem (1978), in seeking to explain the difference between the directivity fault length and the known surface rupture of the 1906 San Francisco earthquake, suggested that there is an effective radiation fault length which may not correspond to the full fault rupture. He points out that the observed displacement along the San Andreas fault for the 1906 earthquake ranged from slightly more than 6 meters for the area around Pt. Reyes to under 0.5 meters for the area south of the Santa Cruz mountains. He suggests that once the displacement along the fault becomes less than a given average value, 0.6 meters in the 1906 case, the affect of the remaining rupture on the radiation amplitude and phase is small and does not influence the directivity and differential phase function (see Figure 42).

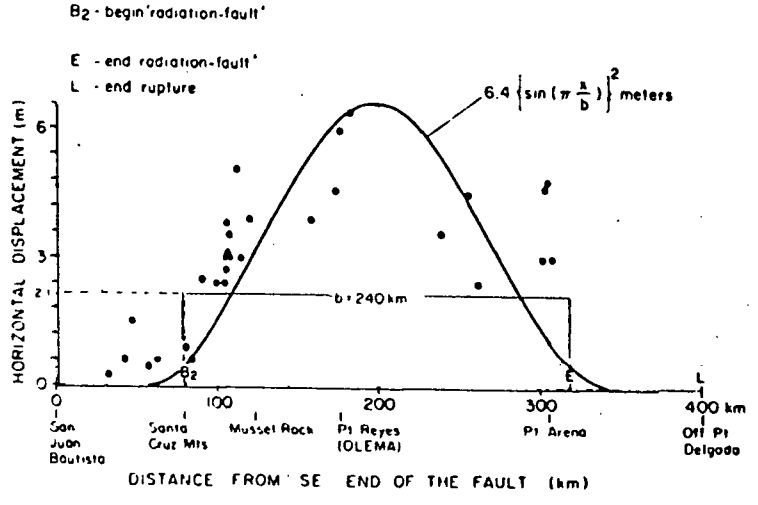

Figure 42 - DISPLACEMENT ALONG THE SAN ANDREAS FAULT FOR THE 1906 EARTHQUAKE

This figure shows the relationship of the displacement along the San Andreas fault to the directivity fault length. The dots represent the measured offset displacement along the fault (from Ben-Menaham, 1978).

If a similar explanation is used to explain the discrepancy between the surface wave fault length and the aftershock zone fault length for the 1949 Queen Charlotte earthquake, then it implies that displacement along the fault was uneven. The northwestward propagation of the effective radiation fault rupture suggests that the largest displacement along the fault occurred for 265 km to the north of the epicenter with the rupture displacement continuing, but with smaller offset, for another 35 km further north and 190 km to the south of the epicenter.

Information can be obtained by further analysis of the M=8.1 August 22 earthquake. In particular, there is enough information given by Ben-Menahem (1967) to determine the initial phase, and, hence, the time function of the 1949 Queen Charlotte earthquake. The time function would be of particular interest as it can be used to derive the rise time of the rupture, which can in turn yield information about the initial stress levels (Kasahara, 1981). Rise-time analysis also plays an important role in earthquake engineering in which prediction of seismic vibration, acceleration and velocity are desired. The use of surface waves to analyse the rupture parameters proved difficult due to the lack of long period instruments operating in 1949. Thus, further study of the source parameters through the use of body waves would be more suited to the instrument responses. Body wave directivity and azimuthal radiation patterns could be obtained to supplement the first motion and surface wave results (e.g., Langston, 1978).

As well as studying the main 8.1 shock an attempt was made to derive the mechanism solutions for the two largest aftershocks using their azimuthal surface wave radiation patterns. It was concluded that the use of this technique to obtain focal mechanism solutions is ineffective for this area and time in history when station coverage was sparse and the quality of instrument calibrations poor.

In view of the limitations in obtaining the overall surface wave radiation pattern, a more productive approach to determining the surface wave focal mechanism might be to select one station for which the instrument parameters and calibration are well known and then try to model the entire surface wave train recorded at that station (e.g., Kanamori, 1970). The dispersion curves for the October 31 earthquake suggest that the surface waves have not been well recorded as no clear mode arrivals can be seen, and, thus, this method might not be successful when applied to that earthquake using the data I've collected (see Figures 32-35) . On the other hand, the dispersion curves for the August 23 earthquake do display clear mode arrivals and suggest that synthetic seismogram modeling of the surface wave forms recorded at DBN might be successful (see Figures 29-31).

6.2 CONCLUSION

Using horizontal seismograms recorded at Sitka, Alaska, thirty-eight new aftershock locations were determined for the 1949 Queen Charlotte earthquake. The aftershock zone was found to extend from 300 km to the north of the epicenter to 190 km to the south of the epicenter, yielding a total aftershock zone of 490 km. This aftershock zone implies that a previously suggested seismic gap to the north of the 1949 epicenter (Kelleher and Savino, 1975) does not exist. The aftershock distribution also suggests a time variation in the rupture sequence, with the aftershocks concentrating first to the north and later to the south of the main shock's epicenter.

The directivity function and differential phases were analyzed at three stations. The results imply a unilateral rupture propagating to the northwest for approximately 265 km at a rupture velocity between 3.1 km/s and 3.5 km/s. These results agree with the results of Ben-Menahem (1967,1978).

The difference between the aftershock zone,and the rupture length derived from the directivity function and differential phases, suggests that there may be a difference between the fracture length and the effective radiation length. This difference between the fracture length and radiation length was first noted by Ben-Menahem (1978) for the 1906 San Francisco earthquake, which, like the Queen Charlotte earthquake, occurred along a shallow vertical strike-slip fault. This difference between the radiation fault length and the fracture fault length suggests that the displacement along the fault was uneven, with

the largest displacement occurring in the area that corresponds to the radiation fault length.

The seismic moment, average fault displacement, seismic energy, apparent stress drop, stress drop, average stress, strain energy, and frictional stress were all estimated for the M=8.1 event and are summarized in Table V.

As well as studying the main shock an attempt was made to derive the mechanism solutions for the two largest aftershocks using their azimuthal surface wave radiation patterns. It was concluded that the use of this technique to obtain focal mechanism solutions is ineffective for this area and time in history when station coverage was sparse and the quality of instrument calibrations poor.

Fault Length	495	km
Fault Depth	20	km
Fault Area	9900	km^2
Rupture Velocity	3.1	km/sec
Average Fault Displacement	4.96	m
Seismic Moment	1.15×10^{28}	dyne cm
Strain Energy	9.5×10^{23}	ergs
Seismic Energy	8.9×10^{23}	ergs
Apparent Stress Drop	25	bars
Stress Drop	34	bars
Average Stress	26.9	bars
Frictional Stress	1.9	bars

Table V - ESTIMATE OF SEISMIC SOURCE PARAMETERS OF THE 1949 QUEEN CHARLOTTE EARTHQUAKE

BIBLIOGRAPHY

1. Acharya, H. K. 1979. Regional variations in the rupture-length magnitude relationships and their dynamical significance. Bulletin of the Seismological Society of America, 69, pp. 2063-2084.

2. Aki, K. 1966. Generation and propagation of G waves from the Niigata Earthquake of June 16, 1964. Bulletin of the Earthquake Research Institute, 44, pp. 23-72.

3. Aki, K., and Richards, P.G. 1980. Quantitative Seismology, Vol. 1. W. H. Freeman Co., San Francisco, CA., 557 pp.

4. Ben-Menahem, A. 1961. Radiation of seismic surface-waves from finite moving sources. Bulletin of the Seismological Society of America, 55, pp. 401-435.

5. Ben-Menahem, A. 1967. Source studies from isolated seismic signals. In: VESIAC conference. on the current status and future prognosis for understanding the source mechanism of shallow seismic events. University of Michigan, Geophys. Lab., pp. 85-108.

6. Ben-Menahem, A. 1978. Source mechanism of the 1906 San Francisco earthquake. Physics of the Earth and Planetary Interiors, 17, pp. 163-181.

7. Ben-Menahem, A., and Toksoz, N. M. 1962. Source-mechanism from spectra of long-period seismic waves, 1: The Mongolian earthquake of December 4, 1957. Journal of Geophysical Research, 67, pp. 1943-1955.

8. Ben-Menahem, A., and Toksoz, M. N. 1963a. Source-mechanism from spectra of long-period seismic waves, 2: The Kamchatka earthquake of November 4, 1952. Journal of Geophysical Research, 68, pp. 5207-5222.

9. Ben-Menahem, A., and Toksoz, M. N. 1963b. Source-mechanism from spectra of long-period surface waves, 3: The Alaska earthquake of July 10, 1958. Bulletin of the Seismological Society of America, 53, pp. 905-919.

10. Chandra, U. 1974. Seismicity, earthquake mechanisms and tectonics along the western coast of North America, from 42° to 61°N. Bulletin of the Seismological Society of America, 64, pp. 1529-1549.

11. Chase, C. G. 1978. Plate kinematics: The Americas, East Africa and the rest of the world. Earth and Planetary Science Letters, 37, pp. 355-368.

12. Forsyth, D. A., Berry, M. J., and Ellis, R. M. 1974. A refraction survey across the Canadian Cordillera at 54°N. Canadian Journal of Earth Sciences, 11, pp. 533-548.

13. Furumoto, M. 1979. Initial phase analysis of R Waves from great earthquakes. Journal of Geophysical Research, 84, pp. 6867-6874.

14. Geller, J., and Kanamori, H. 1977. Magnitudes of great shallow earthquakes from 1944 to 1952. Bulletin of the Seismological Society of America, 67, pp. 587-598.

15. Harkrider, D. G. 1970. Surface waves in multilayered elastic media. 2. Higher mode spectra and spectral ratios from point sources in plane layered earth models. Bulletin of the Seismological Society of America, 60, pp. 1937-1988.

16. Haskell, N. A. 1953. The dispersion of surface waves on multilayered media. Bulletin of the Seismological Society of America, 43, pp. 17-34.

17. Herrmann, R. B., ed., 1978. Computer Programs In Earthquake Seismology, Department of Earth and Atmospheric Sciences, Saint Louis University.

18. Hodgson, J. H., and Milne, W. G. 1951. Direction of faulting in certain earthquakes of the north Pacific. Bulletin of the Seismological Society of America, 41, pp. 221-242.

19. Hodgson, J. H., and Storey, R. S. 1954. Direction of faulting in some of the larger earthquakes of 1949. Bulletin of the Seismological Society of America, 44, pp. 57-83.

20. Horn, J. R., Clowes, R. M., Ellis, R. M., and Bird, D. N. 1984. The seismic structure across an active oceanic/continental transform fault zone. Journal of Geophysical Research, 89, pp. 3107-3120.

21. Horner, R. B. 1983. Seismicity in the St. Elias Region of northwestern Canada and southeastern Alaska. Bulletin of the Seismological Society of America, 73, pp. 1117-1138.

22. Hyndman, R. D., and Ellis, R. M. 1981, Queen Charlotte Fault Zone: microearthquakes from a temporary array of land stations and ocean bottom seismographs. Canadian Journal of Earth Sciences, 18, pp. 776-788.

23. Hyndman, R. D., Lewis, T. J., Wright, J. A., Burgess, M., Chapman, D. S., and Yamano, M. 1982. Queen

Charlotte fault zone: Heat flow measurements. Canadian Journal of Earth Sciences, 19, pp. 1657-1669.

24. Hyndman, R. D., and Weichert, D. H. 1983. Seismicity and rates of relative motion of plate boundaries of western North America. Geophysical Journal of the Royal Astronomical Society, 72, pp. 53-69.

25. Iida, K. 1965. Earthquake magnitude, earthquake fault source dimensions. Journal of Earth Science of Nagoya University, 13, pp. 115-132.

26. Jeffreys, H., and Bullen, K. E. 1967. Seismological tables. British Association for the Advancement of Science, Gray Milne Trust, Office of the British Association, London, 50 pp.

27. Kanamori, H. 1970. Synthesis of long-period surface waves and its application to earthquake source studies-Kurile Islands earthquakes of October 13, 1963. Journal of Geophysical Research, 75, pp. 5011-5027.

28. Kanamori, H., and Anderson, D. L. 1975. Theoretical basis of some empirical relations in seismology. Bulletin of the Seismological Society of America, 65, pp. 1073-1095.

29. Kasahara, K. 1981. Earthquake Mechanics, Cambridge University Press, Cambridge, UK., 284 pp.

30. Kelleher, J. A. 1972. Rupture zones of large South American earthquakes and some predictions. Journal of Geophysical Research, 79, pp. 2087-2103.

31. Kelleher, J., and Savino, J. 1975. Distribution of seismicity before large strike-slip and thrust type earthquakes. Journal of Geophysical Research, 80, pp.260-271.

32. Kovach, R. L. 1965. Seismic surface waves: some observations and recent developments. Physics and Chemistry of the Earth, 6, pp. 251-314.

33. Langston, C. A. 1978. The February 9, 1971 San Fernando Earthquake: A study of source finiteness in teleseismic body waves. Bulletin of the Seismological Society of America, 68, pp. 1-29.

34. Lathram, E. H. 1964. Apparent right lateral separation of the Chatham Strait fault, southeast Alaska. Bulletin of the Seismological Society of America, 75, pp. 249-252.

35. Minster, J. B., and Jordan, T. H. 1978. Present day plate motions. Journal of Geophysical Research, 83, pp.

5331-5354.

36. Page, R. 1969. Late Cenozoic movement on the Fairweather fault in southeastern Alaska. Bulletin of the Seismological Society of America, 80, pp. 1873-1877.

37. Perez, O. J., and Jacob, K. H. 1980. Tectonic model and seismic potential of the eastern Gulf of Alaska and Yakataga seismic gap. Journal of Geophysical Research, 85, pp. 7132-7150.

38. Press, F., Ben-Menahem, A., and Toksoz, N. M. 1961. Experimental determination of earthquake fault length and rupture velocity. Journal of Geophysical Research, 66, pp. 3471-3485.

39. Richter, C. F. 1958. Elementary Seismology. W. H. Freeman Co., San Francisco, CA., p. 69.

40. Riddihough, R. P. 1977. A model for recent plate interactions off Canada's west coast. Canadian Journal of Earth Sciences, 14, pp. 384-396.

41. Riddihough, R. P., Currie, R. G., and Hyndman, R. D. 1980. The Delwood Knolls and their role in triple junction tectonics off northern Vancouver Island. Canadian Journal of Earth Sciences, 17, pp. 577-593.

42. Rogers, G. 1976. A microearthquake study in northwest British Columbia and southeast Alaska. Bulletin of the Seismological Society of America, 66, pp. 1643-1655.

43. Rogers, G. 1983. Seismotectonics of British Columbia. Ph.D. thesis, University of British Columbia, 247 pp.

44. Stauder, W. 1959. A mechanism study: The earthquake of October 24, 1927. Geofisica Pura e Applicata, 44, p. 135.

45. Stauder, W. 1960. The Alaska earthquake of July 10, 1958: Seismic studies. Bulletin of the Seismological Society of America, 50, pp. 293-322.

46. Tobin, P. G., and Sykes, L. R. 1968. Seismicity and tectonics of the north-east Pacific Ocean. Journal of Geophysical Research, 73, pp. 3821-3846.

47. Tocher, D. 1958. Earthquake energy and ground breakage. Bulletin of the Seismological Society of America, 48, pp. 147-152.

48. Tsai, Y., and Aki, K. 1970. Precise focal depth determination from amplitude spectra of surface waves. Journal of Geophysical Research, 75, pp. 5729-5741.

49. Von Heune, R., Shor, G., and Wageman, J. 1979. Continental margins of the eastern Gulf of Alaska and boundaries of tectonic plates. In: Geological and Geophysical Investigations of Continental Margins, edited by J. S. Watkins, L. Montadent, and P. W.

50. Wetmiller, R. J., and Horner, R. B. 1978. Canadian earthquakes 1976. Seismological Series of the Earth Physics Branch, 79, p. 75.

51. Wickens, A. J., and Hodgson, J. H. 1967. Computer re-evaluation of earthquake mechanism solutions 1922-1962. Publications of the Dominion Observatory, Ottawa, 33, pp. 1-560.

52. Wyss, M. 1978. Estimating maximum expectable magnitude of earthquake from fault length (abstract). EOS, Transactions of the American Geophysical Union, 59, p. 1125.

53. Wyss, M. 1979. Estimating maximum expectable magnitude of earthquakes from fault dimensions. Geology, 7, pp 336-340.

APPENDIX A - LIST OF SEISMOGRAPH STATIONS

	Instruments	Type of Records Received	Source
Berkeley (BRK)	Benioff NS,EW,Z	photocopy	Berkeley-Network (Berk-Net)
Aug.22,23 and Oct.31-messy traces, off scale.			
Bermuda (BEC)	Milne-Shaw NE,NW	microfilm	World Data Center A (WDC-A)
Aug.22-off scale, Aug.23-o.k., Oct.31-amplitues too small.			
Boulder City (BCN)	Benioff NS,EW,Z	....	WDC-A
No records received			
Bozeman (BOZ)	McComb-Romberg N,E	microfilm	WDC-A
Aug.22-off scale, Aug.23 and Oct.31-are good.			
Chicago (CHK)	McComb-Romberg N,E	....	WDC-A
no records received			
College (COL)	Benioff N,E	microfilm	WDC-A
Aug.22,23 and Oct.31-all off scale.			
Columbia (CSC)	McComb-Romberg N,E	....	WDC-A
no records received			
De Bilt (DBN)	Galitzin Z,N,E	photocopy	De Bilt
Aug.22,23 and Oct.31-all excellent.			
Fresno (FRE)	Sprengnether Z,N,E	photocopy	Berk-Net
Aug.23 only-excellent.			
Halifax (HAL)	Bosch-Omori N,E	original	Canadian-Network (Can-Net)
Aug.22-L2,R2 amplitudes too small,Aug.23-good,Oct.31-poor.			
Honolulu (HON)	Milne-Shaw N,E	microfilm	WDC-A
Aug.22,23 and Oct.31-good.			
Melbourne (MEL)	Milne-Shaw E	photocopy	Melbourne
Aug.22-L2,R2 amplitudes to small, Aug.23-missing, Oct.31-o.k.			
Mt. Hamilton (MHC)	Wood-Anderson N,E, Benioff Z	microfilm	Berk-Net
instrument too short period to be useful.			
Ottawa (OTT)	Milne-Shaw N,E, Benioff z	original	Can-Net
Aug.22-L2,R2 amplitudes too small, Aug.23 and Oct.31-good.			
Pasadena (PAS)	Benioff Z,N,E	microfilm	Pasadena
Aug.22,23 and Oct.31-all good.			
Perth (PER)	Milne-Shaw N	photocopy	Perth
Aug.22 only-unreadable			
Philadelphia (PHI)	Wenner N,E	....	WDC-A

No records received

Pierce Ferry (PFA) Benioff Z,N,E .... WDC-A
No records received

Rapid City (RCD) Wood-Anderson E microfilm WDC-A
instrument too short period to be useful.

Riverview (RIV) Galitzin Z,N,E photocopy Riverview
Aug.22-off scale, Aug.23 and Oct.31-confused timing,records suspect

Salt Lake City (SLC) Bosh-Omori-McComb-Romberg N,E microfilm
Aug.22,23-off scale, Oct.31-good. WDC-A

Saskatoon (SAS) Milne-Shaw NE,NW original Can-Net
Oct.31 only-o.k.

San Juan (SJP) Wenner N,E microfilm WDC-A
Aug.22-off scale, Aug.23 and Oct.31-good.

Seven Falls (SFA) Milne-Shaw E original Can-Net
Aug.22-L2,R2 amplitudes too small, Aug.23 and Oct.31-o.k.

Shasta (SHS) Benioff Z,N,E .... WDC-A
No records received

Shawingan Falls (SHF) Wood-Anderson N original Can-Net
Aug.22-L2,R2 amplitudes too small, Aug.23 and Oct.31-o.k.

Sitka (SIT) Wenner N,E original Sitka
Aug.22,23 and Oct.31-all off scale.

Stuttgart (STU) Galitzin-Wilip Z,N,E .... Stuttgart
Received a reply, but refused to send records.

Tokyo (TOK) Wiechert, Omori, Galitzin .... Tokyo
No response.

Tucson (TUO) Wood-Anderson NS,EW, Benioff LPZ microfilm
Aug.22,23-o.k., Oct.31-rips in records make this useless.

Uppsala (UPP) Wiechert N,E photocopy Uppsala
Aug.22-L2,R2 amplitudes too small,Aug.23 and Oct.31-amp.too small

Utsunomiya (UTS) Wiechert Z,N,E .... Utsunomiya
No response

Victoria (VIC) Benioff Z original Can-Net
instrument too short period to be useful.

APPENDIX B - WORLD AVERAGED PHASE VELOCITIES AND Q VALUES

LOVE

PHASE VELOCITIES

PERIOD (s)	C (km/s)	
48.	4.49	(1)
86.24	4.616	(1)
90.55	4.626	(1)
100.61	4.651	(1)
113.16	4.693	(1)
129.26	4.725	(1)
143.54	4.764	(1)
161.35	4.815	(1)
180.52	4.871	(1)
196.05	4.917	(1)
209.57	4.959	(1)
230.79	5.025	(1)
249.79	5.085	(1)
256.84	5.107	(1)
264.31	5.131	(1)
299.19	5.244	(1)

Q VALUES

PERIOD (s)	Q	U (km/s)	$\gamma \times 10^{-5}$ km^{-1}	
44.68	197	5.519	6.46	(2)
53.94	187	5.265	5.91	(2)
72.36	190	5.413	4.22	(2)
102.59	139	4.498	4.89	(2)
125.92	119	4.385	4.78	(1)
139.46	116	4.385	4.42	(1)
161.78	121	4.384	3.66	(1)
181.04	119	4.382	3.32	(1)
200.95	111	4.382	3.21	(1)
210.21	111	4.382	3.07	(1)
225.70	113	4.382	2.81	(1)
250.66	112	4.386	2.55	(1)
281.55	115	4.397	2.20	(1)
300.37	110	4.407	2.15	(1)

RAYLEIGH

PHASE VELOCITIES

PERIOD (s)	C (km/s)	
10.0	3.39	(3)
20.0	3.62	(3)
25.0	3.53	(3)
30.0	3.85	(3)
35.0	3.90	(4)
40.0	3.93	(4)
46.0	4.0	(4)
92.0	4.083	(4)
125.0	4.196	(1)
150.0	4.296	(1)
175.0	4.432	(1)
200.0	4.575	(1)
225.0	4.739	(1)
250.0	4.918	(1)
275.0	5.106	(1)
300.0	5.292	(1)

Q VALUES

PERIOD (s)	Q	U (km/s)	$\gamma \times 10^{-5}$ km^{-1}	
10.0			33.0	(5)
12.0			30.0	(5)
14.0			26.0	(5)
16.0			23.0	(5)
18.0			20.0	(5)
20.0			16.0	(5)
30.0			13.0	(5)
40.0			10.0	(5)
50.0			10.0	(5)
61.08	134	3.837	10.0	(2)
73.92	112	3.812	9.13	(2)
97.73	118	3.758	7.24	(2)
125.04	127	3.707	5.33	(6)
160.11	131	3.649	4.10	(6)
181.16	136	3.615	3.52	(6)
200.90	154	3.588	2.83	(6)
212.35	159	3.577	2.60	(6)
225.17	167	3.569	2.34	(6)
250.29	180	3.578	1.94	(6)
282.21	203	3.652	1.50	(6)
306.20	219	3.758	1.24	(6)

The number in the parenthesis indicates the source that the values were taken from.

(1) Kanamori, H. 1970. Velocity and Q values of mantle waves. Physics of the Earth and Planetary Interiors, 2, pp. 259-275.

(2) Dzienwonski, A. M., and Anderson, D .L. 1981. Preliminary reference Earth model. Physics of the Earth and Planetary Interiors, 25, pp. 297-356.

(3) Aki, K., and Richards, P. G. 1980. Quantitative Seismology, Vol. 1. W. H. Freman Co., p.284.

(4) Kovach, R. L. 1965, Seismic surface waves: Some observations and recent developments, Physics and Chemistry of the Earth, 6, pp. 251-314.

(5) Herrmann, R. B., ed., 1978. Input to the computer program QU In: Computer programs in earthquake seismology, Vol. 2, Dept. of Earth and Atmospheric Sciences, Saint Louis University, pp. (XI-15)-(XI-28)

(6) Chael, E. P., and Anderson, D. L. 1982. Global Q estimates from antipodal Rayleigh waves, Journal of Geophysical Research, 87, pp. 2840-2850.

APPENDIX C - EARTH MODEL USED FOR THE AUGUST 23 AND OCTOBER 31 MECHANISM SOLUTIONS

The following model was used as the earth model in determining the theoretical surface wave radiation pattern.

Continental U.S.A.

Crustal and Upper Mantle Structure (H=layer thickness).

H km	α km/s	β km/s	ρ g/cm	$\mu, 10^{11}$ dyne/cm^2	$\lambda, 10^{11}$ dyne/cm^2
28.0	6.15	3.55	2.74	3.453	3.457
12.0	6.70	3.80	3.00	4.332	4.803
13.0	7.96	4.60	3.37	7.131	7.091
25.0	7.85	4.50	3.39	6.864	7.161
50.0	7.85	4.41	3.42	6.651	7.772
75.0	7.85	4.41	3.45	6.710	7.841
50.0	8.20	4.50	3.47	7.027	9.279
	8.40	4.60	3.50	7.406	9.884

(From Ben-Menahem, A., and Singh, S. J. 1981. Seismic Waves and Sources. Springer-Verlag Co., pp. 316.)

APPENDIX D - INSTRUMENT RESPONSE CURVES

The following plots are the instrument response curves for the eight stations used in the surface wave analysis part of this thesis.

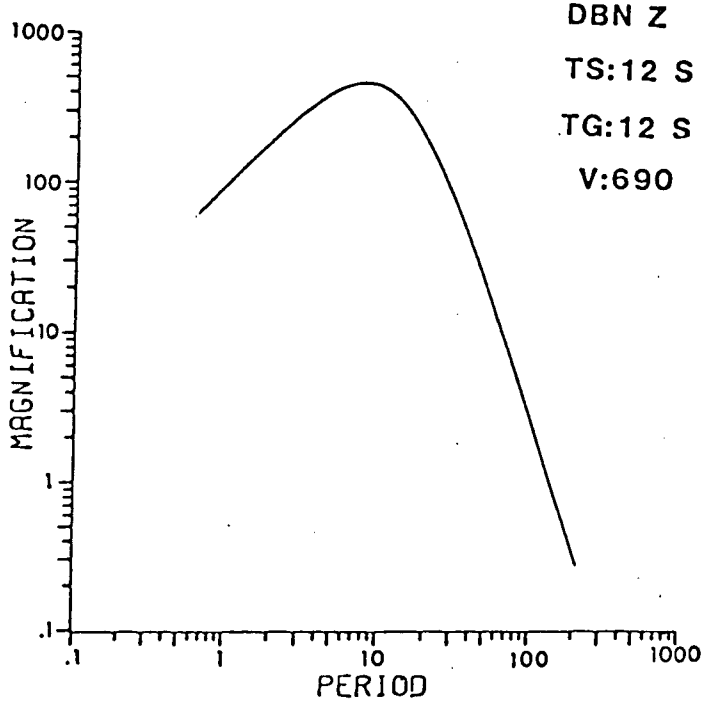

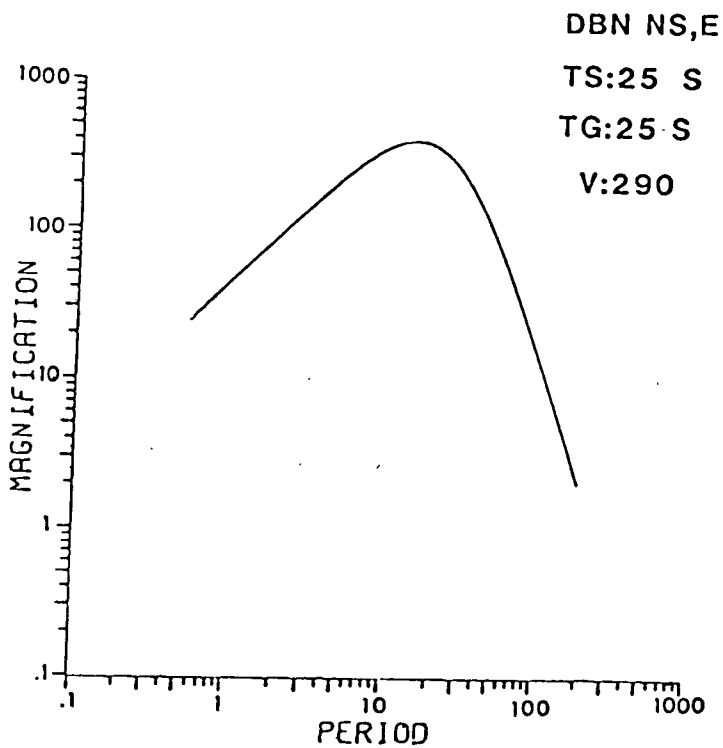

GALITIZIN

DBN

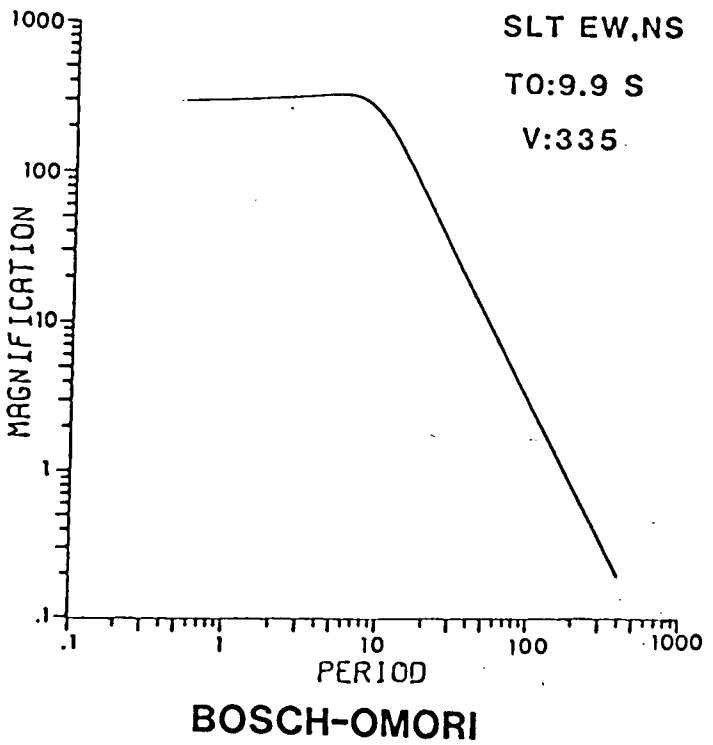

BOSCH-OMORI

SLT

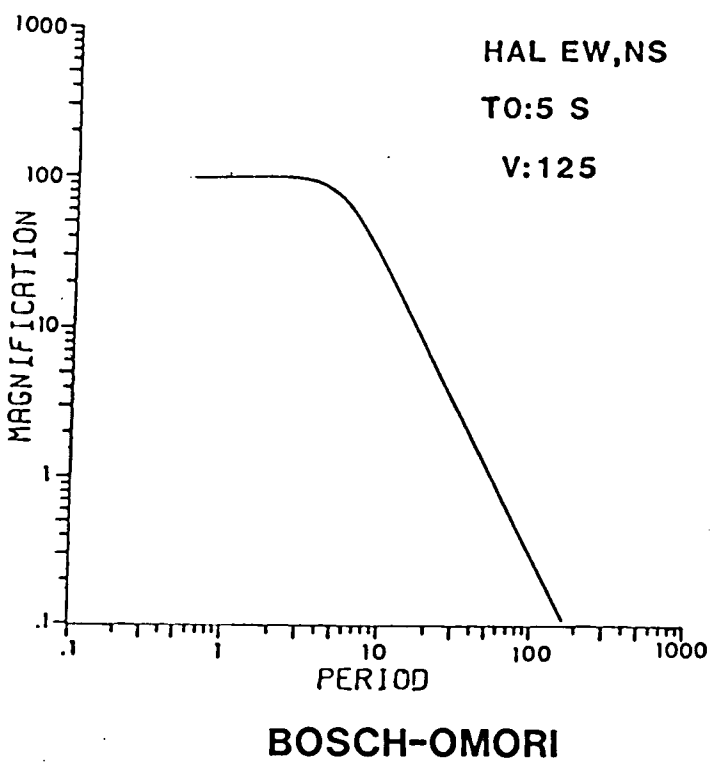

BOSCH-OMORI

HAL

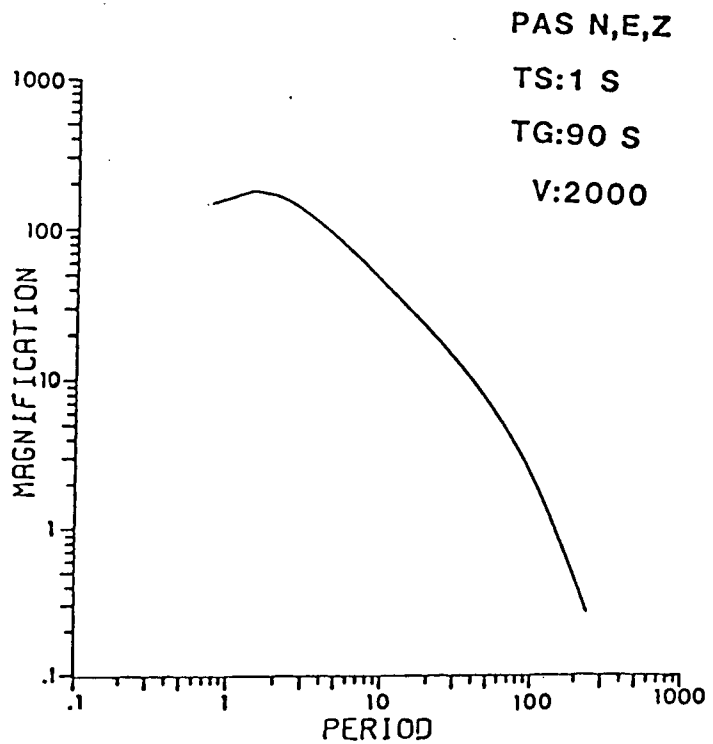

BENIOFF

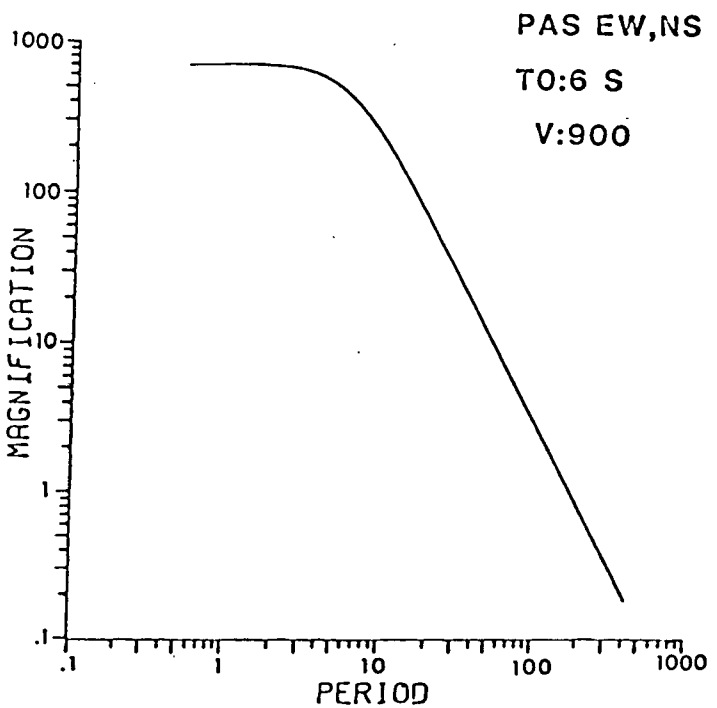

WOOD-ANDERSON

PAS

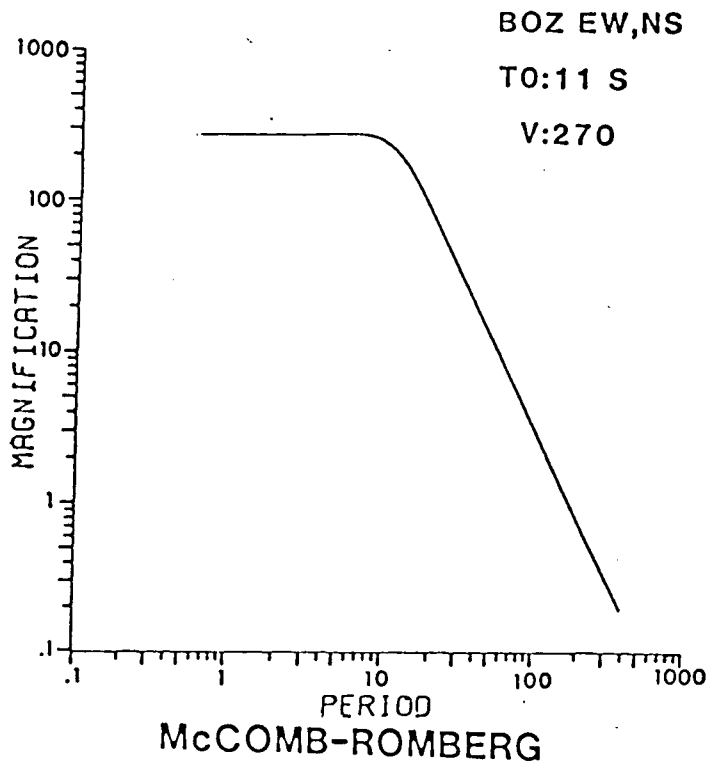
BOZ EW,NS
T0:11 S
V:270
1000
100
10
1
.1
MAGNIFICATION
.1
1
10
100
1000
PERIOD
McCOMB-ROMBERG

BOZ

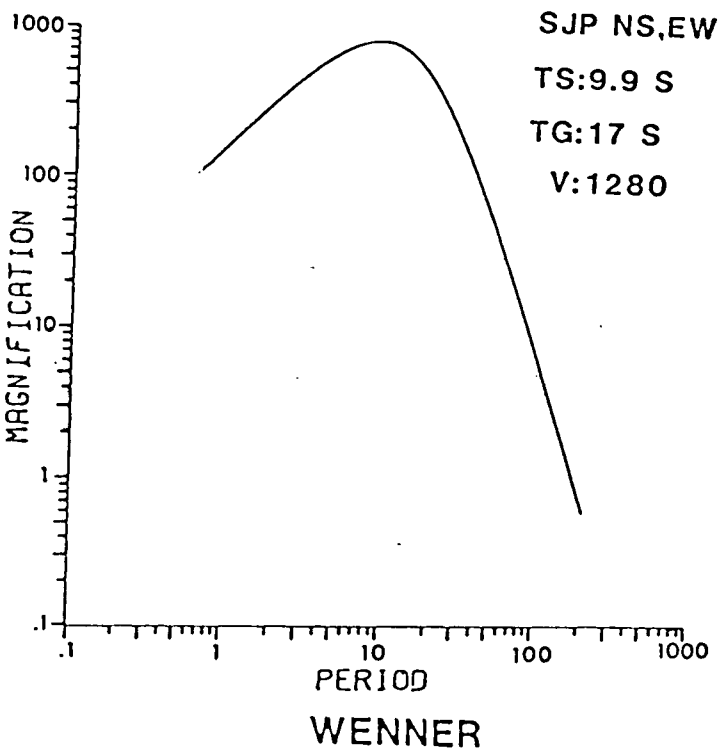
SJP NS,EW
TS:9.9 S
TG:17 S
V:1280
1000
100
10
1
.1
MAGNIFICATION
.1
1
10
100
1000
PERIOD
WENNER

SJP

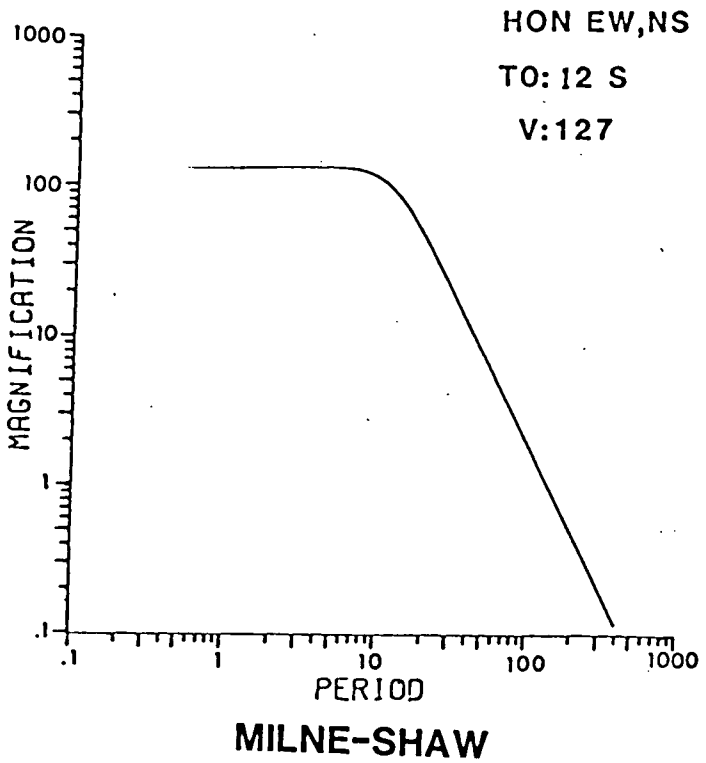

MILNE-SHAW

HON

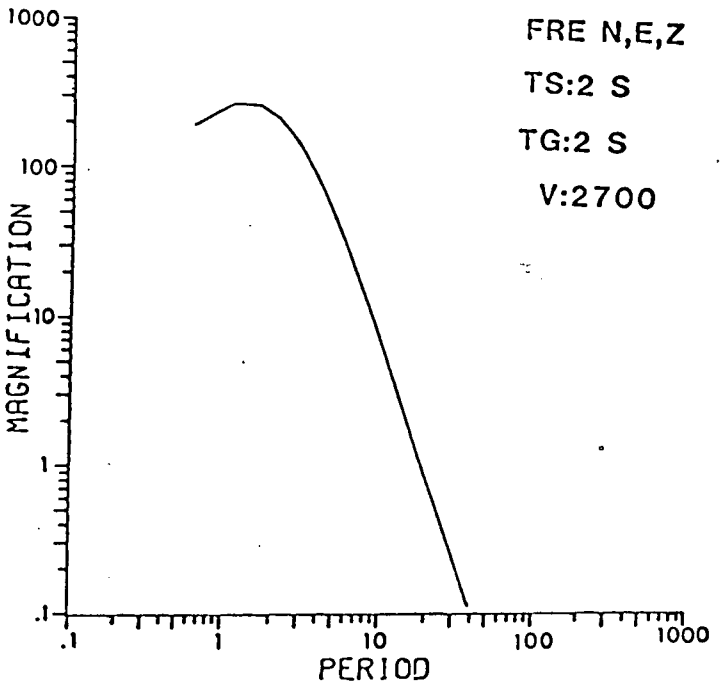

SPRENGNETHER

FRE